



**POLITECNICO  
MILANO 1863**

SCHOOL OF INDUSTRIAL AND  
INFORMATION ENGINEERING

**Master of Science in Materials Engineering  
and Nanotechnology**

# **Optimization of Parameters to Create a Porous Metal Structure**

Academic Tutor: Prof. Maurizio VEDANI  
Prof. Roberto VIGANÓ  
Prof. Riccardo CASATI

**Massimo Falconieri**

897872

Academic Year 2019/2020



## **Acknowledgements**

I would like to express my sincere gratitude to my advisor Prof. Maurizio Vedani, for providing me the opportunity to perform this thesis work under his guidance: it has been great honor to have known him and work for him.

Professor Vedani has always been the source of creative ideas and insightful advice without imposing his opinions which provided me a wonderful atmosphere to enjoy the freedom in performing my dissertation.

Also, I would like to express my gratitude to my thesis co-supervisors Prof. Roberto Viganó and Prof. Riccardo Casati for guiding me throughout my work, supporting in times of need, and help me whenever there was an issue about my research: I have to thank them for the scientific conversations and insightful suggestions about my research as well as the tremendous help for conducting different experimentations.

Without their guidance and precious advices, the writing process would have been much more difficult.

Last but not least I also would like to extend my appreciation to the Doctoral Student Filippo Beelli for helping me during the printing processes and the Dr. Ludovica Rovatti for helping me during the study of the microstructure of the sample and for their availability during the thesis work.

Finally, I would like to thank Politecnico di Milano for giving me the opportunity to study in one of the best Universities in the World and help me in developing my abilities and skills.



## **Abstract**

The following review covers the emerging research on Additive Manufacturing (AM) of metallic materials and provides a comprehensive overview of the physical processes and the underlying science of metallurgical structure and properties of the deposited parts, focusing on the creation of porous structures through the 3D printing.

This thesis work is focused on the achieving of a micro-porous metal structure by optimizing the process parameters during the 3d printing.

This method can be considered as a “controlled error” in the printings and it has to satisfy our requests of porosity: repeatability and geometric order in order to be extended from the experimental studies to the practical applications.

The main goal is to obtain the porosity by setting the optimal printing parameters, without creating it geometrically: in this way we'll have a lighter file outgoing, especially for complex geometries and big components, we reduce the errors caused by the geometrical approximations during the conversion from the CAD file to the .stl file and the method is also way faster.

After the printings, the samples are analyzed through a Scanning Electron Microscopy to check the macrostructure, the weld bead quality and size and the dimension of the pores.

After a first analysis about the difference in porosity in all the directions, we made metallographic analysis by cutting the pieces in order to study the inner porosity in the XY plane and in the XZ plane (being Z the build direction and X-Y the plane of the building platform).

The samples were then mirror polished in order to reveal the inner structure once we analyze it with the optical microscope.

After these steps we are able to draw some conclusions about the different porosities and the structure that has the optimal parameters for our application.

After having chosen the samples with the porous structure that best fit our requests, the samples have been subjected to the compression tests in the three directions in order to check the mechanical properties of the 3D lattices.

The applications for which this structure was studied are mainly moulds for expanded polymers which need to possess a permeable wall in order to allow a flow of steam to be delivered from a rear chamber into the volume of the part to be moulded, thus promoting the sintering of the polymer feedstock.

With a porosity of the order of magnitude of few hundreds of micrometers, the steam will flow through the mould wall but the polymer will not be able to fill the porosity thus achieving a good final surface finish of the formed part.

The porosity will additionally allow the passage of the cold air flow in order to cool the piece down to room temperature faster, saving time and energy.

Other applications could also be concerned with the production of filters for a wide range of applications and porous devices in the biomedical field, where osseo-integration can be promoted by a controlled porosity of prostheses.

Keywords: Additive Manufacturing, 3D Printing, Micro-porous Metal Structure, Printing Parameters, Direct Slicing, Scanning Electron Microscopy, Optical Microscopy, Compression Test

## **Sommario**

La seguente revisione copre una ricerca sull'additive manufacturing (AM) di materiali metallici e fornisce una descrizione dei processi fisici soffermandosi sullo studio delle strutture e delle proprietà dei materiali depositati con uno studio approfondito sulla creazione di strutture porose attraverso la stampa 3D.

Questa tesi è incentrata nel raggiungimento della creazione di un metallo con una micro-porosità, tramite l'ottimizzazione dei parametri del processo di stampa 3D.

Questo metodo consiste nel controllo di un "errore di stampa" a deve soddisfare le nostre richieste di porosità: ripetibilità e ordine geometrico in modo da essere esteso dagli studi sperimentali alle applicazioni pratiche.

L'obiettivo è l'ottenimento della porosità tramite l'impostazione ottimale dei parametri di stampa, senza crearla geometricamente: in questo modo noi otterremo un file più leggero in uscita, specialmente per strutture con geometrie più complesse e per grossi componenti, riduciamo gli errori causati dalle approssimazioni geometriche durante la conversione dal file CAD al file .stl ed inoltre il metodo è più veloce.

Dopo una prima analisi incentrata sulle differenze nella porosità in tutte le direzioni, procediamo con l'analisi metallografica tagliando i pezzi in modo da studiare la porosità interna nel piano XY e nel piano XZ (essendo Z la direzione di costruzione e X-Y il piano del piatto di stampa).

I provini vengono successivamente lucidati a specchio in modo da far risaltare la struttura interna una volta effettuata l'analisi con il microscopio ottico.

Dopo questi steps, siamo capaci di trarre alcune conclusioni sulle differenti porosità e possiamo decidere qual è la struttura che più soddisfa i nostri requisiti in base alle nostre applicazioni.

Dopo aver scelto le strutture con la porosità che soddisfa meglio le nostre richieste, I provini sono sottoposti ai tests di compressione nelle tre direzioni in modo da verificare le proprietà meccaniche dei "lattices" interni.

L'applicazione per il quale questa struttura è stata studiata è principalmente lo stampo per componenti polimerici espansi che hanno bisogno di avere una parete permeabile in modo da consentire un flusso di vapore che è erogato da una camera posteriore all'interno del volume del componente da stampare, promuovendo quindi la sinterizzazione del componente polimerico.

Con una porosità dell'ordine di qualche centinaio di  $\mu\text{m}$ , il vapore passerà attraverso la parete dello stampo mentre il polimero non sarà capace di riempire la porosità ottenendo quindi una buona finitura superficiale del componente creato.

La porosità consentirà inoltre anche il passaggio di aria fredda in modo da poter raffreddare il pezzo fino a temperatura ambiente più velocemente e quindi ci sarà un risparmio in termini di tempo ed energia.

Altre applicazioni possono riguardare la produzione di filtri e devices porosi con un ampio range di utilizzi inerenti il campo dell'ingegneria biomedica, dove l'interazione con le ossa può essere favorita da una porosità controllata dalle protesi.

Parole chiave: Additive Manufacturing, stampa 3D, Micro-porosità, Parametri di Stampa, Direct Slicing, Scanning Electron Microscopy, Microscopio Ottico, Test di Compressione



## Table of Contents

1	State of Art .....	15
1.1	Additive Manufacturing.....	15
1.2	Metal AM techniques .....	17
1.2.1	Directed Energy Deposition Laser .....	18
1.2.2	Directed Energy Deposition Electron Beam .....	19
1.2.3	Directed Energy Deposition Plasma Arc .....	19
1.2.4	Power Bed Fusion Laser .....	19
1.2.5	Powder Bed Fusion Electron Beam.....	22
1.2.6	The Ultrasonic AM .....	22
1.2.7	The Binder Jet AM.....	23
1.3	3D Printing of Lattices .....	23
1.4	Common methods to achieve porosity .....	26
1.4.1	Triply periodic minimal surface porous structure .....	26
1.4.2	Boolean intersection porous structure .....	29
1.4.3	Porosity for Dental implant.....	30
1.4.4	Nickel nanostructures porous technique .....	31
1.5	Conclusions.....	32
2	The strategy of development of the 3D lattices .....	33
2.1	Porosity through process parameters.....	33
3	Materials and Methods .....	36
3.1	Component design .....	36
3.2	3D Printing technology .....	36
3.3	Material.....	38
3.4	Experimental procedures.....	38
3.5	Metallographic analysis .....	40
3.5.1	Cutting .....	40

3.5.2	Mounting, grinding and optical analysis.....	41
3.6	Compression tests.....	42
4	First Printing.....	44
4.1	H400.....	47
4.2	H600, H800, H1000 and H1200.....	48
4.3	H800_o_90.....	49
4.4	Conclusion of the 1 <sup>st</sup> printing.....	51
5	Second Printing.....	52
5.1	H800_L120_ET110_PD40.....	53
5.2	H800_L120_ET140 and H800_L120_PD30.....	54
5.3	Conclusion of the 2 <sup>nd</sup> printing.....	55
6	Third Printing.....	56
6.1	H800_D100.....	58
6.2	H600_o_90_n10 and H600_o_90_n5.....	61
6.3	H600_30, H600_45 and H600_67.....	63
6.4	H1200_67.....	66
6.5	Conclusions.....	67
7	Fourth Printing.....	69
8	Metallographic analysis.....	70
8.1	H600_o_90_n5.....	72
8.2	H600_30.....	73
8.3	H600_45.....	75
9	Compression test.....	77
9.1	H600_30.....	78
9.2	H600_45.....	81
9.3	Conclusions.....	83
10	Final Conclusion.....	86

## List of Figures

Figure 1.1: Additive manufacturing general process [1] .....	16
Figure 1.2: Schematization of the most common AM processes [3] .....	17
Figure 1.3 Representation of the 3D printing process [6].....	20
Figure 1.4: a body-centred cubic, b face-centred cubic, c gyroid (skeletal/network), d double gyroid (sheet/matrix) [13] .....	24
Figure 1.5: Comparison between porous structures [16] .....	25
Figure 1.6: Gyroid Comparison [17] .....	27
Figure 1.7: Gyroid structure sections [17].....	27
Figure 1.8: Comparison between normal pore and deformed pore [17] .....	28
Figure 1.9: K3dSurf Nodal Surface Representation (a, b, c) Geomagic Studio Surface Representation (d, e, f) [20].....	29
Figure 1.10: Porous Structure of a Dental Implant [23].....	30
Figure 1.11: Section of the Dental Implant [23].....	30
Figure 1.12: TEM analysis of Nanoporous Structure [24].....	31
Figure 2.1: Comparison between CAD to Sliced and Direct Slicing file [26] .....	33
Figure 2.2: Porosity due to process parameters [26] .....	34
Figure 2.3: Comparison of .STL assembly and Direct Slicing [27] .....	34
Figure 3.1: Renishaw AM250 [29].....	36
Figure 3.2: Renishaw RBV device [29].....	37
Figure 3.3: Printing scheme .....	37
Figure 3.4: Scanning Electron Microscopy .....	39
Figure 3.5: cutting process .....	41
Figure 3.6: Compression Tests Machine .....	43
Figure 4.1: Porosity Ideal Structure [33].....	44
Figure 4.2: Scanning strategy [34] .....	44
Figure 4.3: Beam Overlap structure [35] .....	45
Figure 4.4: first printing setting .....	45
Figure 4.5: 1 <sup>st</sup> Printing .....	46
Figure 4.6: H400 .....	47
Figure 4.7: SEM analysis of H400.....	47
Figure 4.8: H600 .....	48
Figure 4.9: H800 .....	48
Figure 4.10: H1000.....	48

Figure 4.11: H1200 .....	49
Figure 4.12: H800_o_90 .....	49
Figure 4.13: SEM analysis of H800_o_90.....	50
Figure 4.14: H800_o_90 beams.....	51
Figure 5.1: Second printing setting.....	52
Figure 5.2: 2 <sup>nd</sup> Printing.....	52
Figure 5.3: H800_L120_ET110_PD40.....	53
Figure 5.4: SEM analysis of H800_L120_ET110_PD40 .....	53
Figure 5.5: H800_L120_ET140 .....	54
Figure 5.6: H800_L120_PD30 .....	54
Figure 5.7: SEM analysis of H800_L120_ET140 .....	54
Figure 5.8: SEM analysis of H800_L120_PD30 .....	55
Figure 6.1: 3 <sup>rd</sup> printing setting .....	56
Figure 6.2: 3 <sup>rd</sup> printing .....	57
Figure 6.3: Printing plate after the 3 <sup>rd</sup> print.....	57
Figure 6.4: H800_D100 printing settings .....	58
Figure 6.5: H800_D100 printing settings .....	58
Figure 6.6: H800_D100.....	59
Figure 6.7: SEM analysis of H800_D100 (up view) .....	59
Figure 6.8: SEM analysis of H800_D100 (side view).....	60
Figure 6.9: SEM analysis of H800_D100 (up-side view) .....	60
Figure 6.10: H600_o_90_n10.....	61
Figure 6.11: H600_o_90_n5 .....	61
Figure 6.12: SEM analysis of H600_o_90_n10 (side view).....	62
Figure 6.13: SEM analysis of H600_o_90_n5 (side view).....	62
Figure 6.14: H600_30.....	63
Figure 6.15: H600_45 .....	63
Figure 6.16: H600_67 .....	63
Figure 6.17: SEM analysis of H600_30 (up and side views) .....	64
Figure 6.18: SEM analysis of H600_45 (up and side views) .....	65
Figure 6.19: SEM analysis of H600_67 (up and side views) .....	65
Figure 6.20: H1200_67.....	66
Figure 6.21: SEM analysis of H1200_67 (up view).....	66
Figure 6.22: SEM analysis of H1200_67 (side view) .....	66
Figure 6.23: Comparison of the weld bead width of the samples A, B and C .....	67
Figure 7.1: 4 <sup>th</sup> printing .....	69

Figure 7.2: 4 <sup>th</sup> printing setting.....	69
Figure 8.1: Samples chosen for the metallograpy .....	70
Figure 8.2: 3rd printing process during and after.....	70
Figure 8.3: scheme of the cutting process .....	71
Figure 8.4: Cut of samples A and D.....	71
Figure 8.5: Optical Microscope Up and side views of H600_0_90_n5 .....	73
Figure 8.6: SEM Up and side views of H600_0_90_n5 .....	73
Figure 8.7: Optical Microscope Up view of H600_30 .....	74
Figure 8.8: SEM Up view of H600_30 .....	74
Figure 8.9: Optical Microscope Up view of H600_45 .....	75
Figure 8.10: SEM Side view of H600_45.....	76
Figure 9.1: Samples before and after the compression test.....	77
Figure 9.2: Compressive Tests in Z direction.....	78
Figure 9.3: Compressive Tests in X direction .....	78
Figure 9.4: Comparison in the two directions X and Z .....	79
Figure 9.5: Compressed samples in Z direction .....	79
Figure 9.6: Compressed samples in X direction.....	80
Figure 9.7: Compressive Tests in Z direction .....	81
Figure 9.8: Compressive Tests in X direction .....	81
Figure 9.9: Comparison in the two directions X and Z .....	82
Figure 9.10: Compressed samples in Z direction .....	82
Figure 9.11: Compressed samples in X direction .....	83
Figure 9.12: Comparison of the two different types of samples in Z direction .....	84
Figure 9.13: Comparison of the two different types of samples in X direction.....	84
Figure 10.1: Different applications for porous materials [36].....	87

## **Acronyms:**

**AM:** Additive Manufacturing

**CM:** Computed Tomography

**DED:** Directed Energy Deposition

**DMLS:** Direct Metal Laser Sintering

**DS:** Direct Slicing

**EB or EBM:** Electron Beam (melting)

**GMA:** Gas Metal Arc

**MRI:** Magnetic Resonance Imaging

**PA:** Plasma Arc

**PBF:** Powder Bed Fusion

**LPBF:** Laser Powder Bed Fusion

**SEM:** Scanning Electron Microscopy

**SLM:** Selective Laser Melting

**SLS:** Selective Laser Sintering

**THA:** Total Hip Arthroplasty

**TPMS:** Triply Periodic Minimal Surface

## **1 State of Art**

### **1.1 Additive Manufacturing**

Additive manufacturing (AM) is a technology that allows physical components to be made from virtual three-dimensional (3D) computer models by building the component layer-by-layer until the part is complete.

In comparison with subtractive manufacturing processes, in which one starts with a block of material and removes away any unwanted material (either by carving it by hand or by using a machine such as a CNC machine) until one is left with the desired part, additive manufacturing starts with nothing and builds the part one layer at a time by 'printing' each new layer on top of the previous one, until the part is complete. The earliest concepts related to additive manufacturing probably see their origins at the end of the nineteenth century and early of the twentieth century, with the introduction of topographical maps as 3D representations of terrain. For most of the 1990s, the principal term used to describe the layer-upon-layer manufacturing technologies was rapid prototyping, as the principal use of the various technologies was to make concept models and preproduction prototypes. Some other terms that have also been used include solid freeform fabrication and layer manufacturing. In early 2009, however, the ASTM International Committee F42 on Additive Manufacturing Technologies tried to standardize the terminology used by the industry and, after a meeting in which many industry experts debated the best terminology to use, arrived at the term 'Additive Manufacturing.' In their ASTM F2792 10e1 Standard Terminology for Additive Manufacturing Technologies document, they defined additive manufacturing as the "process of joining materials to make objects from 3D model data, usually layer-upon-layer, as opposed to subtractive manufacturing methodologies, such as traditional machining" [1].

Main applications of additive manufacturing include rapid prototyping, rapid tooling, direct part production and other net shape pieces production: the two main parameters of any AM process are type of input raw material and energy source used to form the part [2].

Unlike subtractive manufacturing, where material is removed from a larger block of material until the final product is achieved, most additive manufacturing processes do not yield excessive waste material. It also typically does not require the large amounts of time needed to remove unwanted material, thus reducing time and costs, and producing

little waste [3]. In the Figure 1.1 are shown the general process passages of an additive manufacturing process.

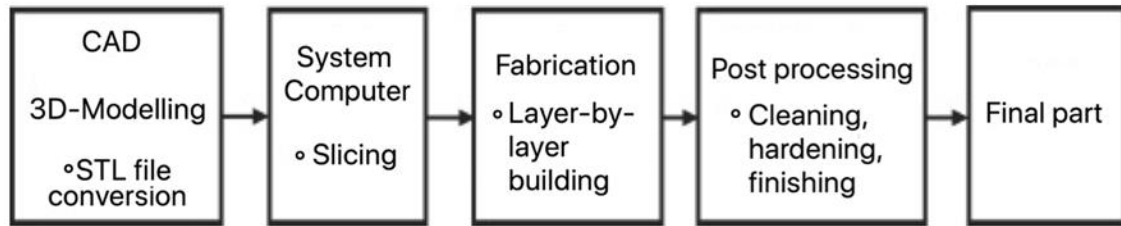


Figure 1.1: Additive manufacturing general process [1]

AM also enables complex and porous structures with specifically designed pores shapes to be produced: the newer field of metal AM has the ability to produce hard to manufacture components in complex structural shapes that are difficult or impossible to fabricate by conventional means.

The 3D printing of metal alloys has its origins in metal powder technology, high-energy beam welding, cladding and prototyping: the processes consolidate feedstock materials such as powder, wire or sheets into a dense metallic part by melting and solidification with the aid of an energy source such as laser, electron beam or electric arc, or by the use of ultrasonic vibration in a layer by layer manner.

These processes fall into two categories defined by ASTM Standard F2792 as Directed Energy Deposition (DED) and Powder Bed Fusion (PBF): both of these technologies can be further classified based on the type of energy source used.

An additional distinction can be made between direct-to-metal AM processes, which begin with a computer model and directly produce a net shaped part and indirect processes that begin with a computer model, print an intermediate part, and then require additional intermediate processing steps such as casting, bulk sintering or machining to attain a net shaped part.

While nearly all applications of AM fabricated metal part require some degree of post processing, heat treatment, and finishing, PBF AM processes, and in many cases DED processes, may be considered direct-to-metal.

In PBF based technologies, thermal energy selectively fuses regions of powder bed and so the density of the final piece is very dense and most of the time we can have net shape pieces that do not require afterwork treatments.

DED processes are often used to produce large rough “blank” shapes requiring extensive machining to create the direct features.



The biggest advantages of the 3D printing are the freedom of design due to the layer by layer technique of creation of the piece, the potential elimination of tooling because of the net shape pieces, the lightweight design, the part consolidation by reducing assembly requirements and the elimination of the production steps because the pieces is totally created from the metal power.

The current disadvantages are the slow build rates, the limited component size depending on the 3d printer, the considerable effort required for application design and for setting the process parameters, the component anisotropy, the dimensional accuracy and the required post treatments like surface finishing [2].

## 1.2 Metal AM techniques

The 3d Printing of the metal alloys covers a wide range of technologies and processes: a further distinction is provided as a function of the primary heat source and so we can now schematize the working principle of the most common AM techniques as shown in the Figure 1.2 [3]:

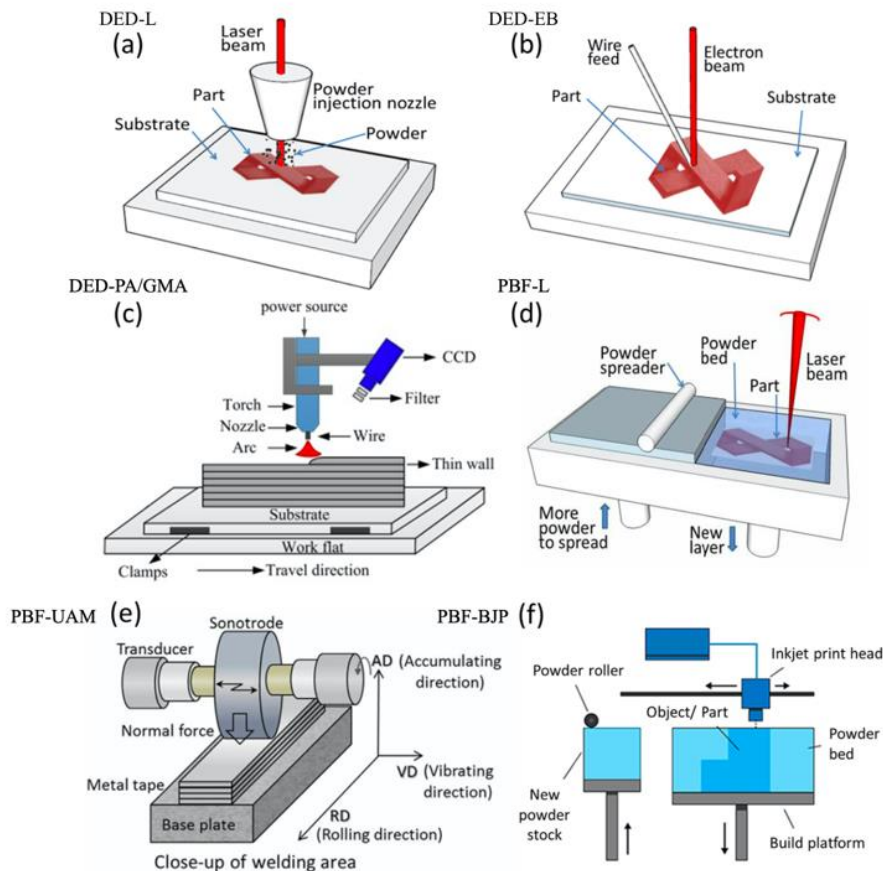


Figure 1.2: Schematization of the most common AM processes [3]

The melt pool properties highly impact the microstructure which is particularly pronounced for thin-walled lattice structures where an elongated grain morphology is observed: the melting process is of crucial importance to guarantee controllability and quality of the manufactured lattice structure.

Moreover, several undesired side effects may occur e.g. a high surface tension gradient in the melt pool leads to splashes during the process and to pores in the final part. Therefore, it is essential to have a qualitative and quantitative understanding to which extent process parameters such as the laser power  $P_l$  and the scanning speed  $v_s$  are interrelated with these physical mechanisms defining the constitution of the melt pool. The AM processes are also characterized by their production times, maximum size of the component that can be fabricated, ability to produce intricate parts and the product qualities such as defects and dimensional accuracy. The production time of the powder-based AM processes is high due to the limitations of powder feeding rate, scanning speed and low layer thickness.

Factors contributing to surface quality for powder-based systems include alloy type, powder shape, size and morphology [4].

Good surface finish and ability to produce intricate features are considered to be the special strength of the powder-based AM processes due to small size of the powder particles. Use of laser and electron beam further allows good dimensional accuracy.

### **1.2.1 Directed Energy Deposition Laser**

The DED-L is a more complex 3D printing process, typically used to repair or add additional material to existing components. It is completely possible to fabricate parts from scratch using this technology, but it is often used for industrial applications to repair existing components.

The DED-L, process shown in the Figure 1.2 (a), typically relies upon the feeding of powder into the melt path and molten pool created by a laser beam to deposit material layer-by-layer or feature-by-feature upon a substrate part or build plate. A shielding gas such as argon is used to protect the molten metal from oxidation and to carry the powder stream into the molten pool. the material is melted at the same time as it's deposited by a nozzle.

This technology is at the frontier of material extrusion and powder bed fusion.

### **1.2.2 Directed Energy Deposition Electron Beam**

The DED-EB, shown in the Figure 1.2 (b), typically consists of a nozzle mounted on a multi-axis arm, which deposits melted material onto the specified surface, where it solidifies. The process is similar in principle to material extrusion, but the nozzle can move in multiple directions and is not fixed to a specific axis. The material, which can be deposited from any angle due to 4 and 5-axis machines, is melted upon deposition with an electron beam: the EB creates a deposit by feeding commercial filler wire into the molten pool. A large vacuum chamber provides a high-purity processing environment during the build and cooling. The process can be used with polymers, ceramics but is typically used with metals, in the form of either powder or wire.

### **1.2.3 Directed Energy Deposition Plasma Arc**

The DED-PA or DED Gas Metal Arc (DED-GMA), shown in the Figure 1.2 (c), is an analogue to the DED-L and DED-EB techniques but it uses an electric arc which is used as the heat source with filler wires as feedstock material similar to fusion welding. These processes consist of the power source, a wire feeding system, and an integrated multi-axis control system for relative movement of the build and the heat source. In all of these DED processes, a 3D part is fabricated in a layer-by-layer manner following the input of a digitized geometry from a computer-aided design (CAD) file.

### **1.2.4 Power Bed Fusion Laser**

Also called Selective Laser Melting (SLM), it is shown in the Figure 1.2 (d). It represents the main process of Power Bed Fusion Laser based technologies: it begins with a solid or surface CAD model, orienting it within a build volume to include support structures, slicing into planar layers, defining a scan path and build-file based upon a pre-specified set of material-specific parameters and the specific machine configuration [5].

The SLM (or PBF-L) technology melts and fuses metallic powders with a powerful laser beam. Once a layer of solid metal is created, the tray holding the 3D print is lowered and powder is layered on top. The sintering with the laser resumes for a new layer. Layer after layer the object is 3D printed, until completion.

With the layer-over-layer process, once a layer of powder has been selectively melted, the building platform is lowered, new powder is deposited and raked

thanks to a levelling blade, and the process is repeated until the object is built [6] as shown in the Figure 1.3:

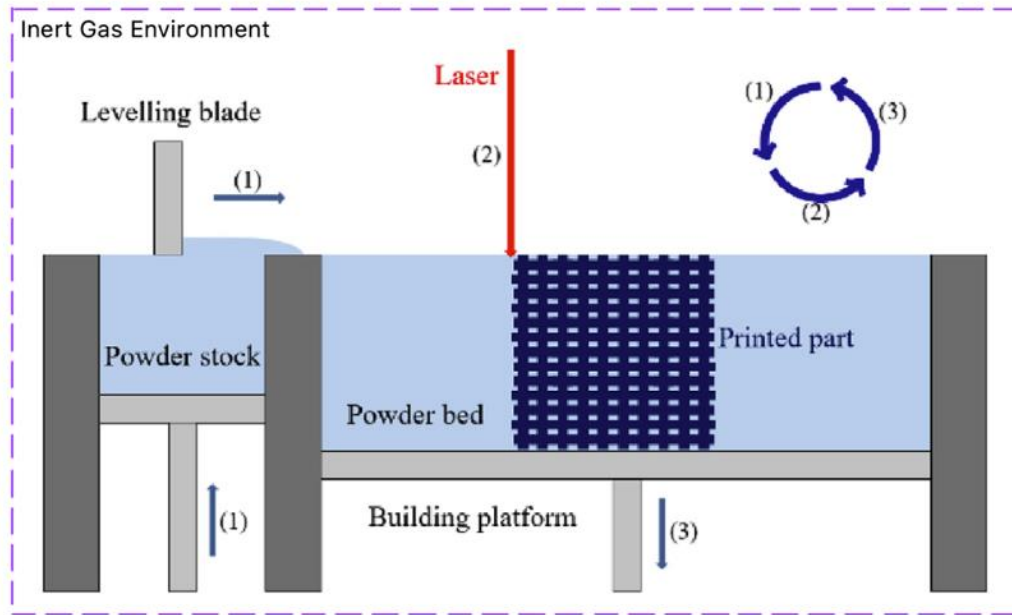


Figure 1.3 Representation of the 3D printing process [6]

Adherence of the current layer to the rest of the part is achieved by re-melting of previous layers. The whole part is produced in a single step, although post-processing such as powder removal, heat treatment or post-machining are required.

The printing characteristics could change depending on different variables:

- The first “macro-variable” is the feedstock quality which determines the properties of the final implant. Powder characteristics, such as size, shape, chemical composition and surface morphology depend on the powder production technique: these influence properties like flowability, apparent density and thermal conductivity of the whole powder bed. Smaller powder particles are used in SLM compared to EBM, leading to a smoother surface finish due to decrease of size of satellites formed during melting and reduction of layer thickness; this is an effect of the overall roughness, which is higher in EBM-manufactured components;
- The second “macro-variable” is defined by the software system: the CAD model represents the ideal final shape of the part to build, but it has to be converted into a Surface Tessellation Format (STL) and sliced into layers in order to generate the manufacturing information for each cross-

section. The conversion CAD-to-STL may represent a source of error with loss of resolution because the STL format simplifies the component geometry into a set of triangular facets connected at the vertices;

- The third “macro-variable” is represented by the hardware of the machine which can have some limitations and so it can affect the quality and the properties of the final piece.

The powder bed is in inert atmosphere or partial vacuum to provide shielding of the molten metal. The Laser is used to scan each layer of the already spread powder to selectively melt the material according to the part cross section obtained from the digital part model. When one layer has been scanned, the piston of building chamber goes downward and the piston of the powder chamber goes upward by defined layer thickness.

The end result of this process is a powder cake and the part is not visible until the excess powder is removed. Build time required to complete a part in PBF based processes is more as compared to DED technologies but, higher complexity and better surface finish can be achieved which requires minimum post-processing. Several parts can be built together so that build chamber can be fully utilized [7]. These processes inherently require support (of same material as part) to avoid collapse of molten materials in case of overhanging surfaces, dissipate heat and prevent distortions. Supports can be generated and modified depending on the part requirements during the pre-processing phase and the same has to be removed by mechanical treatment during post-processing phase [8].

After support removal, the part may undergo post-processing treatments like shot peening, polishing, machining and heat treatment depending on the requirement. Some critical components may even require hot isostatic pressing (HIP) to ensure part density.

This process is characterized by large temperature gradient and rapid cooling rate, which thus result in large columnar grains and superfine basket-weave microstructure. As already reported, the grains prefer to grow parallel to the building direction during the SLM process. These features would inevitably lead to a directional solidification texture and thus an anisotropy of mechanical properties [9].

In practice for the engineering applications of the SLM process, the anisotropy must be carefully considered when designing and building aerospace structural

components: there is a relationship between the mechanical property anisotropy and the microstructure.

The anisotropy has to be considered also because due to the geometry of the samples, the porosity has different shapes in the XY plane and in the XZ plane (or equivalently YZ plane).

The part forms by spreading thin layers of powder and fusing pass-by-pass and layers upon layer of this powder, under computer control, within an inert chamber, incrementally lowering the Z-axis after each layer. Fusion occurs by a raster motion of the laser heat source using galvanometer driven mirrors, resulting in melting and solidification of overlapping tracks.

However, the LPBF process is complex since numerous physical phenomena are involved (heat conduction, melting and resolidification processes, gravitational effects or a highly dynamic melt pool, among others) [5].

### **1.2.5 Powder Bed Fusion Electron Beam**

EBM (electron beam melting) is another PBF based AM process in which electron beam is used to selectively fuse powder bed layer in vacuum chamber.

The PBF-EB is similar to PBF-L but instead uses an EB heat source within a vacuum chamber. The process relies on two-step sequence, first lightly sintering each layer of powder to prevent electro-static charging and repulsion of the powder particles followed by an additional pass fusing the region defined by the part volume.

In both the Laser and Electron Beam process, because of rapid heating and cooling of the powder layer, residual stresses are developed [7].

### **1.2.6 The Ultrasonic AM**

The UAM process, shown in the Figure 1.2 (e), is a solid state additive manufacturing process that sequentially bonds metal foils together using ultrasonic metal welding (USW), layer by layer, and integrates Computer Numerical Control (CNC) machining to remove material to create the desired geometry during this additive build-up process.

The unique nature of the process permits extremely novel functionality to be realised such as multi-material structures with embedded componentry [10].

### **1.2.7 The Binder Jet AM**

The BJ-AM process shown in the Figure 1.2 (f), consists in a liquid binder jet which is supplied by an inkjet printer head and selectively deposited on an alloy powder bed. The binder is cured to hold the powder together to fabricate the component. The delivery of the feedstock material depends on the specific AM process. The part is fabricated layer by layer through depositing liquid binder in the designated regions of each layer until the feature is complete. Due to the use of binder in geometry generation, this process possesses various advantages over the other additive manufacturing technologies including the ability to create colored objects via colored binders, lower cost, lack of melting-induced defects, and its potential capability to print a variety of materials such as metals, sands and ceramics [11].

## **1.3 3D Printing of Lattices**

Additively manufactured lattice structures are popular due to their desirable properties, such as high specific stiffness and high surface area, and are being explored for several applications.

Laser powder bed fusion (LPBF) is a key enabler to manufacture open celled non-stochastic cellular structures like lattices that find applications such as medical implants, impact absorbers, heat exchangers, filters, acoustic absorbers and lightweight structures. On the one hand, they have a high stiffness-to-weight ratio and a broad range of possible applications.

The complexity of lattices challenges the fabrication limits of additive manufacturing processes and thus, lattices are particularly prone to manufacturing defects.

There is a myriad of lattice types available that have unique characteristics (modes of deformation, material efficiency, etc.) and aesthetics. Many of these lattice structures are inspired by naturally occurring crystalline structures [12].

There is a vast array of cell structures, which are individual building blocks in a lattice. Each cell represents a repeatable shape and can come in varying shapes and sizes. Usually, cell structures come in the standard shapes like cubes, stars, hexagons, diamonds and so on: however, many designers can mix and match these shapes to create specific material characteristics for a system.

Lattice structure designs are defined by their unit cell which often falls into one of two categories: strut and surface as shown in the Figure 1.4. Strut-based unit cells consist of a network of often prismatic struts (i.e. constant cross section) connected at nodes,

similar to truss structures. Surface-based unit cells are mathematically defined as the surface connecting set of points for which a given function has a constant value, that is, an iso-surface [13].

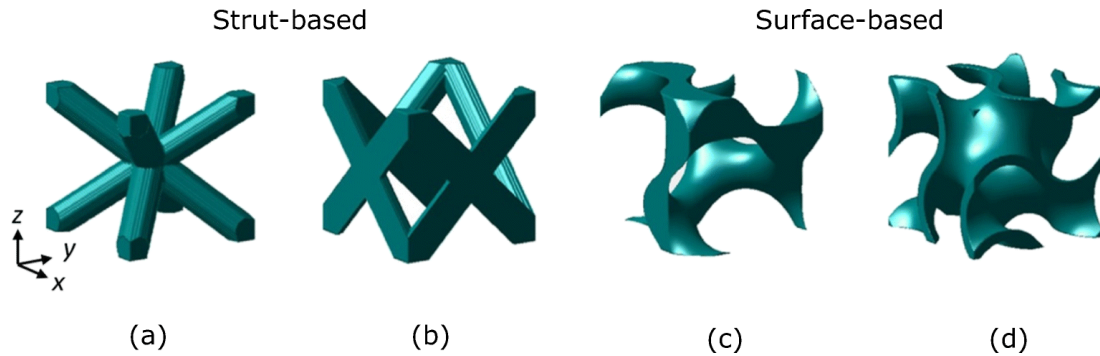


Figure 1.4: a body-centred cubic, b face-centred cubic, c gyroid (skeletal/network), d double gyroid (sheet/matrix) [13]

Unit cell design holds large influence over the mechanical properties of a lattice structure. In strut-based unit cells, the connectivity of the struts, that is the number of struts connected at a given node, greatly controls the structure's behavior under compressive load. For low or high connectivity, unit cells exhibit what is known as bending- or stretch-dominated behavior, respectively.

The main reasons to 3D print lattices are the lightweight arrangements and high strength balance that it can achieve. It also has major aesthetic benefits with its open spaces, complex nodes and a lot more design possibilities. However, there are also structural benefits that go beyond just strength weight or look.

There are generally two paths to improve the strength-to-weight ratio of a given part:

- Through traditional manufacturing, it is accomplished by reducing materials in non-critical areas to optimize the material usage;
- Through latticing, it is possible to put material only in the critical areas of part. Although latticing does reduce the overall strength of the part, the weight savings can improve this strength-to-weight ratio.

By adjusting the thickness and positioning of the nodes, beams or struts, designers can integrate some novel features related to how the component interacts with forces and sound. The use of lattices gives designers far more control over shock absorption, impact control and vibration/noise dampening. Similarly, designers can reduce impact stress or employ elements that act as a sacrificial features which protect the critical components of the object.



The fixation efficacy of 3D printed components strongly depends on the geometric characteristic of the porous structure: a compromise in maintaining the mechanical strength while providing adequate pore size leads to different porous architectures. The majority of the specifications are proprietary but the possible methods to define the 3D porous structures are well established. Typical design strategy for periodic regular networks include the use of CAD tools (libraries of unit cells), image-based structure taken from computed tomography (CT) or magnetic resonance imaging (MRI) data or implicit surfaces solutions, where a single mathematical equation defines the pore shape [14] [15].

These solutions are usually based on a trial-and-error approach, which is why the so-called “topology optimization” have been applied in order to create structures with desired properties satisfying prescribed constraints. In general, the quality and the real dimensions of the mesh may vary significantly depending on design and fabrication process. An example of a unit cell-based highly porous trabecular structure is represented by Trabecular Titanium (TT; Lima Corporate, Udine, Italy (Figure 1.5 (a)): a hexagon-shaped structure developed on three planes. Differently, a stochastic architecture is represented by Tritanium (Stryker, Mahwah, NJ, USA (Figure 1.5 (b)), which is a random interconnected structure with irregular pore size and shape [16] [17].

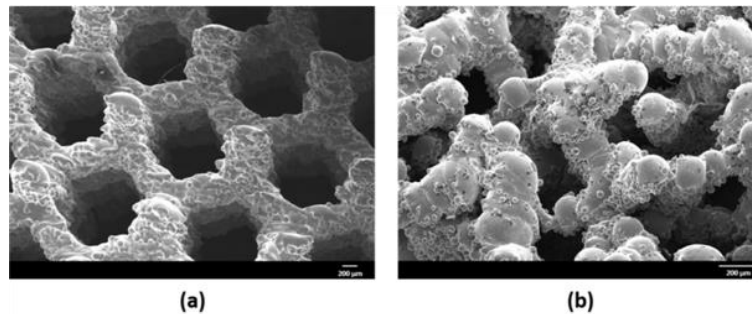


Figure 1.5: Comparison between porous structures [16]

Another classification may take into account the different porous architectures that have been developed: the overall aim is to obtain an open-pore structure in the easiest way possible which satisfy repeatability and homogeneity in order to have a good final product [18].

The general definition of porosity can be thought as the percentage of void space in a solid structure. Porosity (P) can be calculated by the gravimetric method:

$$P = \left(1 - \frac{\rho_{structure}}{\rho_{material}}\right) 100\%$$

## 1.4 Common methods to achieve porosity

The most common method to achieve the porosity is through CAD models: the piece is created with the porosity and so we have a porous 3D model that have to be sliced and printed. Initially, porous structural units are designed by using proper softwares or by using libraries containing different lattice cell porosity types and then the file is converted in order to be read by the 3D printer.

Depending on the application, the porosity can be obtained in different ways which have positive and negative aspects: the most used techniques to create the porosity are analyzed afterwards.

### 1.4.1 Triply periodic minimal surface porous structure

The PBF technique can be used to produce 3D models with good mechanical properties and fine resolution, printing complex structures such as triply periodic minimal surface (TPMS) structures. This technique has been used in a variety of fields such as aerospace, electronics and metal scaffolds in bone tissue engineering. This technology is also capable of fabricating complex porous structures with both micro and macro porosity [19]. An efficient method to create porous microstructures through 3d printing technology is by using triply periodic minimal surface (TPMS) structures: TPMS describes a periodically infinite structure along three independent directions with zero mean curvature of the surface.

These structures can be designed through the following equations:

Gyroid Surface:

$$f(x, y, z) = \cos(x) \sin(y) + \cos(y) \sin(z) + \cos(z) \sin(x) + a$$

Schwartz Diamond:

$$f(x, y, z) = \sin(x) \sin(y) \sin(z) + \sin(x) \cos(y) \cos(z) + \cos(x) \sin(y) \cos(z) \\ + \cos(x) \cos(y) \sin(z) + a$$

Neovius Surface:

$$f(x, y, z) = 3(\cos(x) + \cos(y) + \cos(z)) + 4(\cos(x) \cos(y) \cos(z)) + a$$

D – Prime Surface:

$$f(x, y, z) = 0.5(\sin(x) \sin(y) \sin(z) + \cos(x) \cos(y) \cos(z)) \\ - 0.5(\cos(2x) \cos(2y) \cos(2z) + \cos(2x) \cos(2x)) + a$$

Where the x, y, and z are in the Cartesian Coordinates and the  $\alpha$  variant is the offset value, which can be used to determinate the designed solid fraction.

A computer program called Mathmod has been introduced for TPMS structural analysis and provides support for visualization and manipulation of different TPMS models in multiple dimensions by mathematical equations. The most popular TPMS architectural shape is the Gyroid minimal structure: a network-based Gyroid structure is a solid structure with a single void domain, whereas a sheet-based Gyroid structure has two partitioned, unconnected void spaces [17] as shown in the Figure 1.6 and in the Figure 1.7:

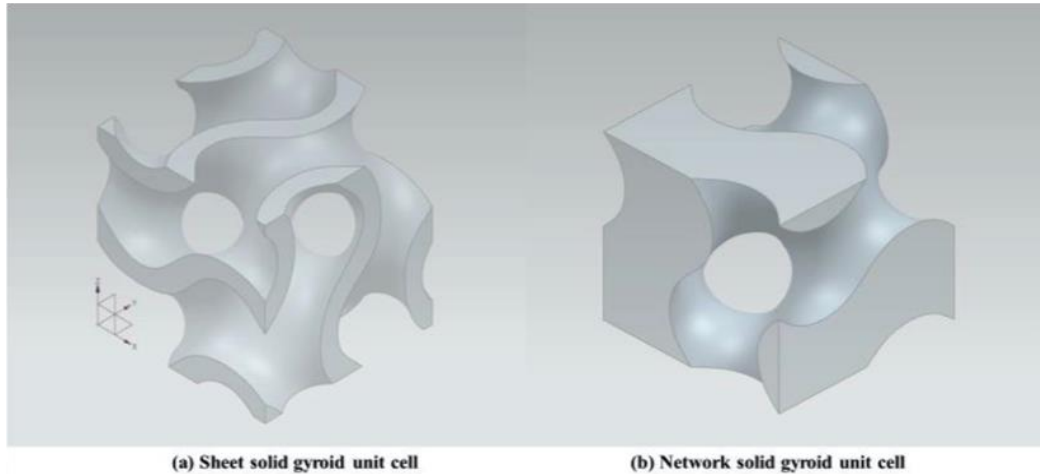


Figure 1.6: Gyroid Comparison [17]

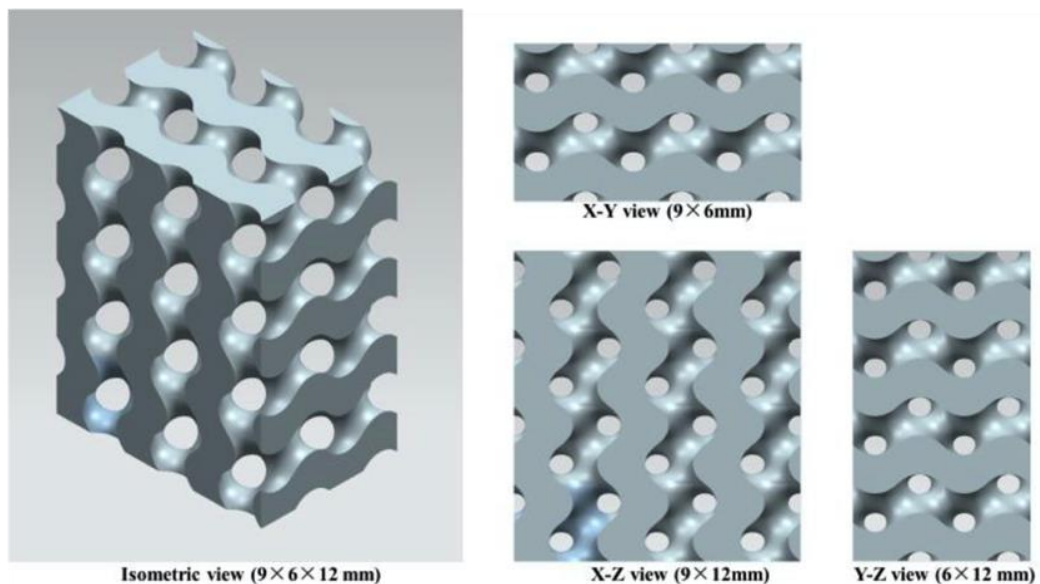


Figure 1.7: Gyroid structure sections [17]

The Gyroid pore shape can be modified to be a deformed Gyroids: the normal Gyroid architecture is associate with spherical pores, where the angle between the

strut and the axial direction is  $45^\circ$ . A deformed gyroid exhibits ellipsoidal-shaped pores with the variable radius in the direction of the longitudinal axis as shown in the Figure 1.8:

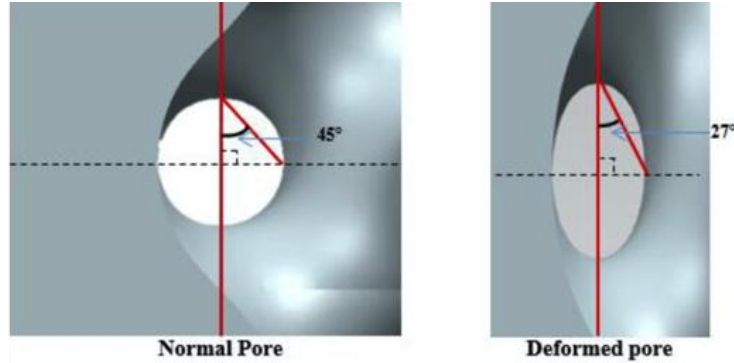


Figure 1.8: Comparison between normal pore and deformed pore [17]

TPMS can be achieved via other methods and it has been recognized as a versatile method of achieving biomorphic porous implant designs. TPMS parts are categorized by their zero-mean curvature at every point and are the subset of the larger class of constant mean curvature (CMC) surfaces. The pore's structure was changed through using three types of TPMS structures: Diamond-type (D), Gyroid-type (G), and Schwartz-type (S). The nodal approximations of the D, G and S are represented in the linear equations described below respectively:

$$D: f(x) = \sin(2\pi x) \sin(2\pi y) \sin(2\pi z) + \sin(2\pi x) \cos(2\pi y) \cos(2\pi z) + \cos(2\pi x) \sin(2\pi y) \cos(2\pi z) + \cos(2\pi x) \cos(2\pi y) \sin(2\pi z) - K$$

$$G: f(x) = \cos(2\pi x) \sin(2\pi y) + \cos(2\pi y) \sin(2\pi z) + \cos(2\pi z) \sin(2\pi x) - K$$

$$S: f(x) = \cos(2\pi x) + \cos(2\pi y) + \cos(2\pi z) - K$$

And so the Porosity Level ( $PL$ ) is respectively:

$$PL_D = 42.284K + 50.12$$

$$PL_G = 32.783K + 50.118$$

$$PL_S = 28.742K + 49.998$$

Constant  $K$  effectively controls the porosity level of the resulting lattice structures. The relationship between  $K$  and the porosity level is unique for each TPMS. For Diamond, Gyroid and Schwartz, the porosity level can be reasonably approximated in a range between 0.1 and 0.9 [20].

To represent the TPMS as the nodal surface, the coordinates of each given surface were created using K3dSurf v0.6.2 software (Figure 1.9 a, b, c). Then, Geomagic Studio 12 (3DSystems, Rock Hill, USA) was used to recreate the surfaces, which

serve as the boundary between solid and void material and to generate solid structures (Figure 1.9 d, e, f) [21]:

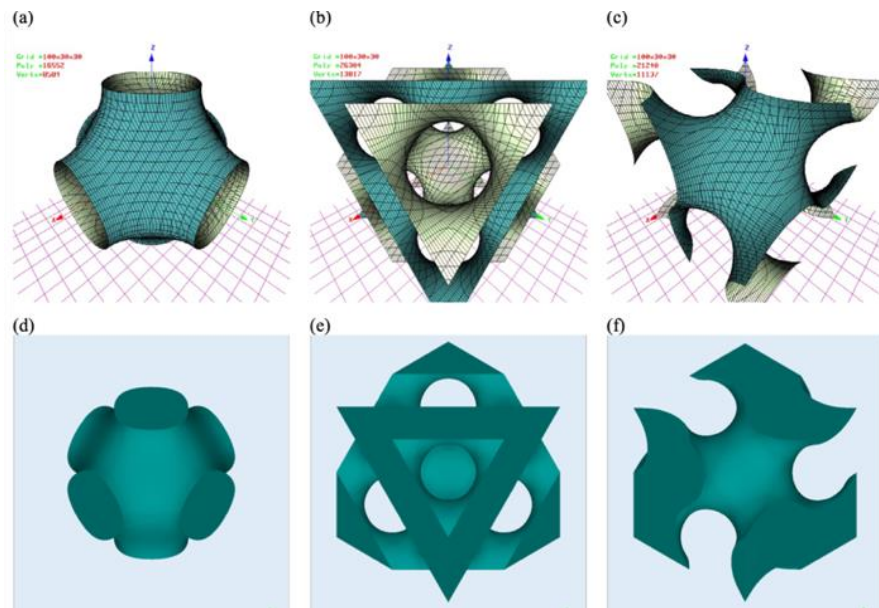


Figure 1.9: *K3dSurf Nodal Surface Representation (a, b, c)*  
*Geomagic Studio Surface Representation (d, e, f) [20]*

### 1.4.2 Boolean intersection porous structure

The LPBF technique was proposed to fabricate the porous metals with different pore structures, porosities, and materials. SLM can directly fabricate porous microchannel structures and effectively reduces the fabrication process of the microchannel catalyst support, thus improving the production efficiency. Through the studying of the unit structure of the used metal, we are able to design porous structures on the basis of an array of repeating units (nevertheless, other types of porous structures can also be explored). Through the Grasshopper tool, which is a parameterized design plug-in based on the 3D design software Rhinoceros, there is the possibility to design and fabricate the porous supports thanks to a method based on parametric design [22].

Through this technique, it is possible to create a porous structure generated by a single closed entity from a Boolean intersection between bodies [15].

The continuous structure of the curve was inspired by the Hilbert curve: the characteristic of the Hilbert curve is that by increasing the order, an infinite length curve can fill a certain size area.

It is easy for the model to approach the manufacturing limit of the size. The idea of modeling is to build a high-order two-dimensional plane curve first, and then scan each layer of curve into a continuum along the z-axis array [4].

### 1.4.3 Porosity for Dental implant

Laser Beam Melting (LBM) 3D printing is an AM technique which can allow the fabrication of porous Ti<sub>6</sub>Al<sub>4</sub>V with complex geometries for a wide range of applications. In Particular in reference [23], for dental implant were studied prototypes with three controlled pore sizes (200 μm, 350 μm and 500 μm). The porous architecture is directly made from a computational model and the generated porous scaffold structure is homogeneous regarding the pore size:

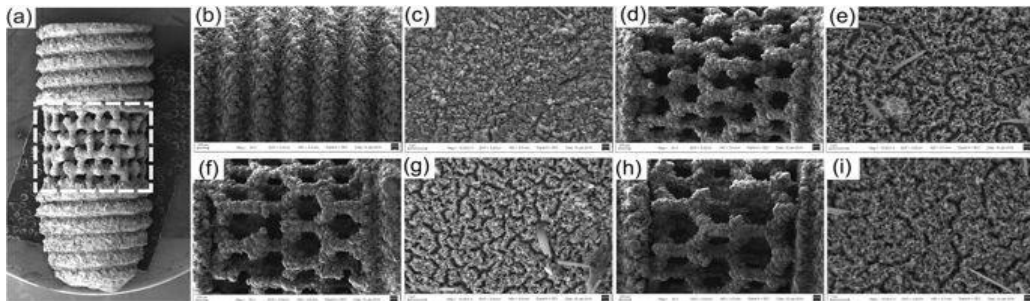


Figure 1.10: Porous Structure of a Dental Implant [23]

The Figure 1.10 shows a general pattern of one kind of porous structured implant. The mid-piece area marked with a white frame is modified into 4 types of architecture (200 μm, 350 μm and 500 μm pore sized and screw-typed structure). These have been observed and analysed with the SEM first at low magnification (Figure 1.10 b, d, f, h) and after at high magnification (Figure 1.10 c, e, g, i). The nano-sized burr-like on the implant surface are generated during the alkali heat treatment to achieve a further nano-modification. Screw thread and porous structure of implants were pre-defined by NX Unigraphics and layered printed with the selective laser melting solution (SLM).

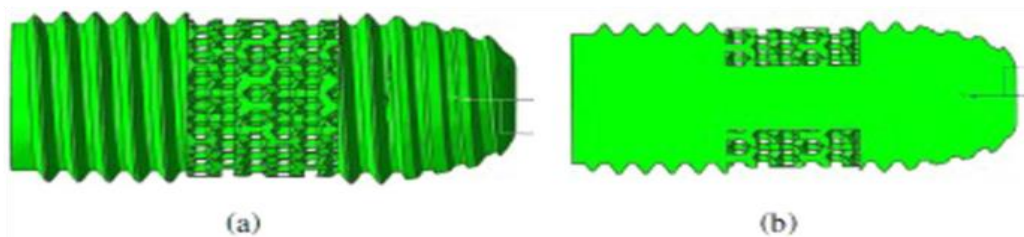


Figure 1.11: Section of the Dental Implant [23]

#### 1.4.4 Nickel nanostructures porous technique

AM of nickel nanostructures is a technique which synthesizes hybrid organic–inorganic materials that contain Ni clusters to produce a metal-rich photoresist, then two-photon lithography is used to sculpt 3D polymer scaffolds, and pyrolyze them to volatilize the organics, which produces a >90 wt% Ni-containing architecture.

It is possible to realize nanolattices with octet geometries, 2  $\mu\text{m}$  unit cells and 300–400 nm diameter beams made of 20 nm grained nanocrystalline, nanoporous Ni. Most existing methods for additive manufacturing (AM) of metals are inherently limited to 20–50  $\mu\text{m}$  resolution, which makes them untenable for generating complex 3D printed metallic structures with smaller features.

Using this approach, the authors demonstrated the fabrication of periodic Ni octet nanolattices with the unit cell size of 2  $\mu\text{m}$  and beam diameters of 300–400 nm diameter as a proof-of-concept. TEM analysis revealed that the microstructure of Ni beams is nanocrystalline and nanoporous, with a 20 nm mean grain size [24] as shown in the Figure 1.12:

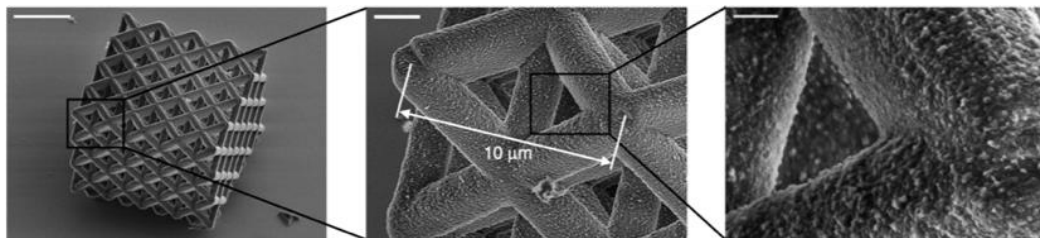


Figure 1.12: TEM analysis of Nanoporous Structure [24]

## **1.5 Conclusions**

The methods that we have analyzed in the chapter 1.4.1, 1.4.2, 1.4.3 and 1.4.4 are able to produce a porous model with a very high homogeneity level because of the utilization of CAD to design porosities with a defined geometry: the pieces are then converted in the STL format, so that the surface is approximated with series of triangles, and printed (except for the last method that uses a complicated series of thermal and chemical reactions to create nanopores).

The conversion to STL file, leads to geometrical approximations and thus to geometrical errors: a drawback is then the low surface quality because of the triangles which approximate the surface. Additionally the bigger the surface the larger the size of the files, and it means that a lot of data have to be handled [25].

To create a volume with a relatively simple geometrical porosity, the methods we have analyzed are not adequate enough because these would require a large number of data to be processed, and so we should introduce the Direct Slicing (DS) approach.

This technique consists in modifying some process parameters in order to achieve the desired level of porosity without designing any porosity through CAD.



## 2 The strategy of development of the 3D lattices

### 2.1 Porosity through process parameters

The porosity through the process parameters is based on the Direct Slicing (DS) approach: this process consists in modifying the process parameters in order to create a “controlled error” and so a lack of material in some areas in order to achieve the desired porosity. The interaction between the laser beam and the powder bed is dependent on various influencing parameters such as:

- Laser power: it is the energy delivered by the laser per unit of time;
- Hatch distance: it is the space between adjacent tracks;
- Layer thickness;
- Scan speed: it indicates how fast is moving the laser to complete a layer.

The main reason for the direct slicing approach is the limitation of the existing data preparation because of the geometrical simplicity of the component which is not converted in a series of plane faces as shown in the Figure 2.1:

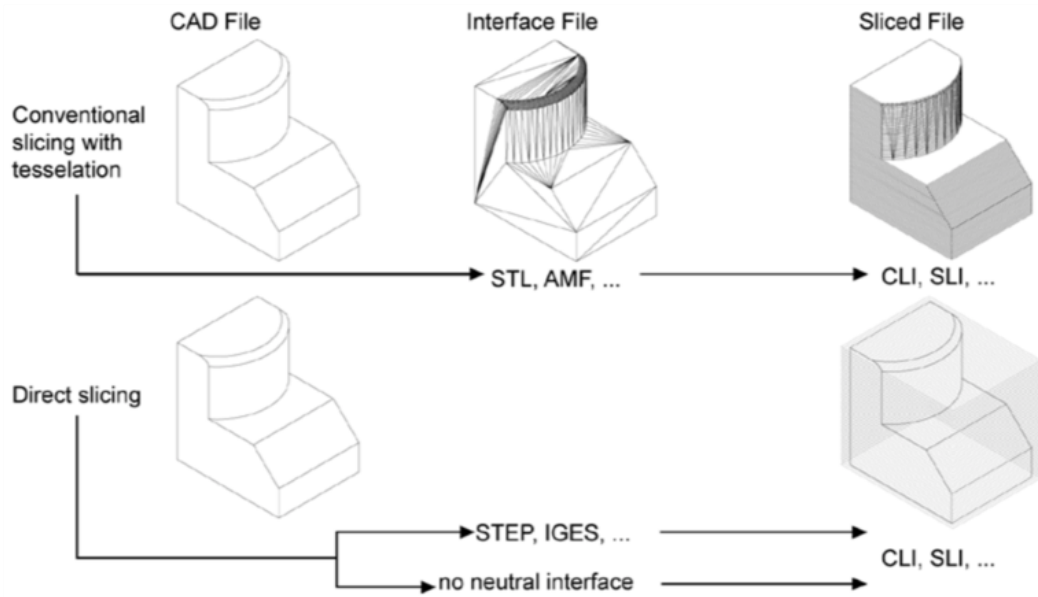


Figure 2.1: Comparison between CAD to Sliced and Direct Slicing file [26]

By using the DS approach, we want to combine a defined geometry with specific process parameters: in this case, we want to create the porosity by setting individual hatch lines (weld beads) in one plane which do not touch one another laterally.

Ideally, the weld beads only touch each other in height (z-direction) creating some cantilever weld beads so that in between them, very small and regularly-distributed empty volumes remain in [26] as shown in the Figure 2.2:

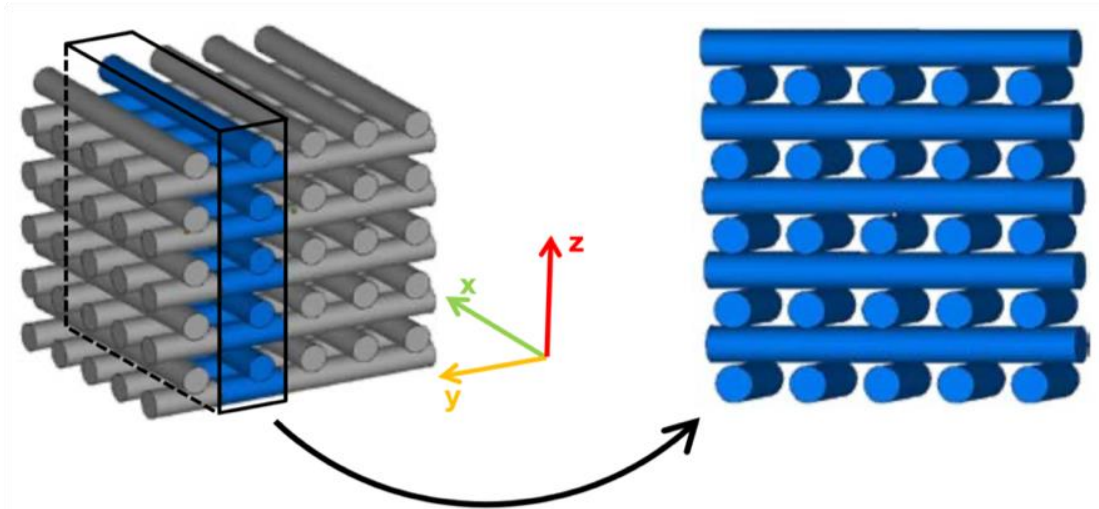


Figure 2.2: Porosity due to process parameters [26]

In practice it is not possible to manufacture these ideal line grid structures due to the lack of heat dissipation to the underlying layer: the melt pool of each weld beads grows in height until it touches the one above it. Nevertheless, small holes remain in these areas by adjusting the process parameters: generating the individual hatch lines is indeed defined but the exact pore size and shape depend on a number of effects difficult to control.

With DS, the geometry is sliced in the CAD system, and the necessary polygons are only generated in each layer. In this step, the number of necessary points in each layer can also be reduced, because straight lines only require one start- and endpoint instead of mid-line points in the STL-file. To conclude the number of points in one layer is reduced, and they can be used to create more accurate polygons of curved segments [27] [28] as shown in the Figure 2.3:

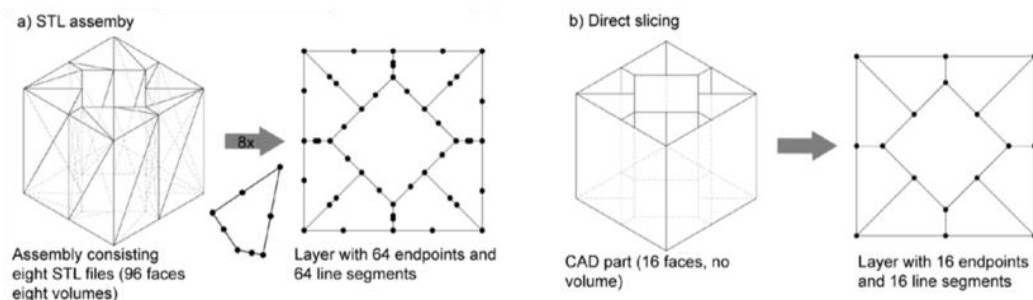


Figure 2.3: Comparison of .STL assembly and Direct Slicing [27]

The initial idea is to create by CAD a homogeneous model without porosity, that has to be made using the exposure strategies of the machine manufacturer (Direct Slicing) with specific settings in order to create an alternative exposure strategy for the laser.

In summary, a number of advantages of the DS approach can be identified: the main reason for this approach is that the .STL format is not able to export surface models and for this reason especially, this way of directly exporting slice data was developed.

With DS, the number of generated process files is reduced because STL files are not required: this reduction simplifies the process, because fewer files and versions have to be handled. In addition, part quality can be enhanced because there is no geometrical approximation of the surface.

Furthermore, the native CAD geometry must not be tessellated before slicing [26].

These 3D printing processes are guided by Computer-Aided-Design (CAD) files containing the model of the part to manufacture.

Our research led us to deeply study and develop the method analyzed in the chapter 2.1 looking for an alternative method to obtain a good level of porosity with the same requirements, bypassing the drawbacks of the conversion between CAD and STL.

## 3 Materials and Methods

### 3.1 Component design

For the design of the cubes and to set the printing parameters we use the software Materialise Magics: this tool is a data preparation and STL editor software for Additive Manufacturing that allows us to convert files to STL, repair errors, edit our design and prepare our build platform. Materialise Magics has the tools we need to duplicate parts, orient them in an ideal way, generate support for metal and create no-build zones.

### 3.2 3D Printing technology

The LPBF machine used for our experiment is a Renishaw AM250 RBV (reduced build volume), with a maximum power of 200W and a laser source with wavelength of 1070 nm and a working volume of 250x250x300 mm<sup>3</sup> (Figure 3.1 and Figure 3.2).

This AM system features a patented vacuum build preparation system to rapidly reduce the oxygen level, before re-pressurizing the system with inert processing gas, creating class-leading processing conditions. It was used with an additional RBV (reduced build volume) device capable of working with very small amounts of powder (to prevent waste of powder), facilitating the test and production of non-standard materials. The RBV allows us to enable rapid real time testing and development of parameters, speeding up our research.



Figure 3.1: Renishaw AM250 [29]

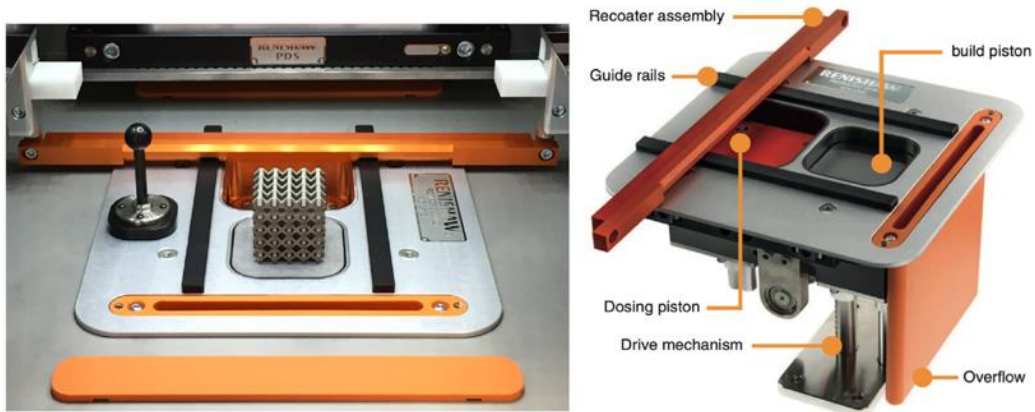


Figure 3.2: Renishaw RBV device [29]

A robust process chamber prevents process gas pressure loss, leading to unmatched low process gas consumption. This economic use of process gas helps maintain uniform processing conditions and reduces waste and cost of ownership [29].

The Reduced Build Volume (RBV) is designed for users who wish to easily change between materials for the purpose of materials development and experimentation.

Once the RBV is removed, the machine functions as a normal full-size AM system.

The main parameters of the LPBF printer are the powder layer thickness which is between 20  $\mu\text{m}$  and 100  $\mu\text{m}$  and the maximum available laser power which is 200 W.

The models, to test the different printing parameters, are cubes with dimensions 10mm x 10mm x 10mm: the cubes are set with no edges, no up-skin and no down-skin.

The default settings for the printing are described in the Table 3.1 and showed in the Figure 3.3:

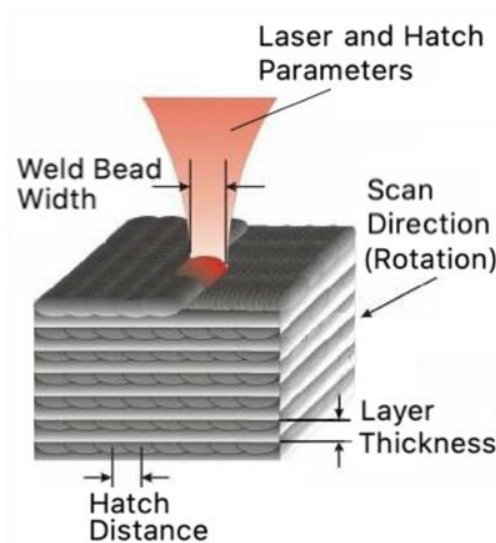


Figure 3.3: Printing scheme

Process Parameter	Abbreviation	Default Value
Weld Bead width	w <sub>b</sub>	150 μm
Hatch Distance	H <sub>d</sub>	95 μm
Layer Thickness	Z	60 μm
Rotation	α	90°
# Consecutive Layers Equally Oriented	n	1
Laser Parameter	Abbreviation	Default Value
Laser Power	P <sub>l</sub>	200W
Exposure Time	t <sub>e</sub>	70 μs
Point Distance	P <sub>d</sub>	60 μm
Focus	f	0 μm

Table 3.1: Default printing parameters

### 3.3 Material

The Ti6Al4V alloy powder is the metal used in our investigation: it comprises titanium mass fraction up to 90% alloyed with aluminium up to 6.75% and vanadium up to 4.5%, along with other minor elements [29].

This alloy is also known as Ti64, and it is an  $\alpha + \beta$  titanium alloy with high strength, low density, high fracture toughness, excellent corrosion resistance and superior biocompatibility.

Recognized as the most popular titanium alloy, Ti6Al4V occupies almost a half of the market share of titanium products used in the world today.

It features good machinability and excellent mechanical properties and it is one of the most common used Titanium alloy due to its biocompatibility, mechanical strength, corrosion resistance and general properties [30]. The Ti6Al4V alloy offers the best allround performances for a variety of weight reduction applications in aerospace, automotive and marine equipment [31].

### 3.4 Experimental procedures

After printing the samples are first roughly cleaned from the powder with a brush and then, to remove almost all the metal powder inside the porosities, they are put in a glass vessel filled with water and subject to the ultrasounds cleaning.

Analyses of the lattice samples are carried out by macroscopic and microscopic observations:

- The observation of the morphological features of the 3D lattice is made by the optical microscope, shown in the Figure 3.4 (a), with a low magnification in order to analyze the porous macrostructure and the inner porosity of the samples;
- The microscopic observation is made by the Scanning Electron Microscope (SEM), shown in the Figure 3.4 (b), to analyze the microstructure of the sample, the weld tracks, the metal grains and the melt pool formed during the printing.

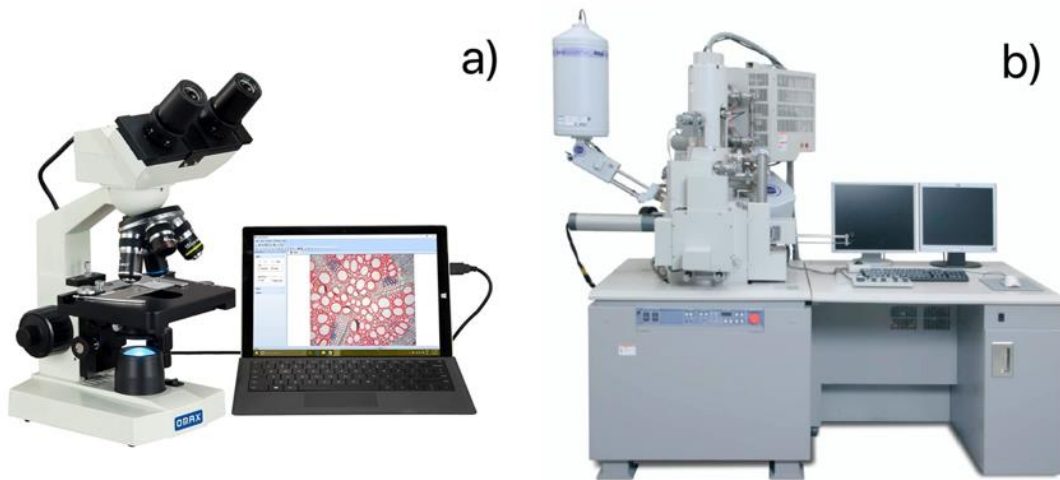


*Figure 3.4: Scanning Electron Microscopy*

The main SEM components include:

- Source of electrons;
- Column down which electrons travel with electromagnetic lenses;
- Electron detector;
- Sample chamber;
- Computer and display to view the images.

Electrons are produced at the top of the column, accelerated down and passed through a combination of lenses and apertures to produce a focused beam of electrons which hits the surface of the sample. The sample is mounted on a stage in the chamber area and, unless the microscope is designed to operate at low vacuums, both the column and the chamber are evacuated by a combination of pumps.

The level of the vacuum depends on the design of the microscope.

The position of the electron beam on the sample is controlled by scan coils situated above the objective lens. These coils allow the beam to be scanned over the surface of the sample. This beam enables information about a defined area on the sample to be

collected. As a result of the electron-sample interaction, a number of signals are produced: these signals are then detected by appropriate detectors.

The scanning electron microscope (SEM) produces images by scanning the sample with a high-energy beam of electrons. As the electrons interact with the sample, they produce secondary electrons, backscattered electrons, and characteristic X-rays. These signals are collected by one or more detectors to form images which are then displayed on the computer screen. When the electron beam hits the surface of the sample, it penetrates the sample to a depth of a few microns, depending on the accelerating voltage and the density of the sample. Many signals, like secondary electrons and X-rays, are produced as a result of this interaction inside the sample.

The maximum resolution obtained in a SEM depends on multiple factors, like the electron spot size and interaction volume of the electron beam with the sample. While it cannot provide atomic resolution, some SEMs can achieve resolution below 1 nm. Typically, modern full-sized SEMs provide resolution between 1 nm and 20 nm whereas desktop systems can provide a resolution of 20 nm or more.

### **3.5 Metallographic analysis**

Metallography is the study of the macrostructure and of the microstructure of various metals. To be more precise, it is a scientific discipline of observing the microstructures of metals, and as such is crucial for determining product reliability [32].

#### **3.5.1 Cutting**

After the morphological analysis at the SEM the samples are ready for the metallographic analysis.

This analysis is made in order to understand the porosity along sections of the samples at the macrostructure and microstructure levels.

The cut is made by using a precision cutting tool with a diamond disc which rotates at about  $120 \div 150$  *Rotation/min*, cooled with a solution of water and oil as shown in the Figure 3.5 :



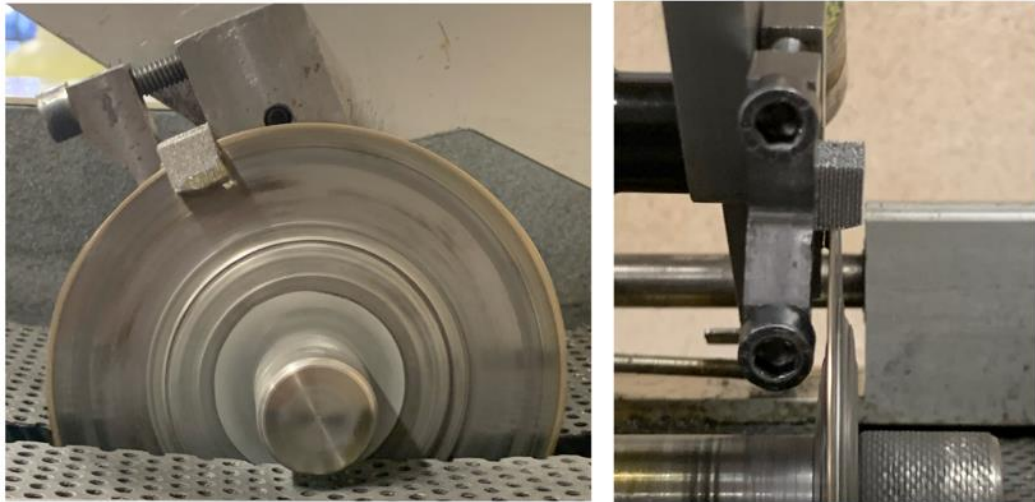


Figure 3.5: cutting process

This Low Speed cutting machine is a precision sectioning tool that is designed for cutting various types of materials with minimal deformation. This low speed precision cutter is targeted for delicate or small parts by only using gravity fed force with a minimal deformation.

### 3.5.2 Mounting, grinding and optical analysis

The sections, to be studied, are then mounted in a polymer for convenience in handling, to protect the edges and in order to fill the pores to facilitate the studies. This process protects the material's surface, fills voids in damaged (porous) materials, fills the porosities and improves handling of irregularly shaped samples. There are plenty of ways to conduct this operation, and all of them depend on the type of material that is being handled. So, there are: thermosetting mounting resins and castable mounting resins.

The most used method to embed the metal pieces are:

- The hot method: it consists on the utilization of a hot mounting press machine which embed the metal pieces in a polymer powder that melts by using high pressure and high temperature;
- The cold method: it consists on embedding the metal samples by using Epoxy Resin which is a high quality resin: this resin is obtained mixing 2 parts of powder epoxy and 1 part of liquid hardener for a 2:1 ratio.

The next procedure is the grinding: the entire process is designed to produce a scratch free surface by employing a series of successively finer abrasives, up to the mirror polishing in order to highlight the structure: we start with a paper of

grain size 320 up to arrive to a grain size of 2500. After this grinding process, we polish the sample to make it reflective by using rotating discs covered with soft cloth.

To highlight the metal micro-structure, the surface has to be attacked with a mixture made of the 88% of H<sub>2</sub>O, the 9% of HNO<sub>3</sub> and the 3% of HF. The sample are put in contact with this liquid for a period of time between 15 and 25 seconds (the more the contact time, the more the contrast in the surface, paying attention to don't ruin the sample).

The piece is then ready to be analyzed at the optical microscopy in order to check the porosity (the macrostructure) and the microstructure.

### **3.6 Compression tests**

The compression test is the test in which the material experiences opposing forces that push inward upon the specimen from opposite sides. The test sample is generally placed in between two plates that distribute the applied load across the entire surface area of two opposite faces of the test sample and then the plates are pushed together by a universal test machine causing the sample to flatten. A compressed sample is usually shortened in the direction of the applied forces and expands in the direction perpendicular to the force.

The goal of a compression test is to determine the behavior or response of a material while it experiences a compressive load by measuring fundamental variables, such as, strain, stress, and deformation. By testing a material in compression the compressive strength, yield strength, ultimate strength, elastic limit, and the elastic modulus among other parameters may all be determined. With the understanding of these different parameters and the values associated with a specific material it may be determined whether or not the material is suited for specific applications or if it fails under the specified stresses: such information is important in the analyses of structural properties when materials are subject to compressive or bending loads and of metal working and fabrication processes that involve large compressive deformation such as forging and rolling.

Compression tests were performed with a MTS Alliance RF150 electromechanical testing machine (Figure 3.6) and those tests are made:

- with a compression rate of 0,0833 *mm/s* (= 5 *mm/min*);
- With a data acquisition rate of 50 Hz;
- Without extensometer due to the low size of tested specimens;

- Three specimens tested per condition.

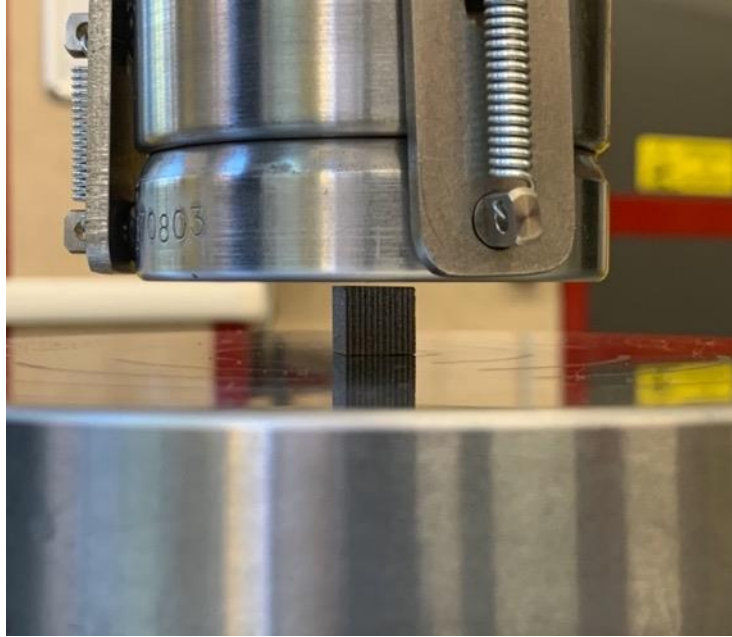


*Figure 3.6: Compression Tests Machine*

## 4 First Printing

For the first printing we firstly create a defined geometry with different process parameters in order to obtain different size of porosities by making individual hatch lines (weld beads) in one plane that have not to touch one another laterally: The Idea is that the porosity is created because the weld beads only touch in height (z-direction) [33] as shown in the Figure 4.1:

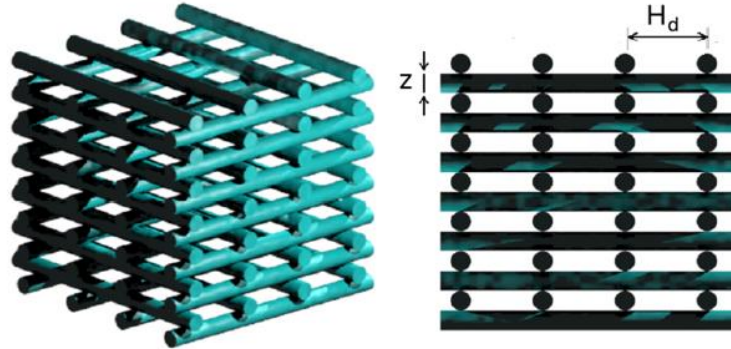


Figure 4.1: Porosity Ideal Structure [33]

The latter method can be modified and improved by developing a ‘beam overlap’ technique for the manufacturing of a different porous structure [34].

The CAD file representing the component geometry has to be modified in order to be sliced into thin horizontal layers with the scanning strategy described in the Figure 4.2:

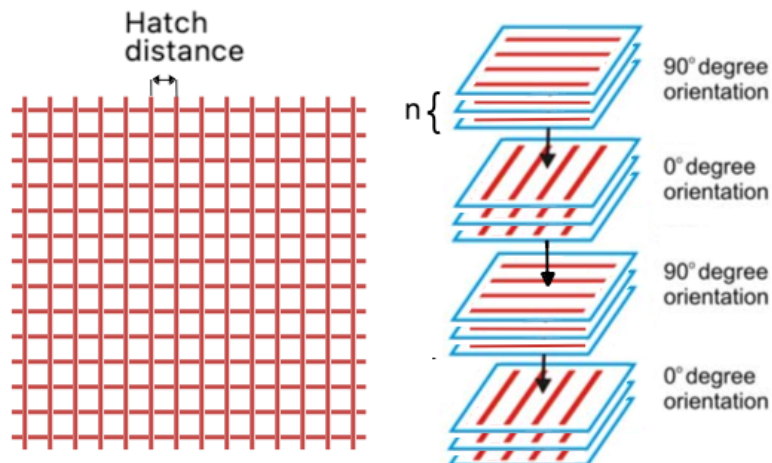


Figure 4.2: Scanning strategy [34]

These parts were created by selecting the laser processing parameters to produce walls of the thickness  $d_{wt}$ , and hatch spacing  $d_{hs}$ , so that there was no overlap between the individual scan lines. In order to produce the desired pore depth, each layer was repeated

a number of times  $n$  until the desired wall height  $d_{hh}$ , was obtained as shown in the Figure 4.3.

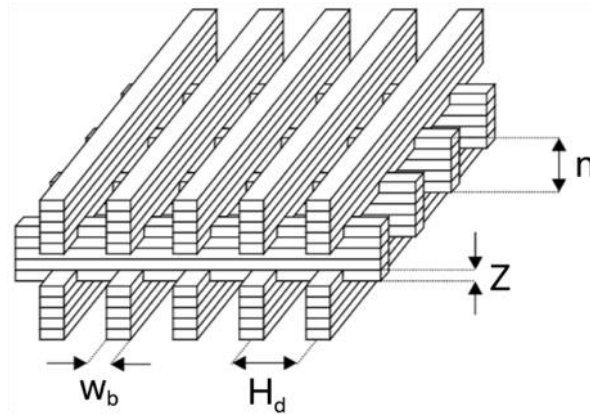


Figure 4.3: Beam Overlap structure [35]

The process of LPBF has many adjustable variables, which taken together with the possible variation in design that can be printed, has created even more possible variables in the final product that must be understood if we have to predict the performance of the 3D lattices [35].

For the first printing we set 7 cubes as shown in the Figure 4.4:

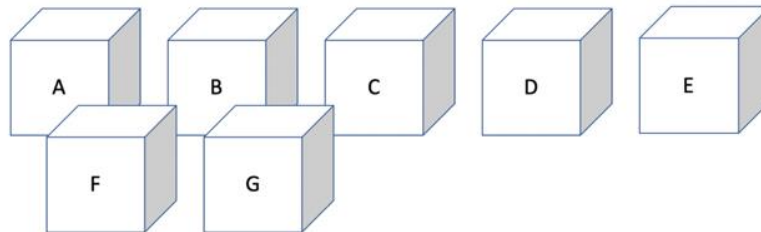


Figure 4.4: first printing setting

Cube Position	Sample Name
<b>A</b>	H400
<b>B</b>	H600
<b>C</b>	H800
<b>D</b>	H1000
<b>E</b>	H1200
<b>F</b>	H800_o_90_n10
<b>G</b>	H800_o_90_n5

Table 4.1: 1<sup>st</sup> printing

The samples **A**, **B**, **C**, **D** and **E** are made with the rotation of  $90^\circ$  for each layer ( $n = 1$ ) and with the default settings except for the hatch distance that is changed so that for H400 it is  $H_d = 400 \mu m$ , for H600 it is  $H_d = 600 \mu m$  and so on.

The samples **F** and **G** are made with the “Beam overlap technique” by overlapping respectively 15 and 30 beams oriented at  $0^\circ$  and  $90^\circ$  (so that  $n_F = 10$  and  $n_G = 5$ ).

Since in a single printing it is not possible to change the Z parameters (we can't print simultaneously samples with different heights) in the second printing we will try to create the porosity by varying the Z parameters.

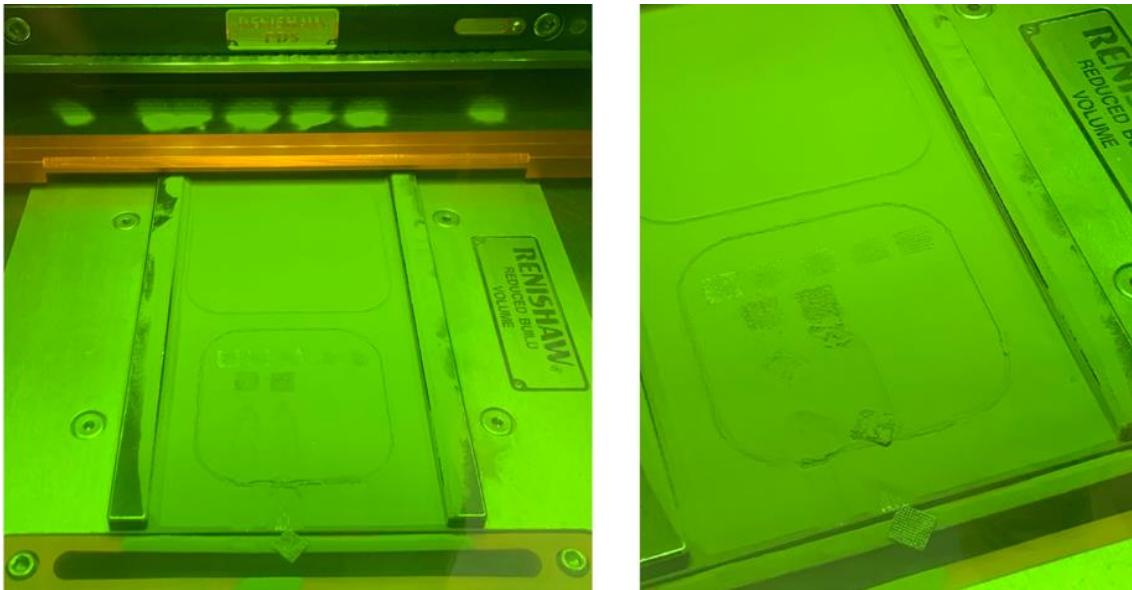


Figure 4.5: 1st Printing

As shown in the Figure 4.5 during the printing we had some detachment problems so that the samples F and G detached and so we had to stop the printing of these samples. The detachment problems maybe happen because of the shrinking after the melting of the powder and because of the residual stresses due to the fact that the surface that touches the building plate is very little.

Nevertheless we have to check if this problem will occur again in order to better understand the cause of the problem.

## 4.1 H400

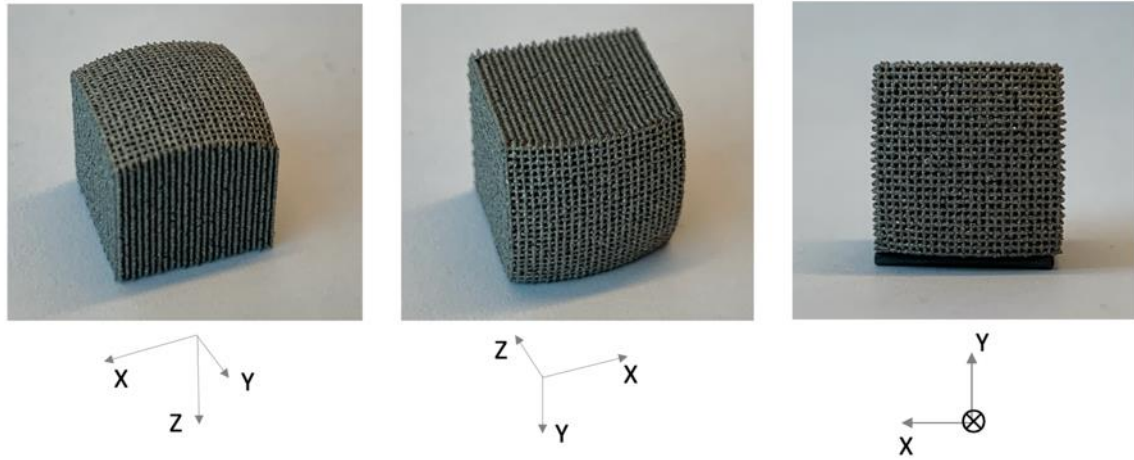


Figure 4.6: H400

As we can see in the Figure 4.6, there is a side which is curved: this is the base of the cube facing the building plate that during the printing partially separated from the substrate and bent due to the effect of shrinkage thermal stresses.

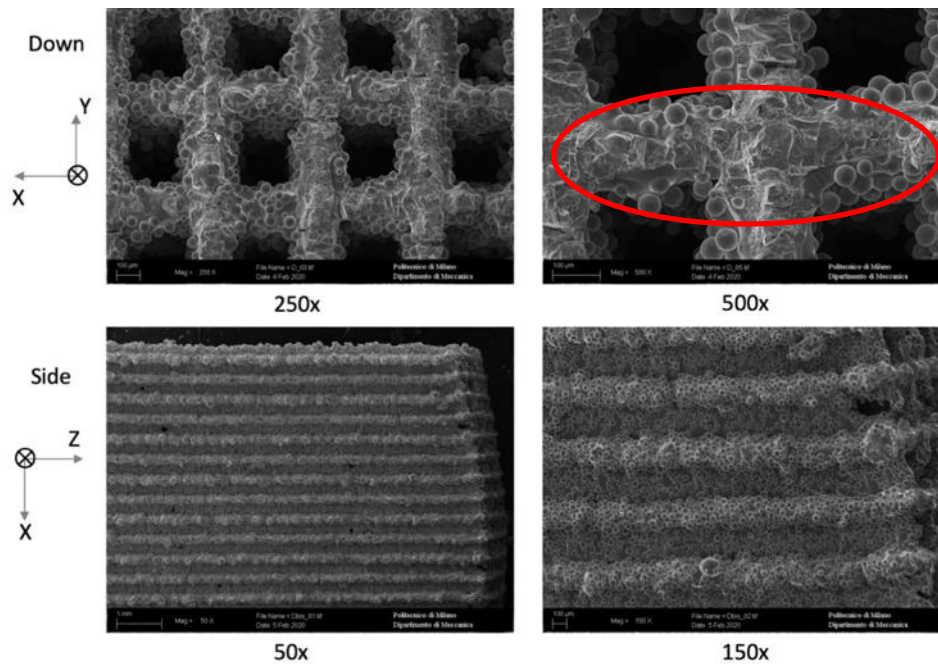


Figure 4.7: SEM analysis of H400

As we can see in the Figure 4.7 , taken by SEM, the first layer, as circled in the figure at the top right, is full of fractures because it detached from the printing plate but we have created a good unidirectional porosity, while in the side we have no porosity and so we have to change either the process parameters or the printing technique.

## 4.2 H600, H800, H1000 and H1200

The following figures show respectively the samples **B** (H600), **C** (H800), **D** (H1000) and **E** (H1200) where only the hatch distance is varied and they showed the same structure of the sample **A** (H400) just analyzed (chapter 4.1).

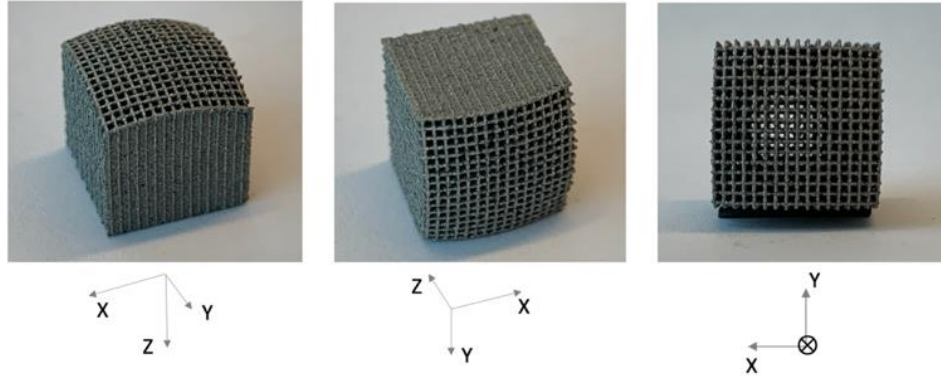


Figure 4.8: H600

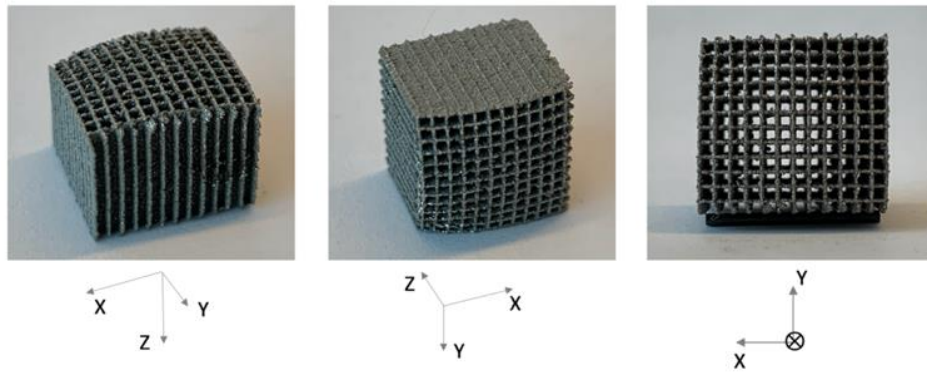


Figure 4.9: H800

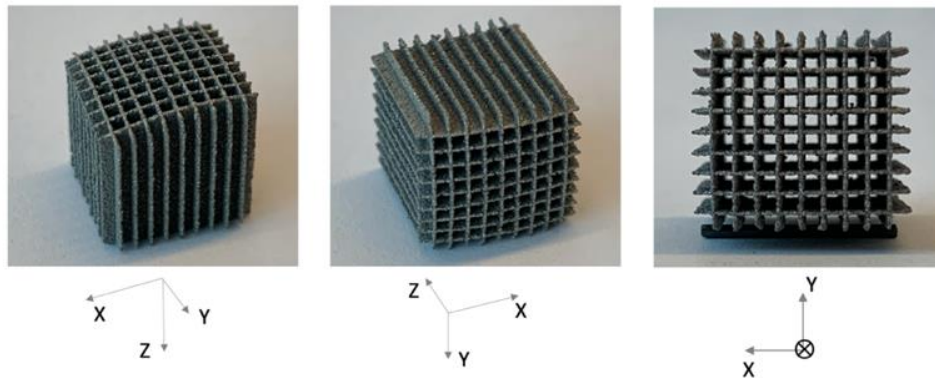


Figure 4.10: H1000



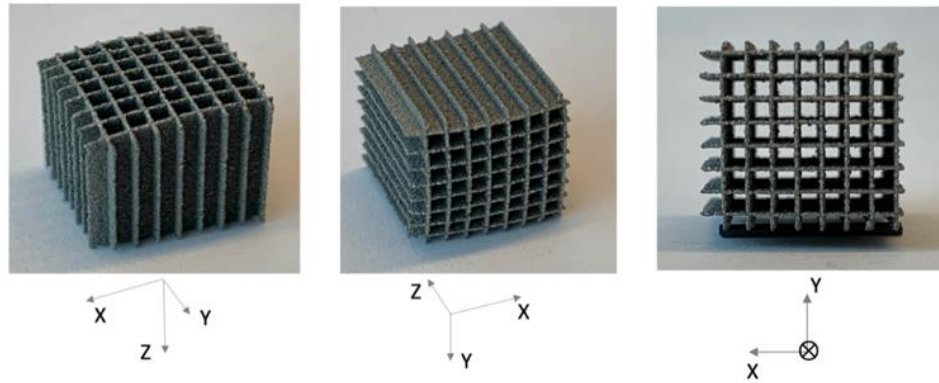


Figure 4.11: H1200

The base of the cube facing the building plate is curved for all of these samples and the first layer is full of fractures as previously shown in the Figure 4.7.

In the side we have either no porosity or a random porosity which can be considered a printing defect and so we have to change either the process parameters or the printing strategy.

### 4.3 H800\_0\_90

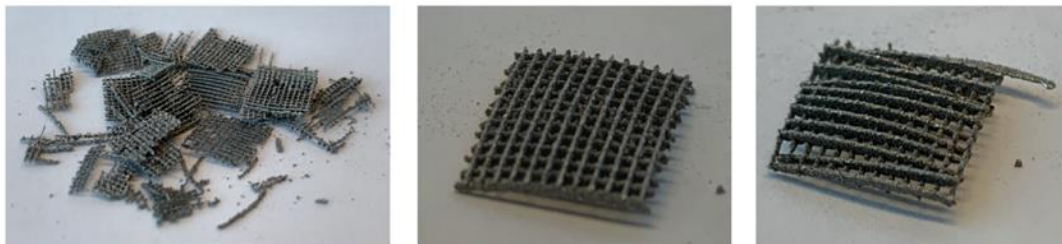


Figure 4.12: H800\_0\_90

During the printing of the samples F and G, the first layers of the lattice fully detached from the building platform which caused some printing problems so that the two samples mixed each other and so it is difficult to distinguish distinct fragments coming from samples **F** and **G**.

During the analysis we take as example the two best pieces within the parts as shown in the Figure 4.12 (center and right figures).

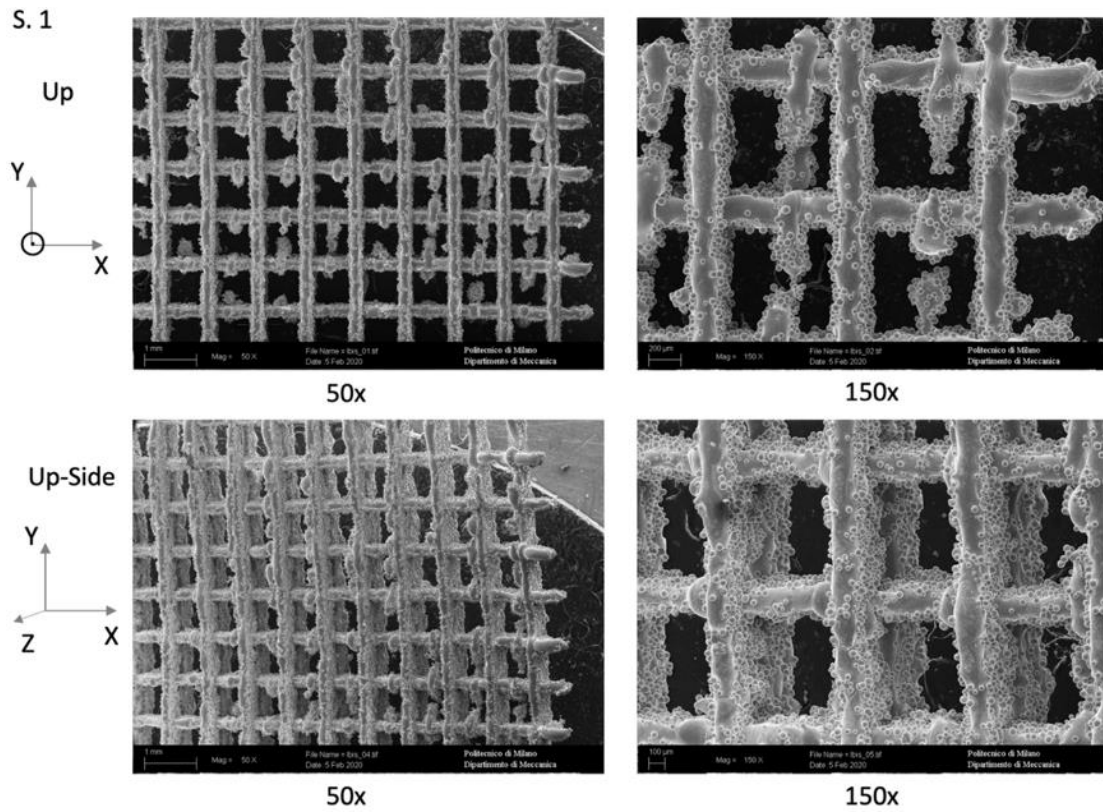


Figure 4.13: SEM analysis of H800\_o\_90

As we can see in the Figure 4.13, in the picture Up-Side 150x, the overlapped beams are well visible and there is also a small porosity due to method applied to print these samples.

#### 4.4 Conclusion of the 1st printing

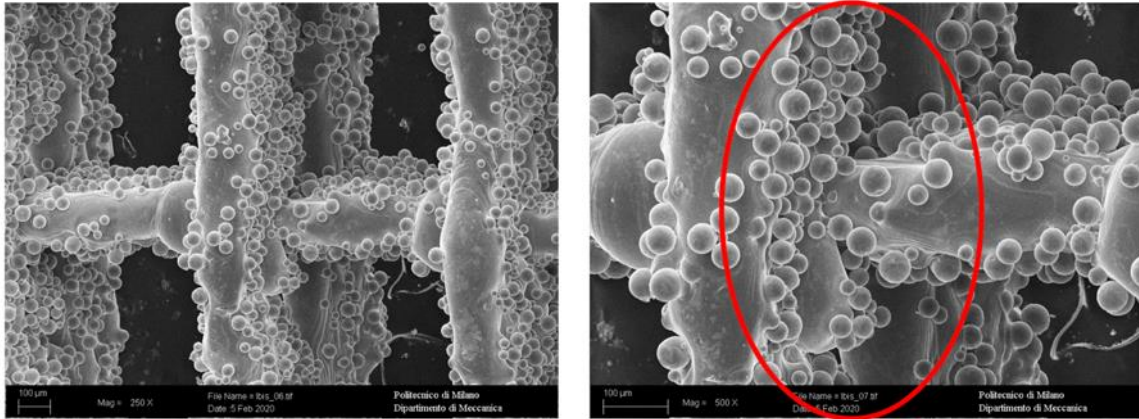


Figure 4.14: H800\_0\_90 beams

We can summarize by saying that the first 5 samples (H400, H600, H800, H1000 and H1200) have a very well defined and repeatable geometry in the XY plane (and so a good porosity in Z direction) but we still have to create the porosity in the XZ plane and in the YZ plane because each weld bead collapsed onto the previous one so there is no side porosity left.

The approach used in the samples **F** and **G** (Figure 4.14) is the beam overlap method in which  $n_F = 10$  and  $n_G = 5$  so, even if we were theoretically expecting a porosity, in the side, between the series of tracks (the beams) we can see some holes so in the end this is the best way to follow: we had printing problems so we can't analyze a good sample but we have reason to suppose that if we improve this method we can reach a good level of porosity and so we will try to reduce the hatch distance to  $H_d = 400 \mu m$  and  $H_d = 600 \mu m$ . In this way the distance between two parallel tracks is reduced and there is less suspended weld bead in the following layer so with less cantilever weld bead we suppose to have less collapse.

## 5 Second Printing

For the Second printing we set 3 cubes as shown in the Figure 5.1:

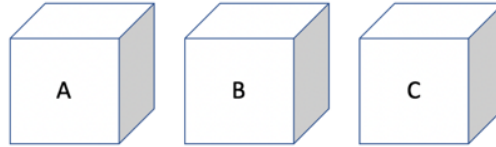


Figure 5.1: Second printing setting

Cube Position	Sample Name
<b>A</b>	H800_L120_ET110_PD40
<b>B</b>	H800_L120_ET140
<b>C</b>	H800_L120_PD30

Table 5.1: 2<sup>nd</sup> Printing

While in the first printing  $Z = 60 \mu m = const$ , in the second printing we increase the value of  $Z$  up to  $120 \mu m$  and so we increase the value of the melt pool depth.

In this printing we modify the Laser Parameters so that the laser is more focused on the same spot: in the sample **A** the exposure time is increased from  $70 \mu s$  to  $100 \mu s$  and the point distance is decreased from  $60 \mu m$  to  $40 \mu m$ , in the sample **B** the time of exposure is increased from  $70 \mu s$  to  $140 \mu s$  so that and in the sample **C** the point distance is decreased from  $60 \mu m$  to  $30 \mu m$  so that  $t_{eB} = 2 t_{e_{std}}$  and in the sample **C** the point distance is decreased from  $60 \mu m$  to  $30 \mu m$  so that  $P_{dC} = \frac{1}{2} P_{d_{std}}$ .

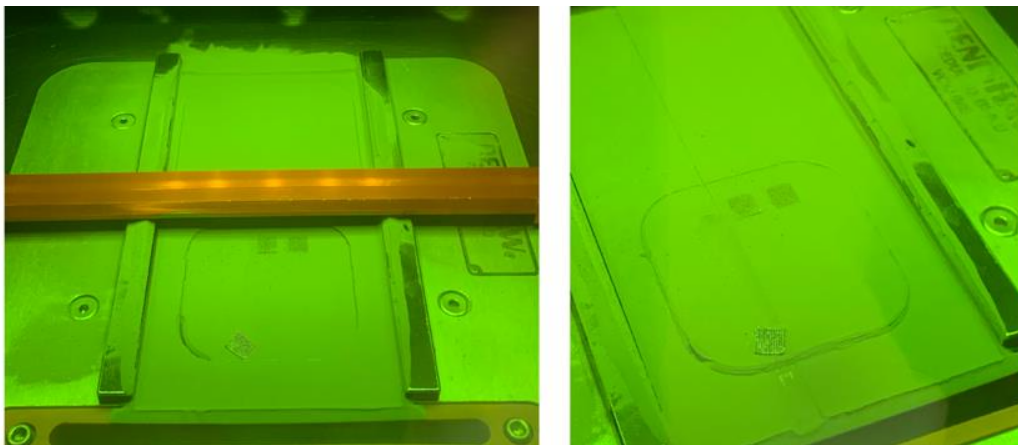


Figure 5.2: 2<sup>nd</sup> Printing

As shown in the in the Figure 5.2 during the printing we had some detachment problems in the samples A and so we had to stop the printing of this sample.

## 5.1 H800\_L120\_ET110\_PD40

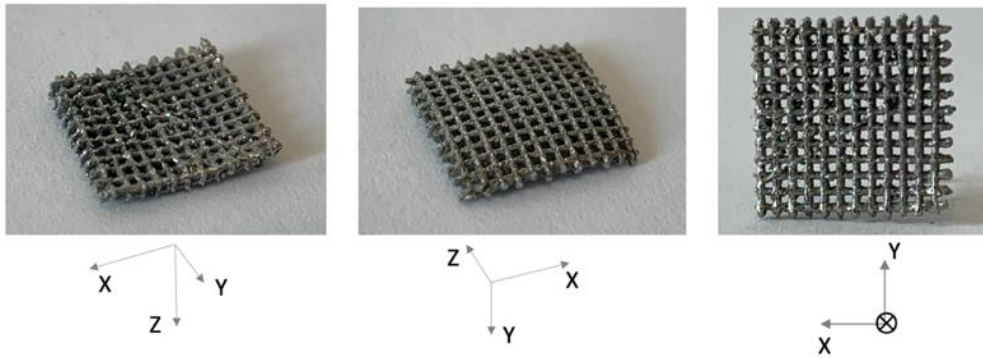


Figure 5.3: H800\_L120\_ET110\_PD40

During the printing of the sample A, the first layers of the lattice fully detached from the building platform which caused some printing problems so that we had to stop the printing as shown in the Figure 5.3.

However we analyzed the sample which can allow us to draw some useful conclusions.

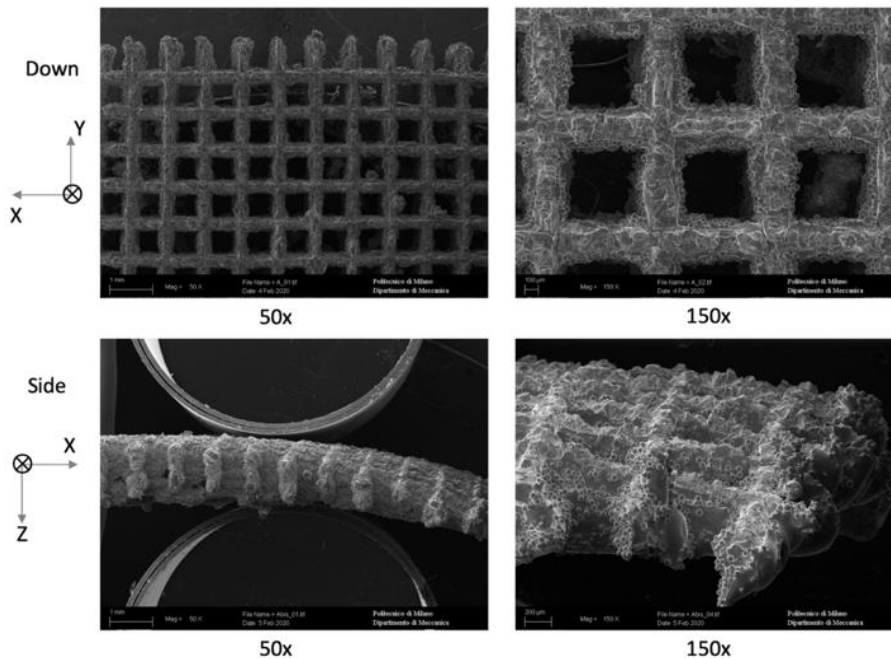


Figure 5.4: SEM analysis of H800\_L120\_ET110\_PD40

As we can see in the Figure 5.4 taken by SEM, the first layer is full of fractures because it detached from the building plate but we have created a good unidirectional porosity, while in the side we have no porosity (even if in this sample there is a small side area, we can see that it is uniform) and so we have to change either the process parameters or the printing technique.

## 5.2 H800\_L120\_ET140 and H800\_L120\_PD30

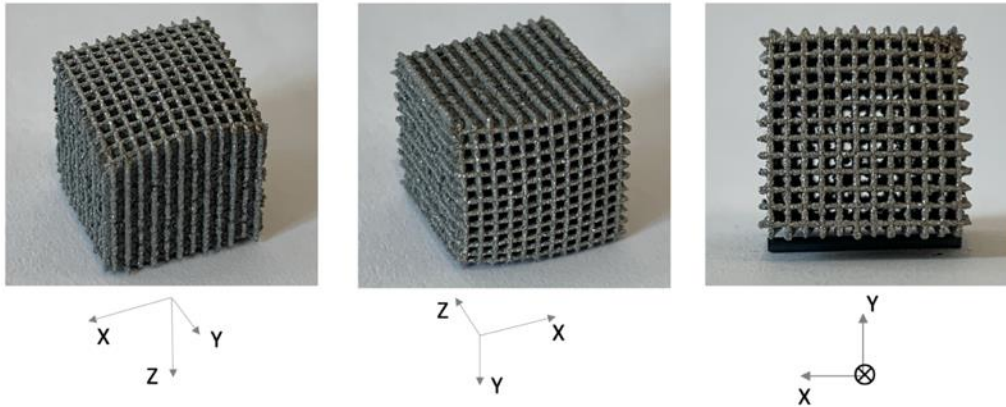


Figure 5.5: H800\_L120\_ET140

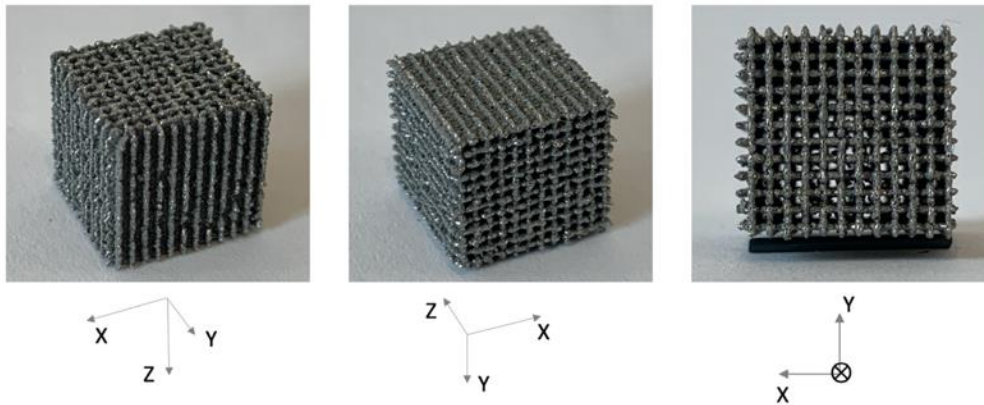


Figure 5.6: H800\_L120\_PD30

The Figure 5.5 and Figure 5.6 show respectively the sample **B** (H800\_L120\_ET140) and the sample **C** (H800\_L120\_PD30): both the samples have a similar structure but the sample C has a cubic shape so there was no deformation of the first layers because of detachment problems due to shrinkage thermal stresses.

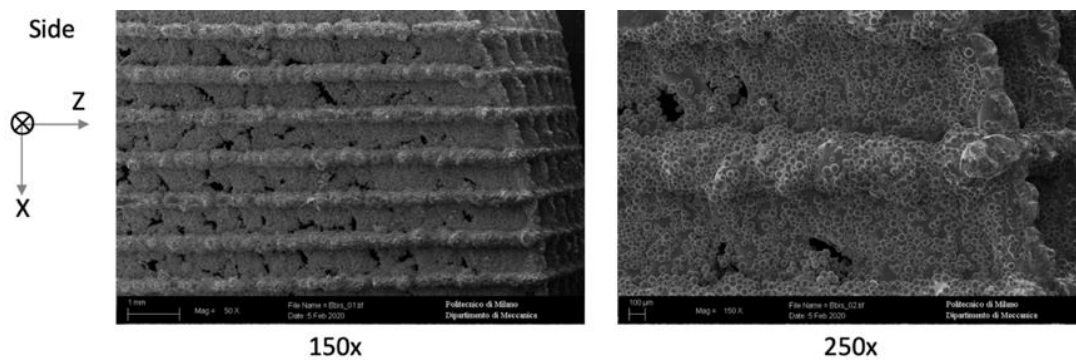


Figure 5.7: SEM analysis of H800\_L120\_ET140

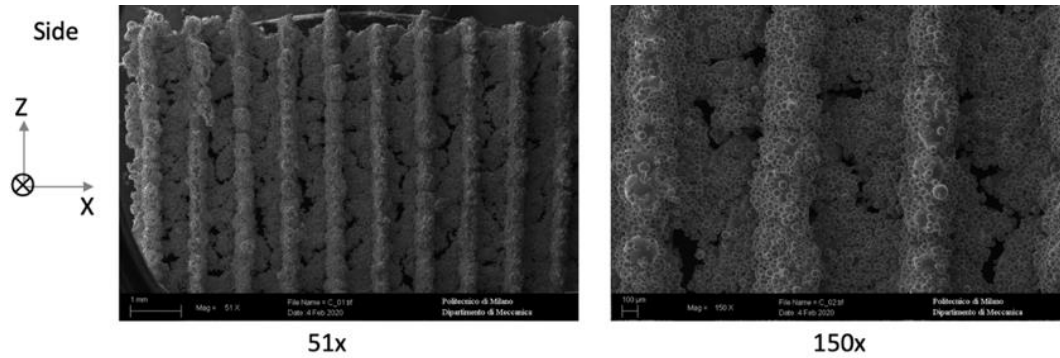


Figure 5.8: SEM analysis of H800\_L120\_PD30

Through Z direction the porosity is comparable to that of the samples in the first printing (4.1 and 4.2) and so it is well visible and geometrically defined.

The Figure 5.6 and Figure 5.8 taken by SEM show the side of the two samples where it is possible to notice a random porosity without a defined shape or an uniform repetition and so we can't say we improved the side porosity level because we have to change the printing technique in order to achieve a uniform pattern of porous in the side.

### 5.3 Conclusion of the 2<sup>nd</sup> printing

We could state that the detachment problems do not depend neither on the printing settings or on the printing parameters so we can't control this phenomenon without create a support. Anyway the method used during the second printing did not give us satisfying results and so we have no controlled porosity in the sides so that we have to change the method to print.

The next methods to analyze and to further explore are the beam overlap method and the rotation for angles less than 90° in order to find other solutions.

## 6 Third Printing

For the third printing we set 7 cubes as shown in the Figure 6.1:

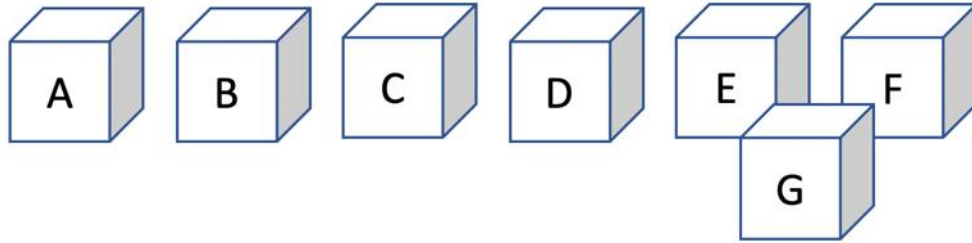


Figure 6.1: 3<sup>rd</sup> printing setting

Cube Position	Sample Name
<b>A</b>	H800_D100
<b>B</b>	H600_o_90_n10
<b>C</b>	H600_o_90_n5
<b>D</b>	H600_30
<b>E</b>	H600_45
<b>F</b>	H600_67
<b>G</b>	H1200_67

Table 6.1: 3<sup>rd</sup> printing

The samples **A**, **B** and **C** are made with the “Beam overlap technique” by overlapping respectively 15, 15 and 30 beams made respectively of 10, 10 and 5 tracks oriented at  $0^\circ$  and  $90^\circ$  (so that  $n_A = 10$ ,  $n_B = 10$  and  $n_C = 5$ ): these samples are made with the same method of the samples **F** and **G** of the first printing but in this case we reduced the hatch distance.

In the samples **D**, **E**, **F**, and **G** we try to create the porosity by rotating each layer of a specific angle  $\alpha$ : the value of the angle has to be between  $0^\circ$  and  $90^\circ$  taking care that if  $\alpha$  is too low we can risk to have a wall which grows with a DNA geometry without having porosity on the side and there could be also the risk of the collapse of the thin walls.

In these samples  $n = 1$  and we set the hatch distance  $H_d = 600 \mu m$ .





Figure 6.2: 3<sup>rd</sup> printing

As shown in the Figure 6.2, during the printing we had some detachment problems so that the samples **E** (H600\_45) detached and so we had to stop the printing of this sample.

Regarding the other samples, they perfectly stuck as shown in the Figure 6.3 so that to remove them we had to use a palette knife and so we damaged the first layers which remained welded to the printing plate (it is not a problem when we analyze the samples).

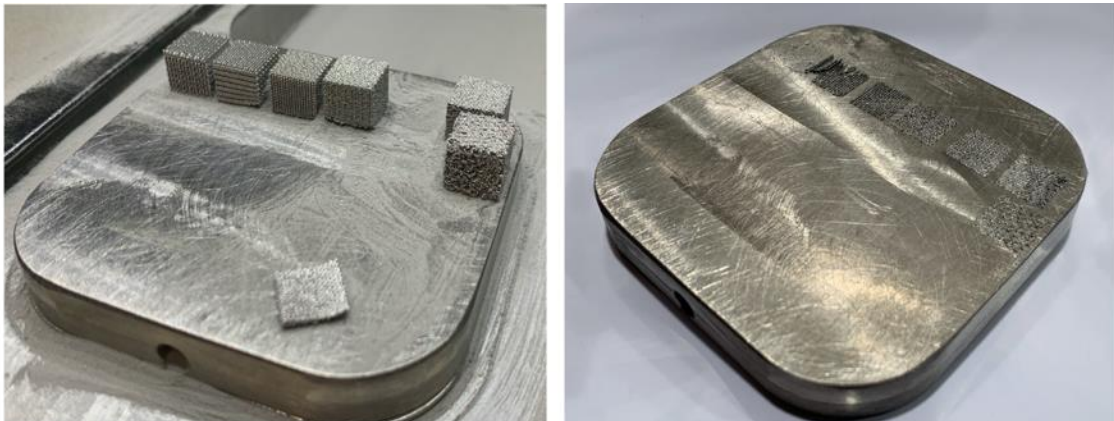


Figure 6.3: Printing plate after the 3<sup>rd</sup> print

## 6.1 H800\_D100

To design the sample **A**, through Magics Materialise, we created a cube made by two intersecting H800 cubes displaced by 100  $\mu\text{m}$  in the X axis and 100 $\mu\text{m}$  in the Y axis as shown in the Figure 6.4 and in the Figure 6.5. In this way we have the superposition between the weld beads and so there is more contact surface between the consecutive layers in order to have less detachment problems:

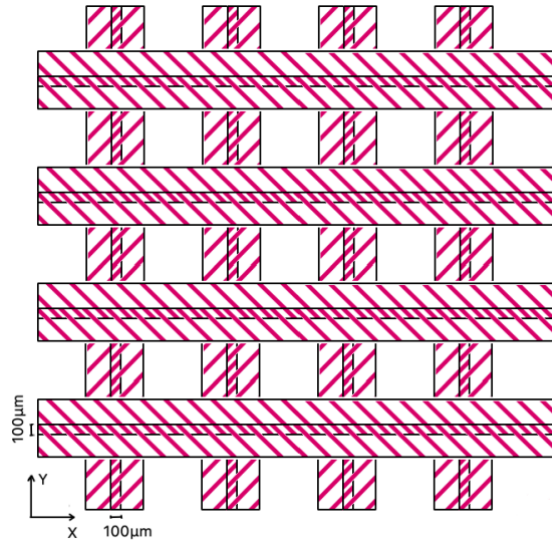


Figure 6.4: H800\_D100 printing settings

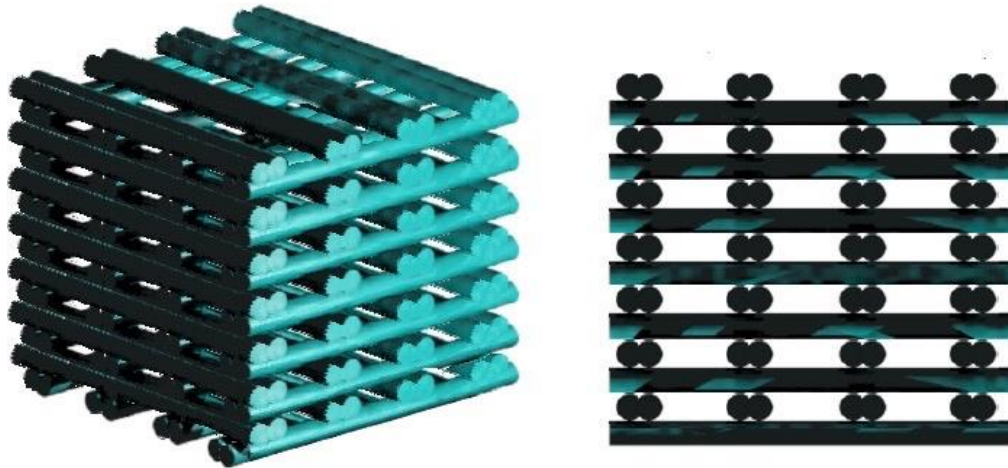


Figure 6.5: H800\_D100 printing settings

This sample was printed by using the beam overlap method but we modified it in order to have a wider weld bead.

The cube is created by alternating at 0° and 90°, fifteen group of layers (about 600  $\mu\text{m}$  each) so that  $n = 10$ .

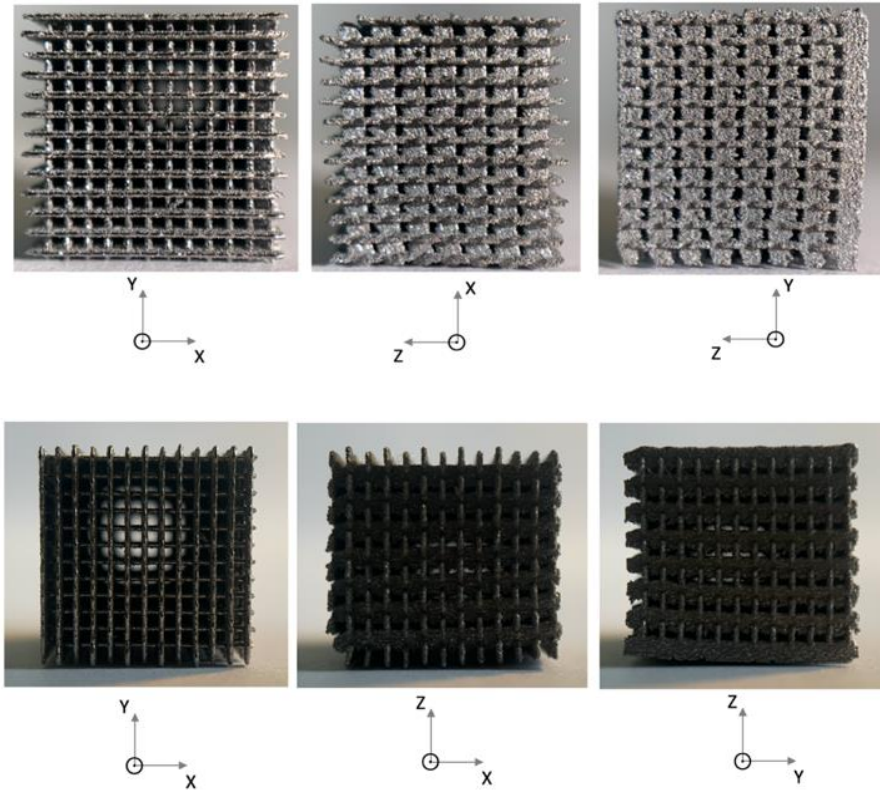


Figure 6.6: H800\_D100

As we can see in the Figure 6.6, it is possible to see-through in all the directions and so for the first time we have a well defined porosity also in all the sides, with a definite geometrical shape. In addition the sample has the cubic shape so there were no detachment problems.

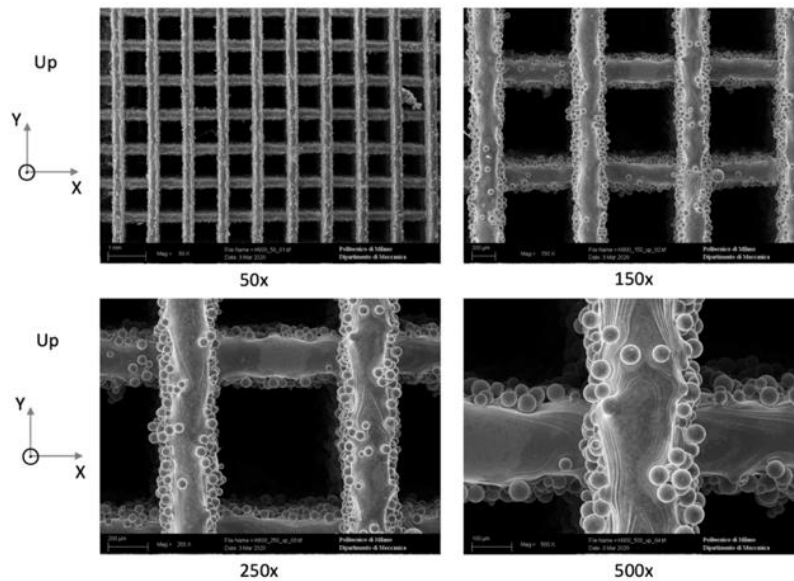


Figure 6.7: SEM analysis of H800\_D100 (up view)

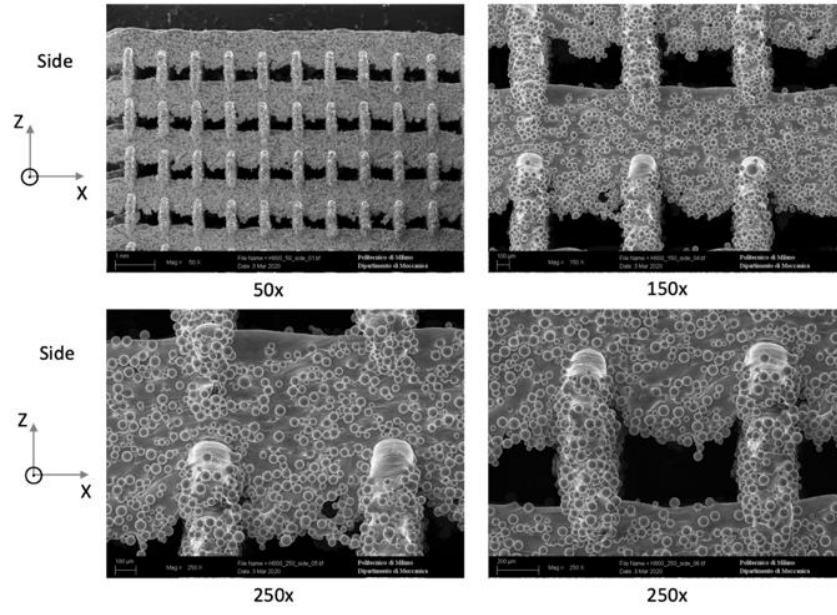


Figure 6.8: SEM analysis of H800\_D100 (side view)

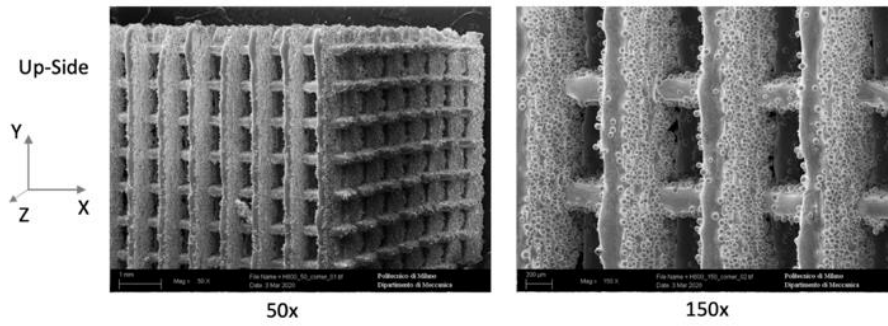


Figure 6.9: SEM analysis of H800\_D100 (up-side view)

## 6.2 H600\_o\_90\_n10 and H600\_o\_90\_n5

The samples **B** (H600\_o\_90\_n10) and **C** (H600\_o\_90\_n5) are made by following the idea of the samples **F** and **G** of the first printing (which had detachment problems so it was not possible to analyze them) but with less cantilever weld bead so that the problem of collapse of the layers onto the previous should be improved. The cubes are designed as follow:

- The sample **B** is made of the alternation at  $0^\circ$  and  $90^\circ$  of fifteen group of layers (about  $600\ \mu\text{m}$  each) so that  $n = 10$  ;
- The sample **C** is made of the alternation at  $0^\circ$  and  $90^\circ$  of thirty group of layers (about  $300\ \mu\text{m}$  each) so that  $n = 5$  ;

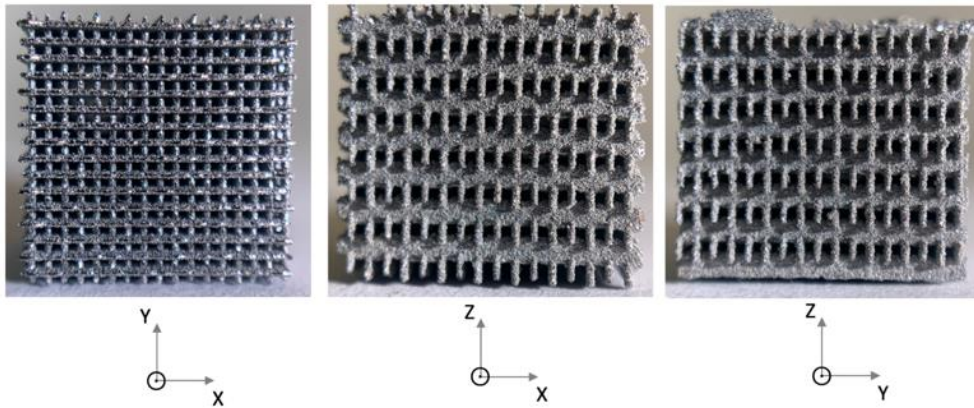


Figure 6.10: H600\_o\_90\_n10

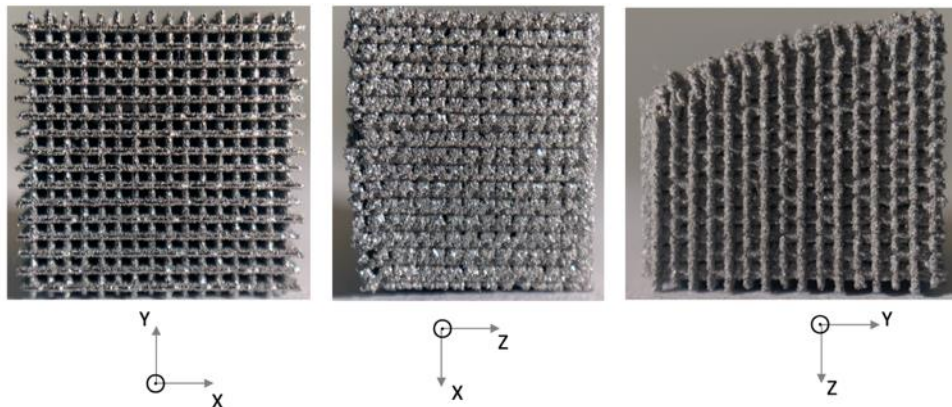


Figure 6.11: H600\_o\_90\_n5

The Figure 6.10 and Figure 6.11 show the two samples: while the sample **B** did not have problems and shows a cubic shape, the sample **C** shows a defect in the first layer due to the detachment problems. However it is possible to notice a good level of porosity also in the side and additionally it is possible to see-through in all the directions.

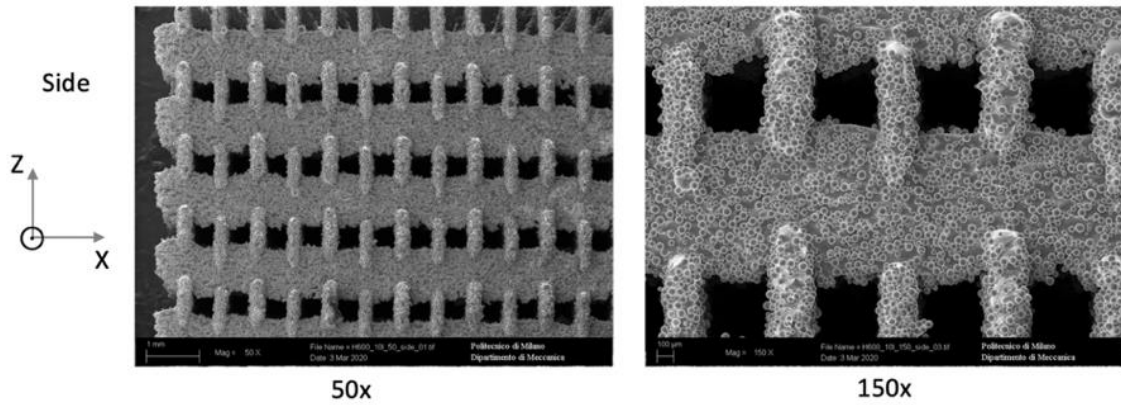


Figure 6.12: SEM analysis of H600\_o\_90\_n10 (side view)

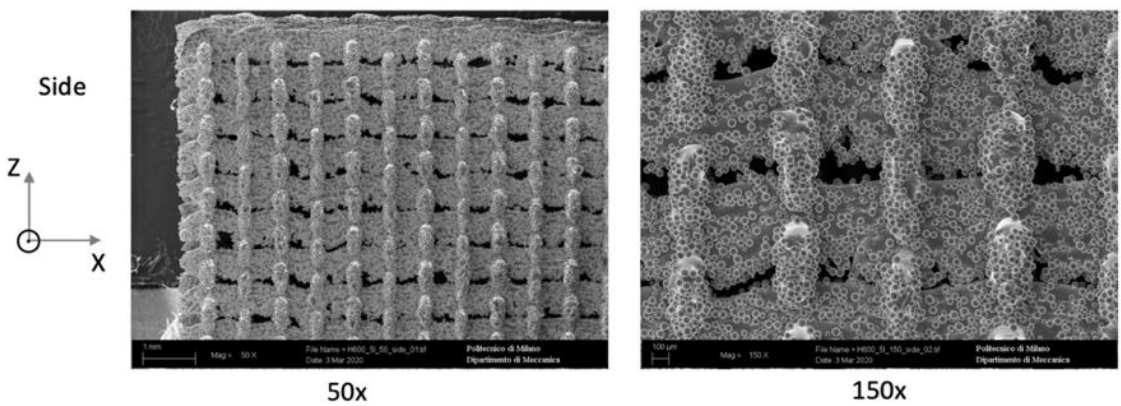


Figure 6.13: SEM analysis of H600\_o\_90\_n5 (side view)

As we were expecting, even if the hatch distance of both the samples is the same, the sample **B** presents bigger and more defined shape of the porosities in the sides because the beam (made of weld beads) is more solid and so there is less collapse due to the gravity. The sample **C** shows smaller and less defined holes that in some cases are almost closed due to the collapse of the weld bead.

### 6.3 H600\_30, H600\_45 and H600\_67

The following pictures are referred to the samples **D** (H600\_30), **E** (H600\_45) and **F** (H600\_67), made by using the default parameters but setting the hatch distance  $H_d = 600 \mu\text{m}$  and the rotation angle respectively  $\alpha_D = 30^\circ$  (for the sample **D**),  $\alpha_E = 45^\circ$  (for the sample **E**),  $\alpha_F = 67^\circ$  (for the sample **F**), so that each layer is rotated of  $\alpha$  compared to the previous and so  $n = 1$ .

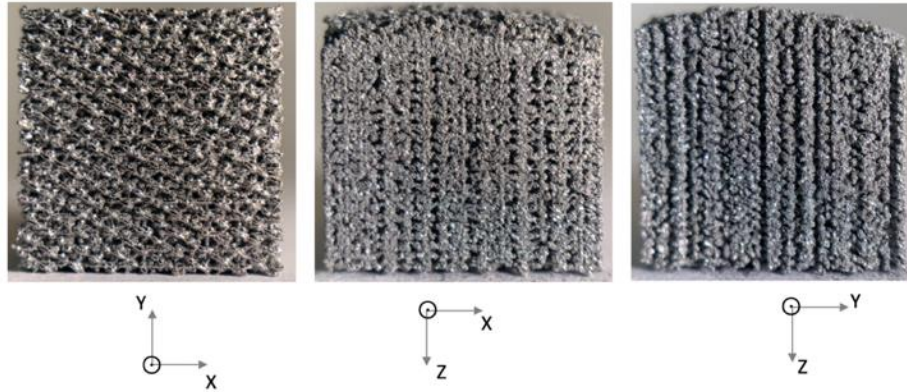


Figure 6.14: H600\_30

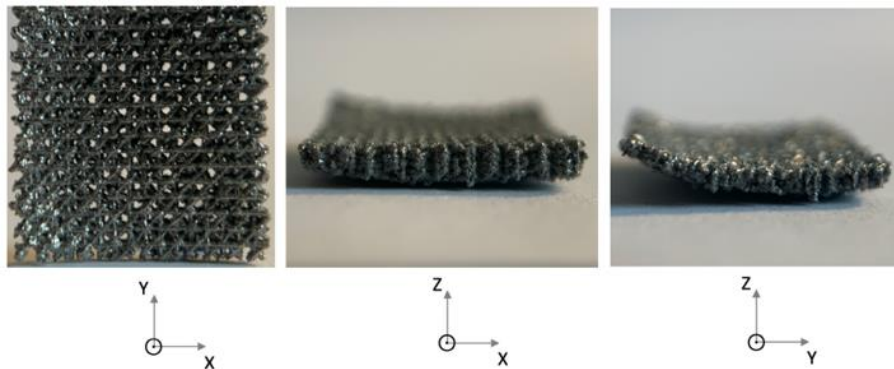


Figure 6.15: H600\_45

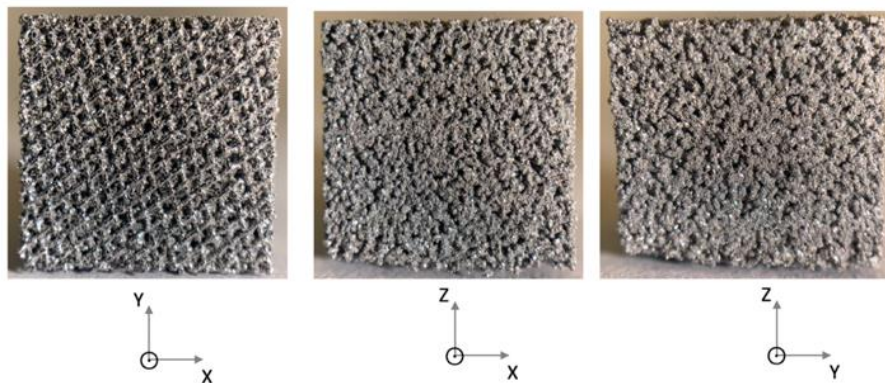


Figure 6.16: H600\_67

As we can see in the Figure 6.15 to print this sample **E** there were detachment problems so that we had to stop the print after few layers so this sample will be printed again in order to be studied. Even if, as expected, it is not possible to look-through the sample, the porosity seems to be visible to the eye in all the directions.

For these sample we thought it was useless to make the analysis with the 500x magnification because it was difficult to recognize the structure and the geometry.

Nevertheless, analyzing by SEM the three samples (even if we will print again the sample E, it is possible to draw some conclusions about it), it is possible to recognize a good level of porosity in all the directions.

The weld bead and their directions are well identifiable and even if there was a small amount of collapse portion of the tracks, the sides show a good porosity pattern, improved by the new used technique.

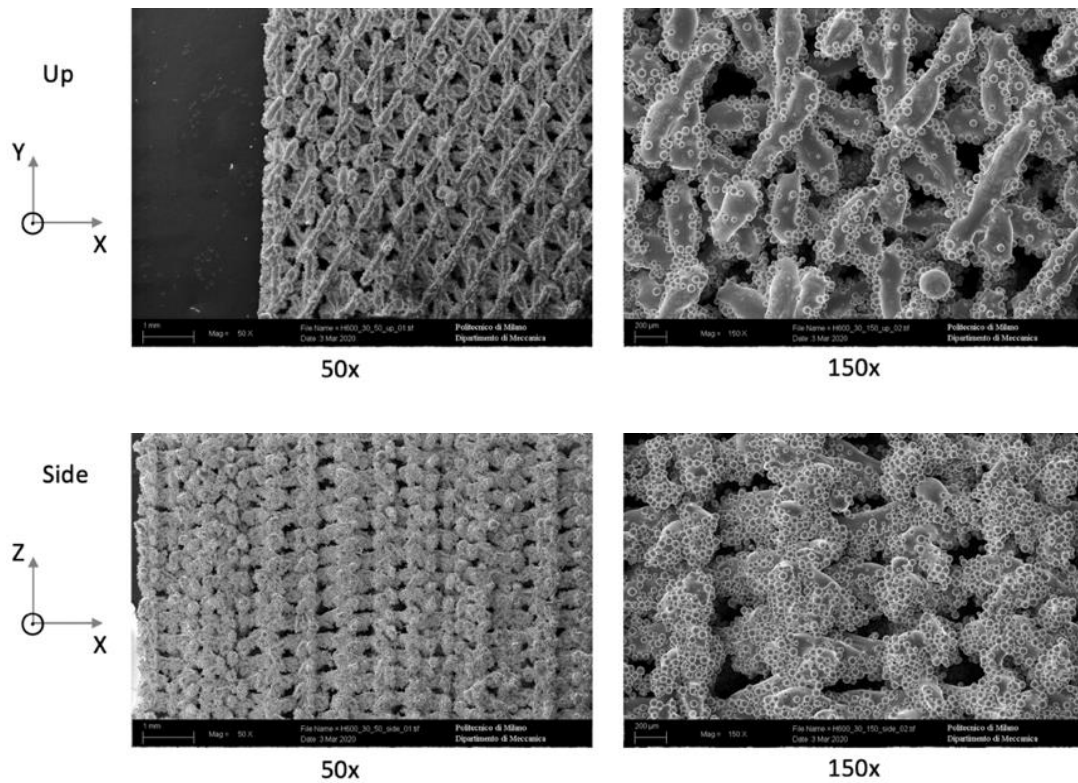


Figure 6.17: SEM analysis of H600\_30 (up and side views)



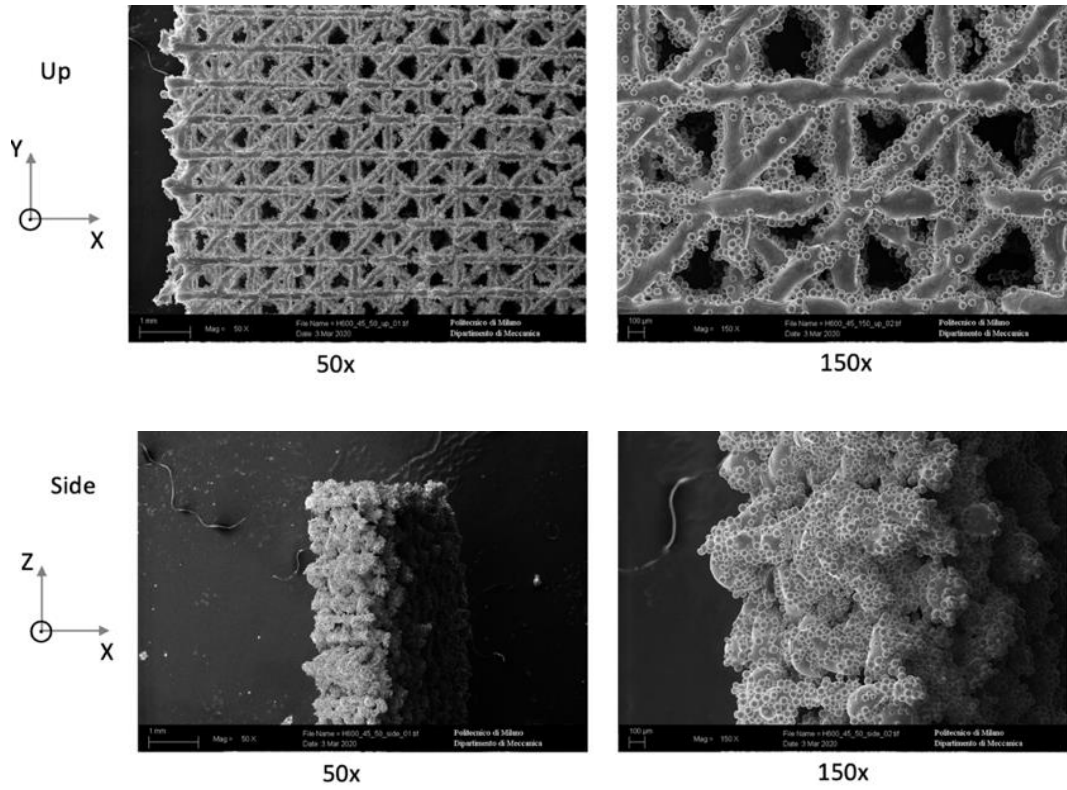


Figure 6.18: SEM analysis of H600\_45 (up and side views)

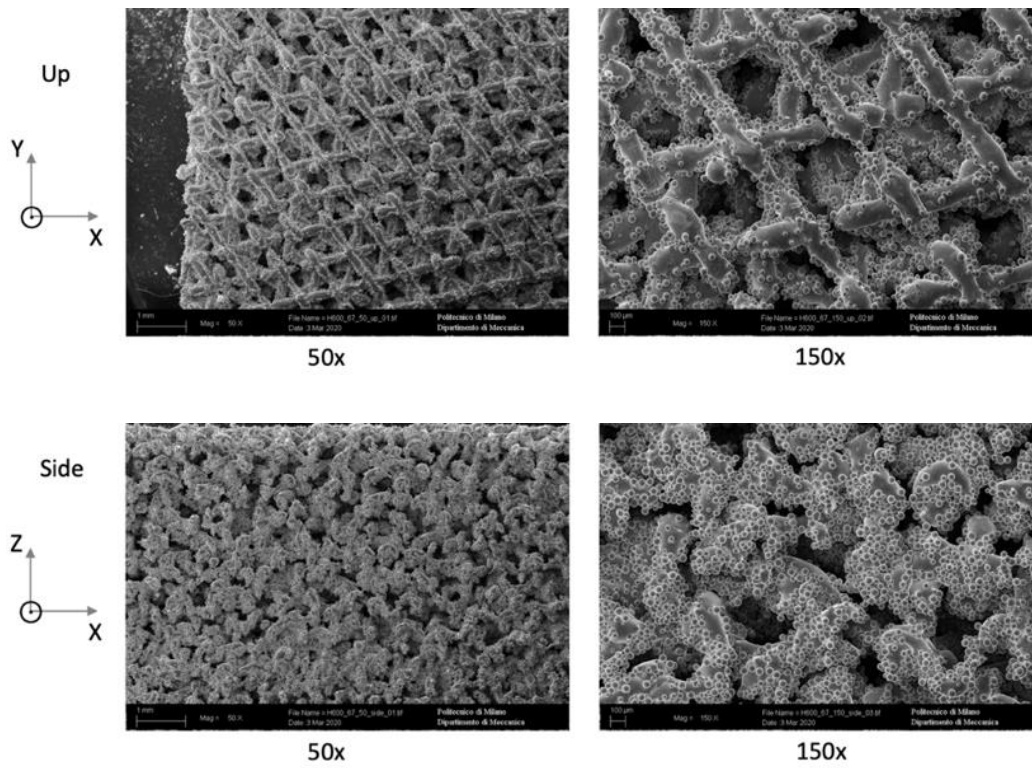


Figure 6.19: SEM analysis of H600\_67 (up and side views)

### 6.4 H1200\_67

The sample **G** (H1200\_67) is made by using the default parameters and setting the hatch distance  $H_d = 1200 \mu\text{m}$  and the rotation angle  $\alpha = 67^\circ$  so that each layer is rotated of  $67^\circ$  compared to the previous and so  $n = 1$ .

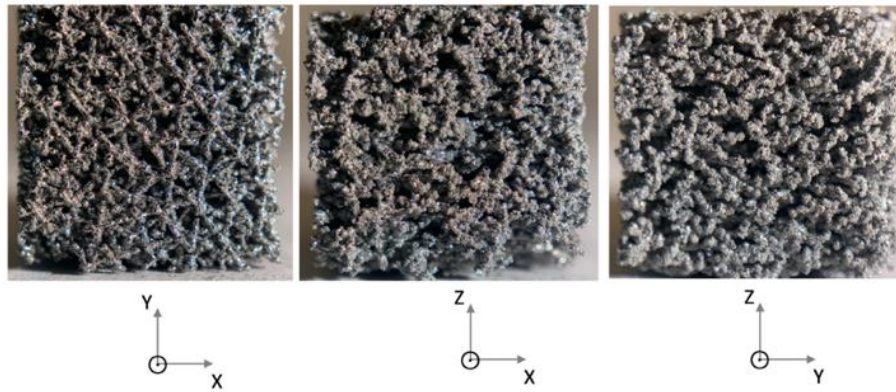


Figure 6.20: H1200\_67

As for the latter analyzed samples, this seems to have a good porosity but with an inhomogeneous shape in all the directions. The sample has not the cubic shape because due to its brittleness it was damaged during the detachment from the printing plate.

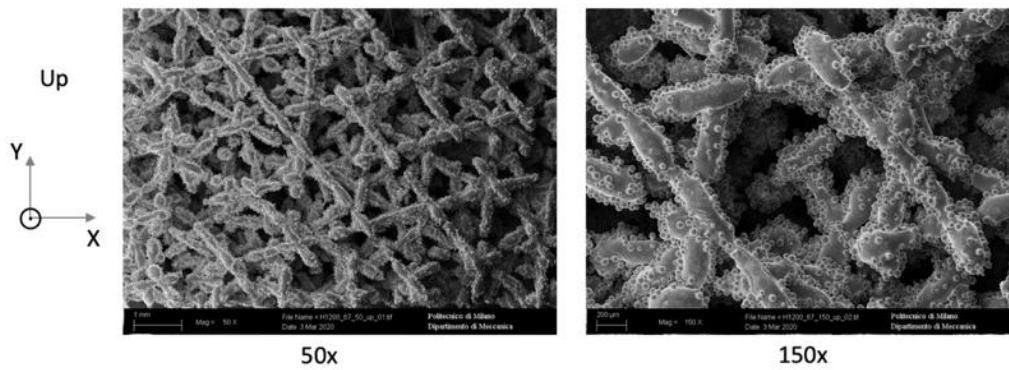


Figure 6.21: SEM analysis of H1200\_67 (up view)

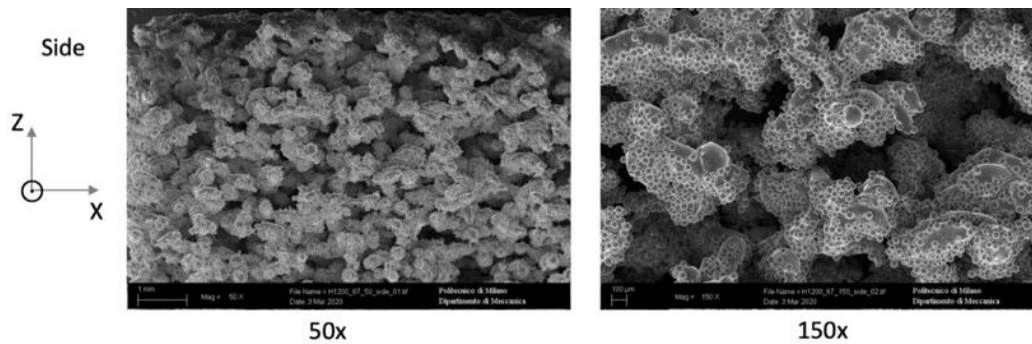


Figure 6.22: SEM analysis of H1200\_67 (side view)

## 6.5 Conclusions

In the samples **A**, **B** and **C** we have a good level of porosity and a well defined geometry in all the directions so that it is possible to see-through.

The samples have a regular, rectangular and interconnected pore distribution. The side and top images show that the distribution of pores is directionally dependent because the wall profiles create thick horizontal bars in the side view but not top view. The pore diameters increase with  $d_{hs}$  as predicted by the theory and all specimens measured exhibit pore diameters between 300  $\mu\text{m}$  and 500  $\mu\text{m}$ .

A potential negative effect of the beam overlap structures is that the pore distribution is directionally dependent. In the side view the walls are seen in profile, which decreases the line of sight porosity compared to the highly open top view.

After the studies at the SEM we noticed that the weld bead has the same width for all of these samples while as shown in the Figure 6.4 and Figure 6.5, we were expecting the track to be wider in the sample **A** due to the displacing of 100  $\mu\text{m}$  in X and Y directions. To sum up we can state that we have achieved a good result in the sample **A**, **B** and **C** but it is a bit tricky to create this kind of porosity because we have to manually displace the tracks, alternating them at  $0^\circ$  and  $90^\circ$  to obtain the beam overlap structure and so for more complicated structures and for practical use it can be a bit difficult and it requires a lot of time.

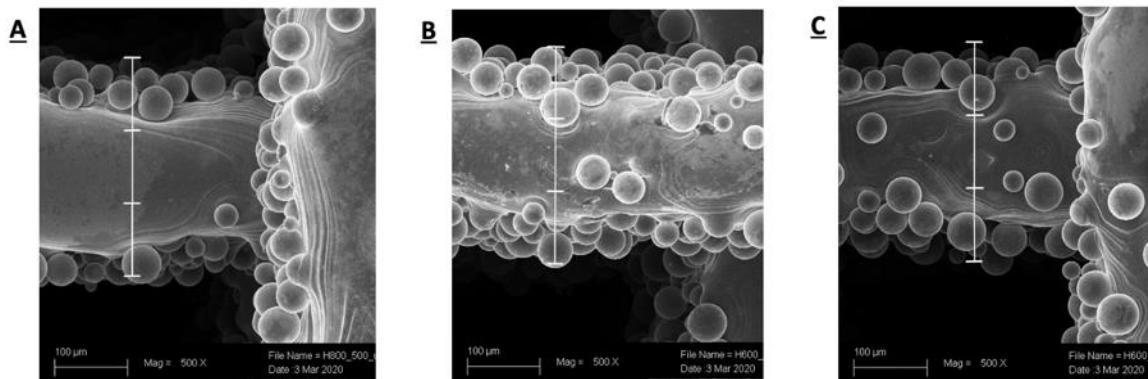


Figure 6.23: Comparison of the weld bead width of the samples **A**, **B** and **C**

In the samples **D** and **F** we have a good level of porosity in all the directions that can seem practically random but it has to be checked along a section plane, through the optical microscopy and with the SEM.

In the sample **E** we can't make accurate conclusions because we print only few layers and then we stop the printing so it should be suggested to make this printing again in order to study this sample.

The sample **G** is too weak and it crumbles just by applying some pressure or under the effect of an external force because of the low contact surface between the following planes and so it can be neglected in the following studies to understand the macro and the microstructure.

## 7 Fourth Printing

The fourth printing is made to print both the sample **E** of the third printing (H600\_45) with a hatch distance of  $600\mu\text{m}$  and rotation angle  $a = 45^\circ$  that during the printing had detachment problems and the sample **D** of the third printing (H600\_30) with a hatch distance of  $600\mu\text{m}$  and rotation angle  $a = 30^\circ$ .

The samples are printed as shown in the Figure 7.2 and schematized in the Figure 7.2:

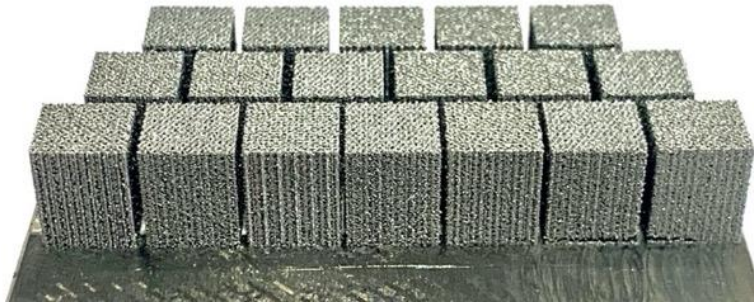


Figure 7.1: 4<sup>th</sup> printing

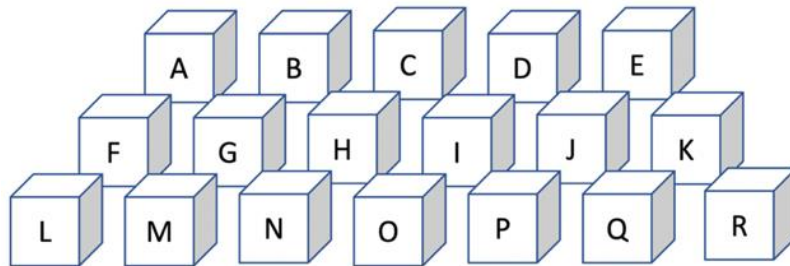


Figure 7.2: 4<sup>th</sup> printing setting

Cube Position	Sample Name
<b>A, B, E, H, K, M, O, Q</b>	H600_30
<b>C, D, F, G, I, J, L, N, P, R</b>	H600_45

Table 7.1: 4<sup>th</sup> printing

In the fourth printing we printed 18 samples and in the specific:

- 8 x H600\_30 of which six of them for the compression test in the three directions and two more to stay in safety and to have a margin of error if some samples had had problems;
- 10 x H600\_45 of which six of them for the compression test in the three directions, one of them for the metallographic analysis and three more to stay in safety and to have a margin of error if some samples had had problems.

## 8 Metallographic analysis

The next analysis is made in order to understand if the porosity is present also inside the samples. The samples to be analyzed are:

- from the 3<sup>rd</sup> printing the samples **A** (H800\_D100), **C** (H600\_o\_90\_n5), **D** (H600\_30) and **F** (D600\_67) as shown in the Figure 8.1;
- from the 4<sup>th</sup> printing the sample **R** (H600\_45);

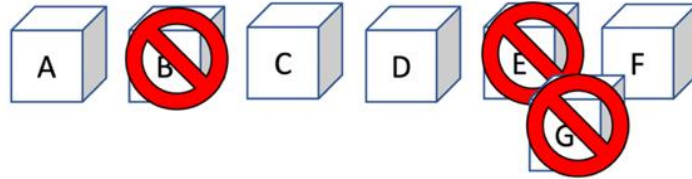


Figure 8.1: Samples chosen for the metallography

The other samples are not studied for the following reasons:

- **B**: H600\_o\_90\_n10 is made of 15 beams made of 10 layers each and so it is kind of a mix between the sample A and the sample C that are already studied separately;
- **E**: H600\_45 was stop after few layers because, as shown in the Figure 8.2, it started to detach and so it was not possible to cut and mount it to be studied;
- **G**: H1200\_67 is too weak and it smashes by applying pressure or an external force so we decided to avoid to study this sample because it is useless.

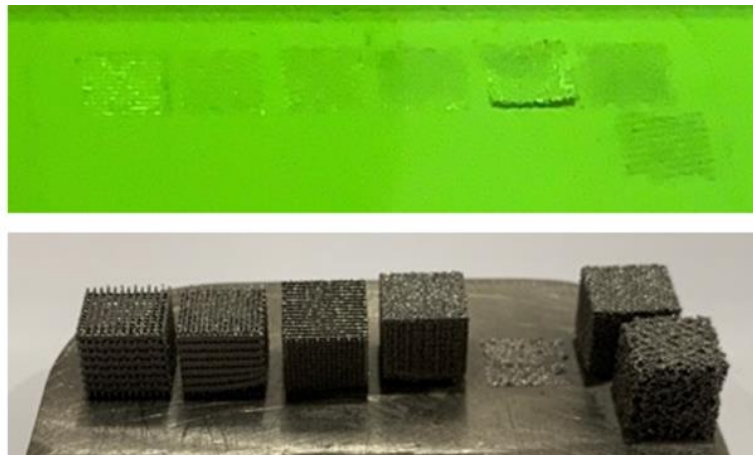


Figure 8.2: 3rd printing process during and after

The studies are made at the beginning to check the macrostructure and then to check the microstructure.

Each sample is cut in three pieces in order to study two different plane sections: the plane XY and the plane ZY or ZX which is the same because of the symmetry of piece. The studied sections are highlighted in the Figure 8.3 in order to understand the inner porosity corresponding with the side and with the top surface of the cube:

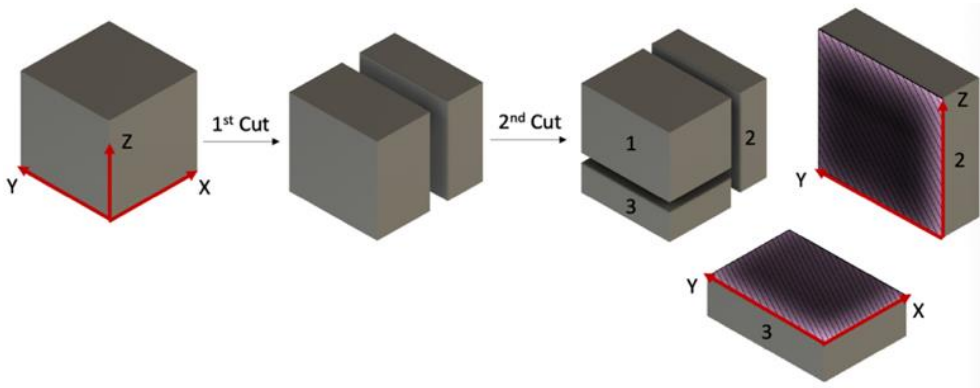


Figure 8.3: scheme of the cutting process

The sections, to be studied, are mounted in a resin for convenience in handling, to protect the edges and in order to fill the pores to facilitate the studies.

To better understand which kind of resin better satisfy our requests of fluidity in order to fill the porosity, we tried both the hot method and the cold method, and then we decided: the hot method is used for the sample **A** and the cold method is used for the sample **D** as shown in the Figure 8.4:

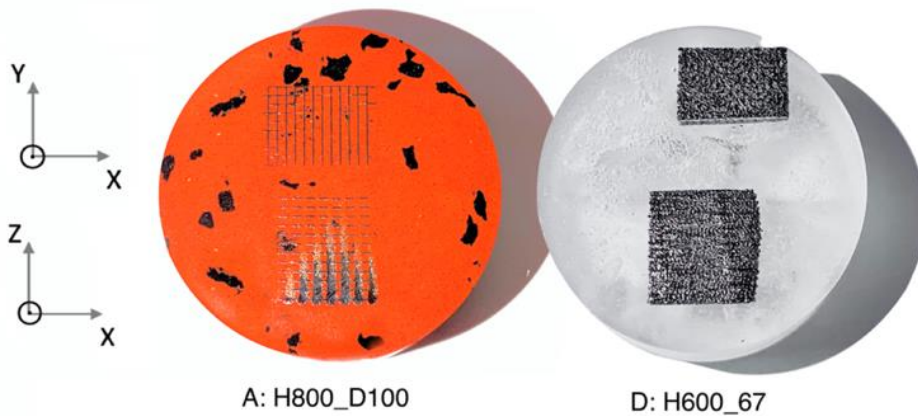


Figure 8.4: Cut of samples A and D

Comparing the two samples we can see that with the cold method:

- the resin was not able to penetrate deeply, maybe either because of the smaller size of the pores of the sample D or because of the absence of pressure that forces the liquid polymer to fill the porosities;

- in the mounted sample there is the presence of bubbles inside, maybe released by the sample during the polymerization process from the pores;
- the metal pieces moved during the process of pouring.

While the hot method is faster, the resin fills the pores, there are no visible bubbles, the metal pieces didn't move and the costs are cheaper so we decided to proceed with this hot method for the other samples.

Within all the mounted samples, we have chosen to deeply study and analyze:

- H600\_o\_90\_n5 (from the third printing in the chapter 6.2) because it has the best properties within the samples made with the beam overlap method;
- H\_600\_30 (from the third printing in the chapter 6.3) and H\_600\_45 (from the fourth printing in the 7) because they have a good porous uniformity with a good level of porous order along the three axis.

Even if other samples showed a good final result in terms of porosity and homogeneity of the hole pattern, a lot of them presented similar structures.

The chosen sample are then mirror polished by using increasingly finer clothes and in the end we used a synthetic-velvet disc imbued with a 1 $\mu$ m diamond paste and oil.

To avoid the sample to oxide we made an extra final step consisting of a polishing of the samples with hydrogen peroxide.

These steps are followed by the etched of the samples with the reagent to stand out the microstructure, and so we proceed to analyze the samples first at the optical microscope to have a magnification of 25x and 100x and then we use the SEM to have a magnification of 500x and 1500x.

## **8.1 H600\_o\_90\_n5**

As we can see in the Figure 8.5 the structure is well visible both in the side and in the up views. There are some voids in the side view but they can be reasonably related to the fact that the section is close to end of the weld bead and so the layers are visible and distinguishable.

In the Figure 8.6 we can see that the microstructure is uniform in the XY plane and in the XZ plane and it is all martensite, so there are no visible weld beads or weld tracks.



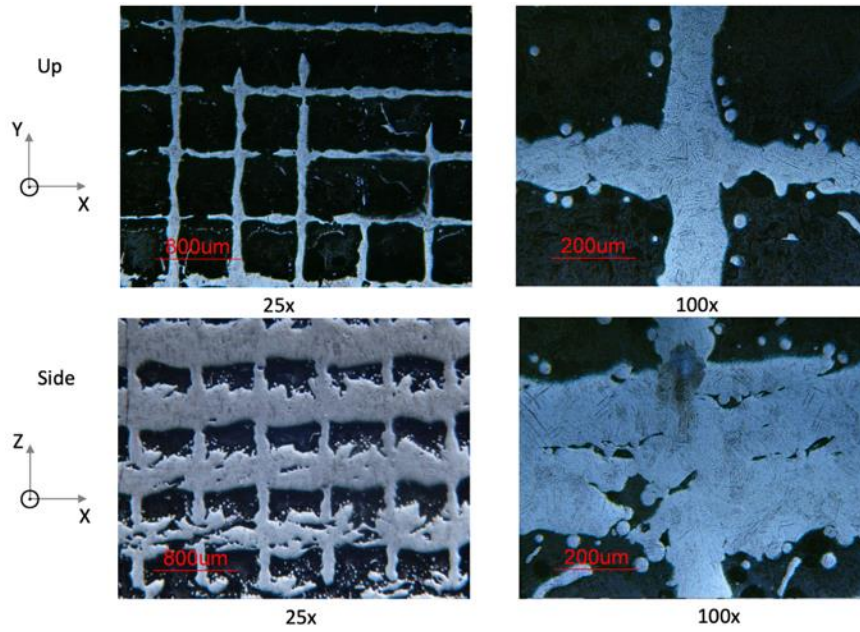


Figure 8.5: Optical Microscope Up and side views of H600\_o\_90\_n5

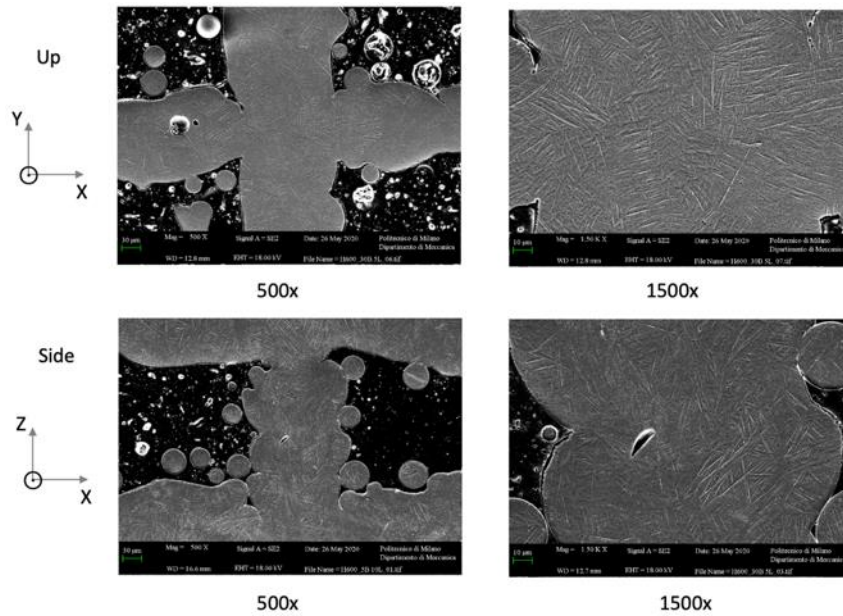


Figure 8.6: SEM Up and side views of H600\_o\_90\_n5

## 8.2 H600\_30

As we can see in the Figure 8.7 the porosities are well distinguishable in the top view while in the side it is present a good level of porosity which seems to have a regular pattern. In the XY plane it is possible to see different layers because, during the cut, the mounting and the polishing, it is reasonably possible that the cut was not exactly parallel to the XY plane and also, there can be some collapse of the layers onto the previous one.

In the Figure 8.8 we can see that the microstructure is uniform in the XY plane and in the XZ plane and it is all martensite, so there are no visible weld beads or weld tracks. We can also notice that a lot of powder particles are present within the porosities: this could be because the sample was not properly cleaned and so some metal powder could have been stuck in the structure.

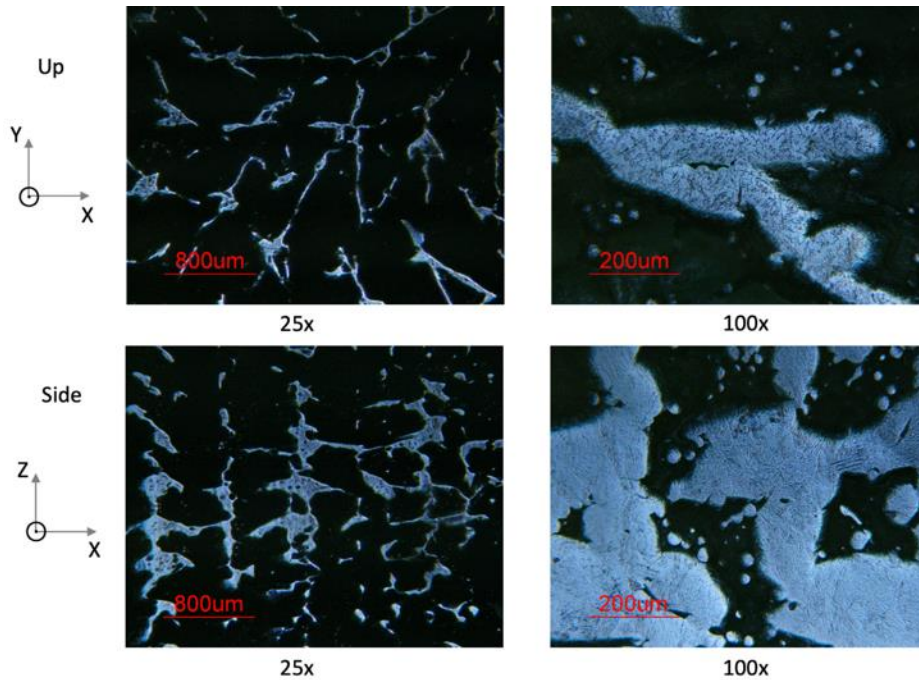


Figure 8.7: Optical Microscope Up view of H600\_30

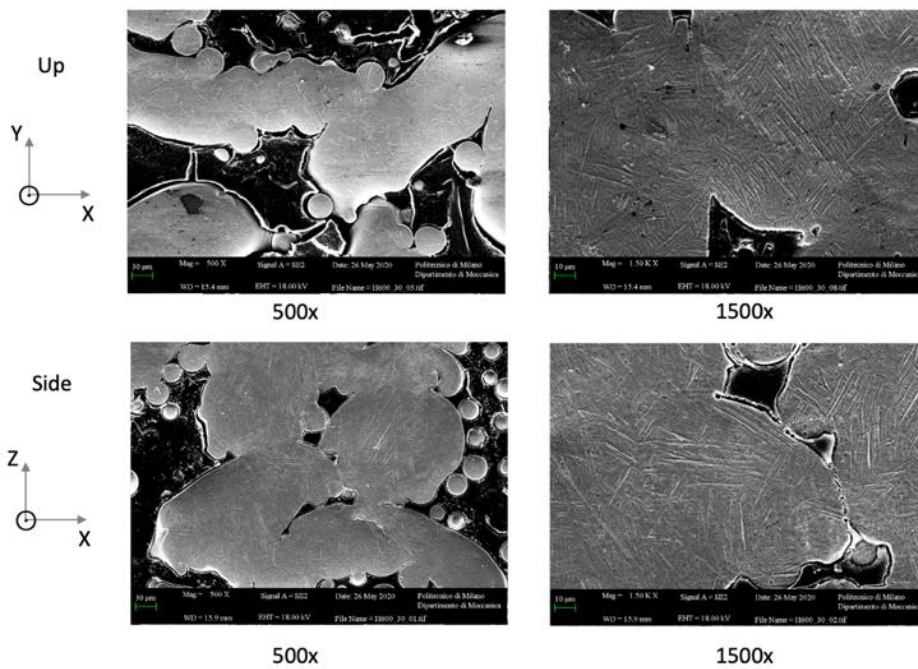


Figure 8.8: SEM Up view of H600\_30

### 8.3 H600\_45

For this sample, the conclusion are very similar to the sample H600\_30 and so, as shown in the Figure 8.9 and in the Figure 8.10, the structure is well visible and the microstructure is uniform and it is all martensite.

For this sample we didn't make the magnification of 1500x in the XY-plane because the attack effect was weaker than in the other direction so the microstructure was not highlighted as we were expecting but we can reasonably expect the same microstructure of the other samples: this can be stated because in all the samples studied, we saw the same microstructure.

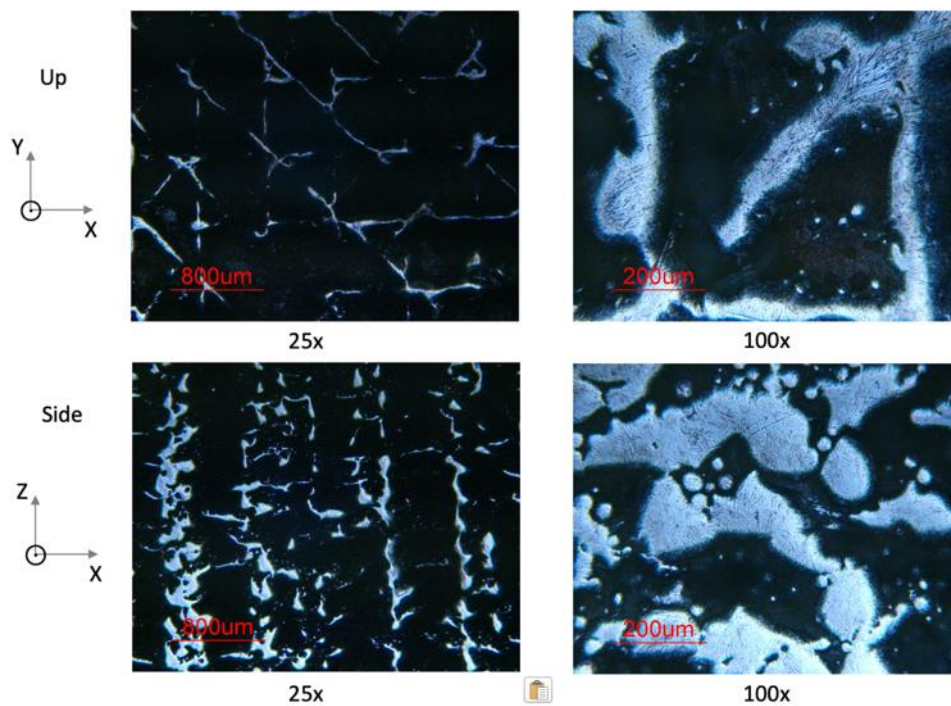


Figure 8.9: Optical Microscope Up view of H600\_45

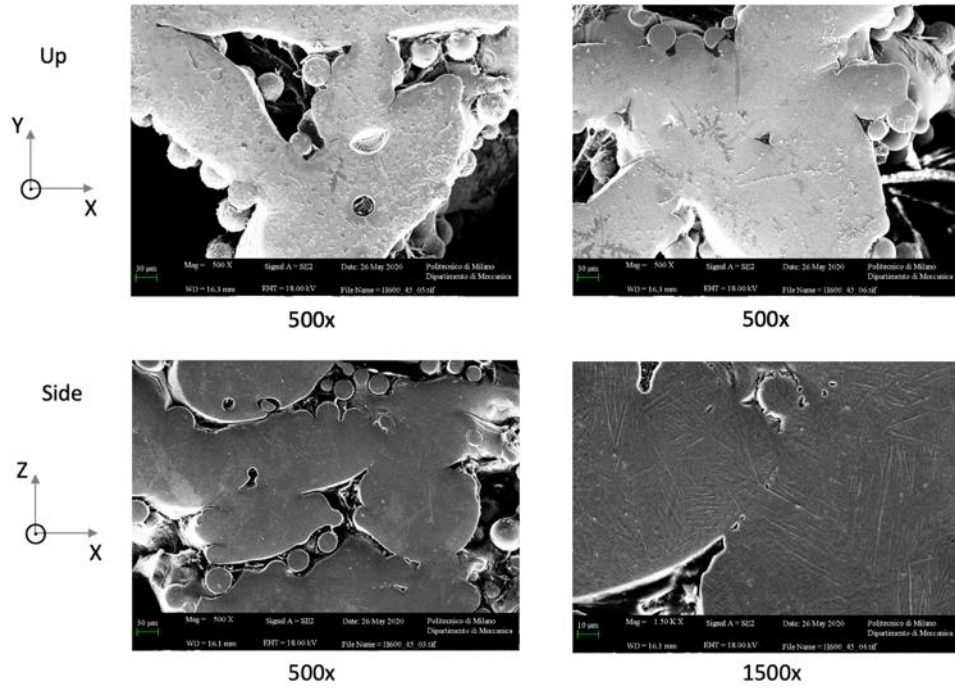


Figure 8.10: SEM Side view of H600\_45

## 9 Compression test

The compression test is made in order to study the material behavior according to a testing mode which is compatible to size and shape of the produced samples.

While uniaxial testing is sufficient for isotropic samples, anisotropic samples require tests along the different main directions.

In the case of plastic deformation, anisotropy plays a significant role because it means that the sample has different reactions depending on direction of the force.

To better study the behavior of the sample to the compressive stress, we repeat each test three times per direction in order to have more data to analyze.

The tests are made in both directions Z and X (or Y, since it is the same) for H600\_30 and H600\_45. We expect stress-strain curves characterized by three stages:

- The first stage with a linear curve because of the elasticity of the material;
- The second stage with a plateau related to a high plastic deformation of the lattice struts;
- The third stage with a densification where the stress increases sharply because of the collapse of struts.

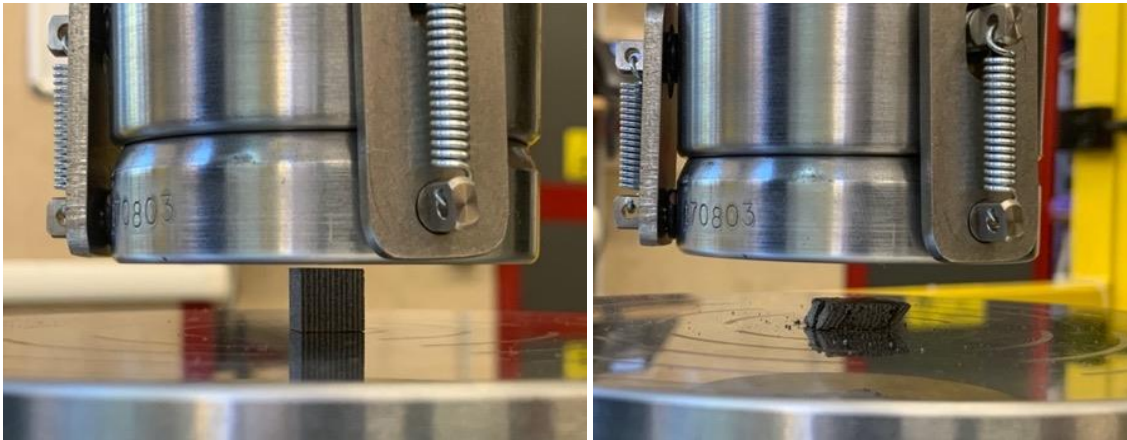


Figure 9.1: Samples before and after the compression test

In the Figure 9.1 is shown a sample before and after the compression test and we can notice that the sample is completely broken in the side and that small pieces are separated from the main volume.

## 9.1 H600\_30

In the Z direction, the compressive stress features the behavior shown in the Figure 9.2:

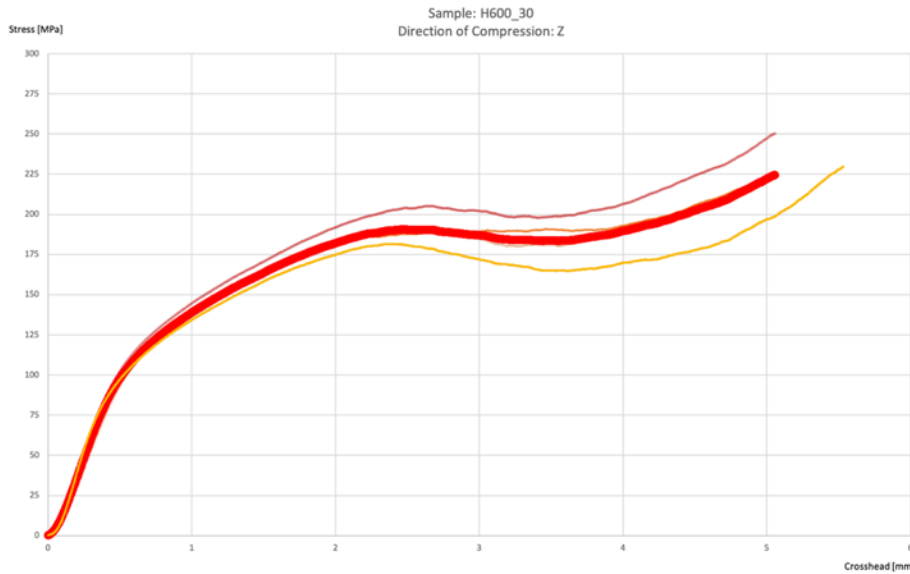


Figure 9.2: Compressive Tests in Z direction

The red pronounced line is the average curve of all the tests while the thinner lines are the curves resulted from the single tests. For this analysis we made 4 tests instead of 3 because the first one was to setup the machine, but since it gives us useful data, we decided to add it and as we were expecting, the shape of the curves shows three well defined steps. In the X direction, the compressive stress trend is shown in the Figure 9.3

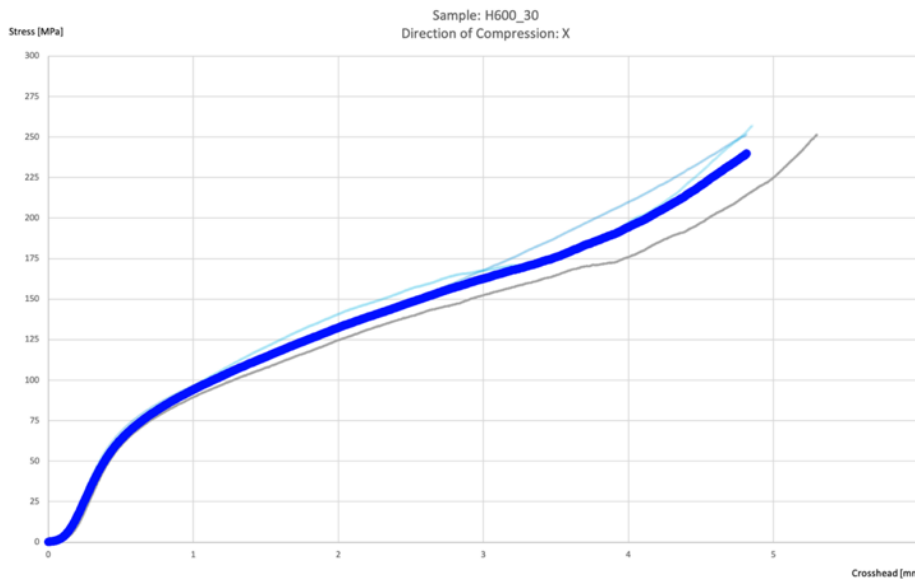


Figure 9.3: Compressive Tests in X direction

The blue pronounced line is the average curve of all the tests while the thinner lines are the curves resulted from the tests.

In these tests, the shape of the curves shows three steps but less defined with the absence of the plateau or the decrease of the load value.

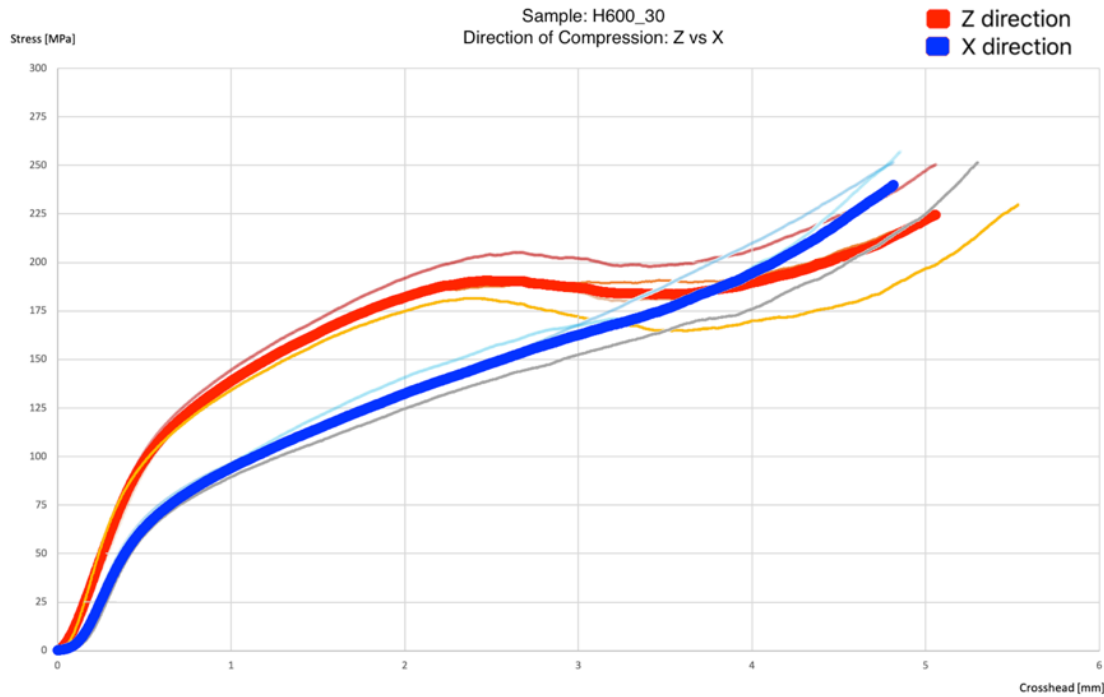


Figure 9.4: Comparison in the two directions X and Z

As shown in the Figure 9.4, both the curves of all samples are similar and all experiencing the three stages with the difference that in the Z direction there is a first local peak (or a plateau) but the first and the third step (as expected) are almost the same in the two directions.

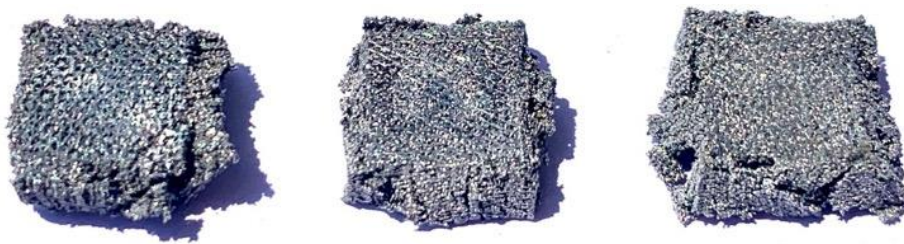


Figure 9.5: Compressed samples in Z direction



*Figure 9.6: Compressed samples in X direction*

After the tests, by analyzing the samples, we can notice that during the compression through the Z axis, the samples are completely broken in the side and there was also the loss of parts in the sides as shown in the Figure 9.5.

If the compression is made through the X axis, the samples show a volume compression without breaking in the sides significantly as shown in the Figure 9.6.



## 9.2 H600\_45

For this sample, as expected, the results of the compressive tests are similar to those of the sample H600\_30.

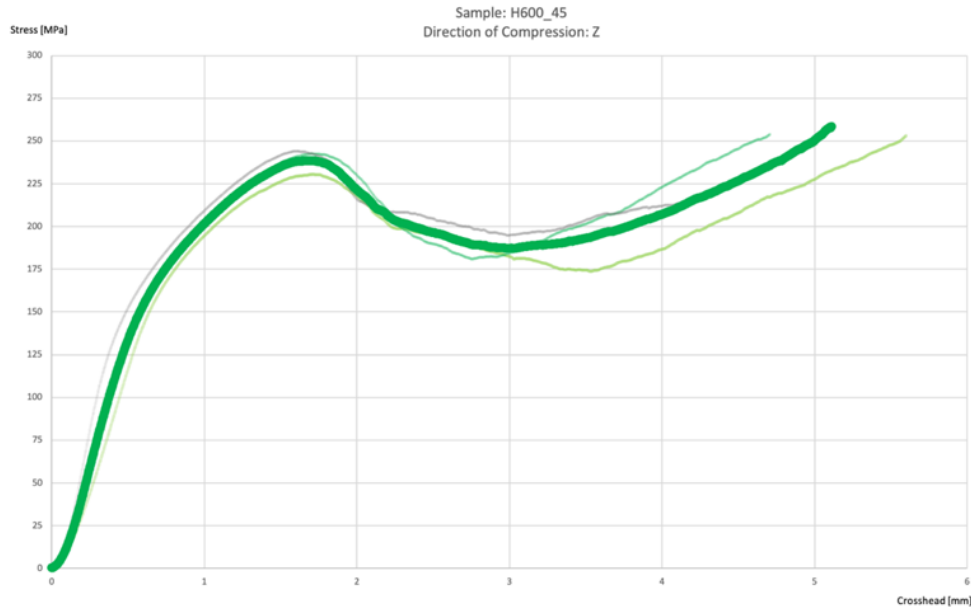


Figure 9.7: Compressive Tests in Z direction

The green pronounced line in the Figure 9.7 is the average curve of all the tests made in the Z direction and here the three stages are very defined.

In the X direction, the compressive stress has the behavior shown in the Figure 9.8:

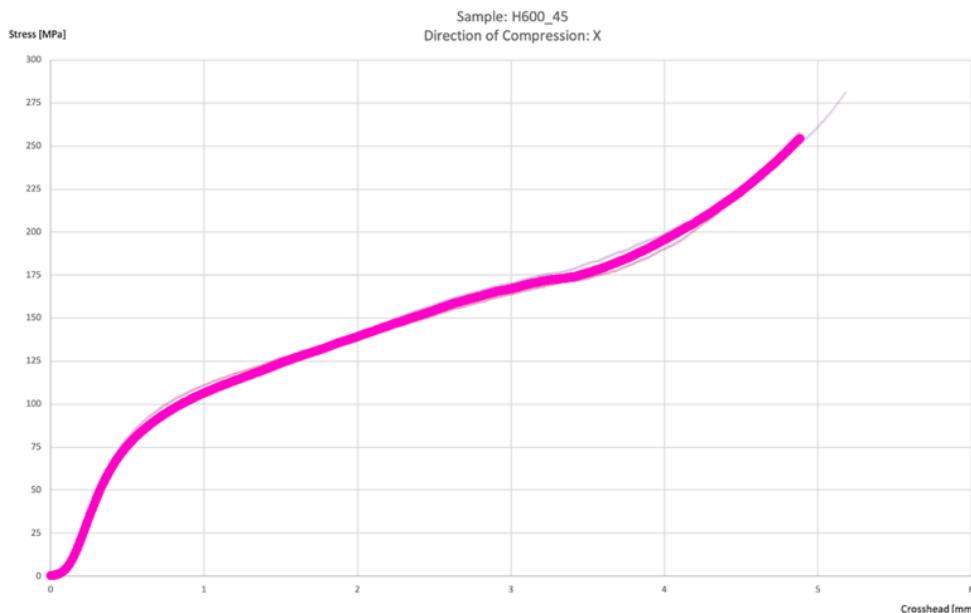


Figure 9.8: Compressive Tests in X direction

For these samples, as for the samples H600\_30, the shape of the curves shows three steps.

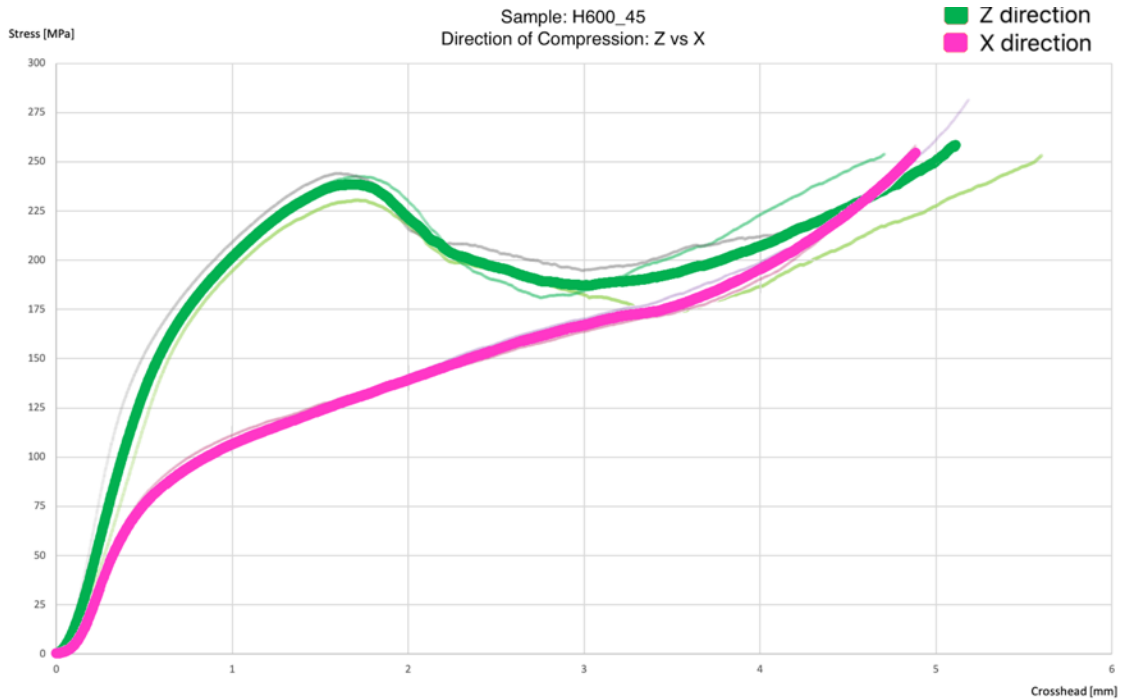


Figure 9.9: Comparison in the two directions X and Z

As shown on the Figure 9.9, both the curves of all samples are similar and all experiencing the three stages with the difference that in the Z direction there is a first local peak (or a plateau) but the first and the third step (as expected) are almost the same in the two directions.



Figure 9.10: Compressed samples in Z direction



Figure 9.11: Compressed samples in X direction

After the tests, by analyzing the samples, we can notice that during the compression through the Z axis, the samples are completely broken in the side and there was also the loss of parts in the sides as shown in the Figure 9.10.

If the compression is made through the X axis, the samples show a volume compression without breaking in the sides significantly as shown in the Figure 9.11.

### 9.3 Conclusions

Compressive tests yielded stress-strain curves: the curves of all samples are similar, all experiencing three stages:

- The first stage is the linear elastic portion caused by elastic deformation of strut and only takes small part of the whole curves. In this stage, linear relationship between stress and strain can be observed.;
- The second stage is characterized by a plateau in the middle part which is related to a high plastic deformation with only low increase in stress. This stage is the constant stress portion and during compressing, metal struts won't immediately connect to each other to achieve the density because of the high porosity. In this stage, samples experience a long-term deformation under a certain stress. Such stress platform is ascribed to the balance between stress decrease caused by holes collapse and stress increase caused by holes densification;
- The third stage is characterized by a densification of the metal, where the stress increases sharply: it is caused by the collapse of struts followed by complete collapse of cells accompanied with compaction of the porous structure. In this stage density increases following the increase of strain, and struts of porous sample start to contact with each other. Therefore, the compression to porous samples in this stage, which corresponds to the compression to bulk metal, leads to a rapid stress increase.

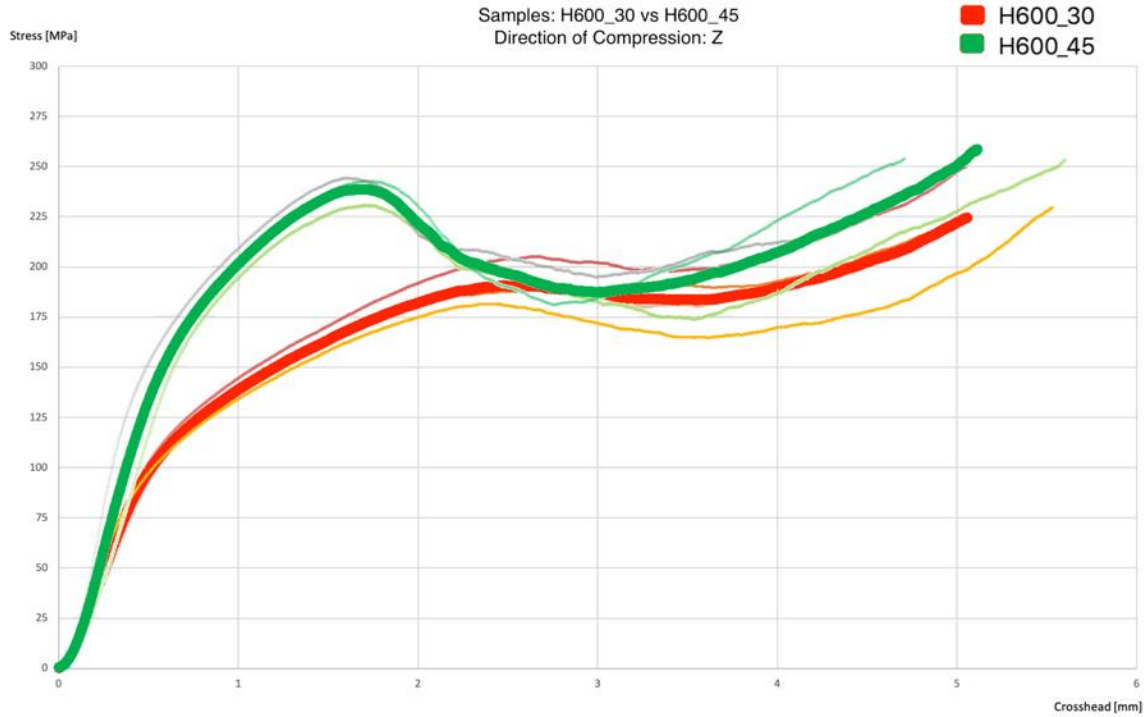


Figure 9.12: Comparison of the two different types of samples in Z direction

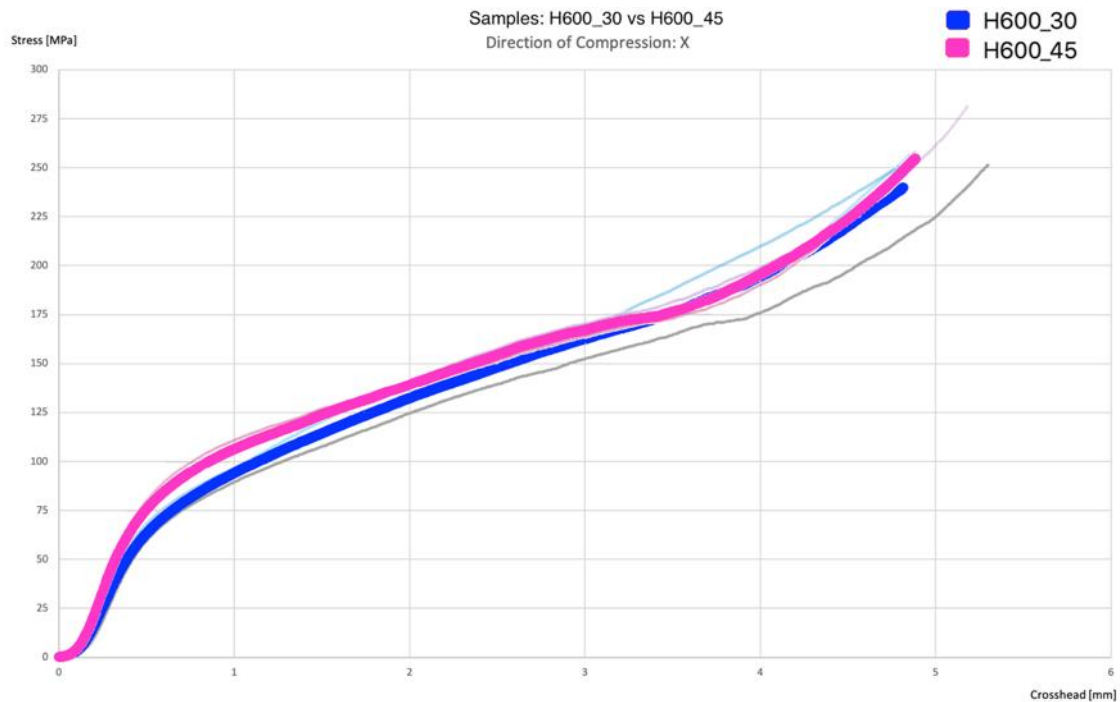


Figure 9.13: Comparison of the two different types of samples in X direction

The Figure 9.12 and Figure 9.13 show the comparison of the tests in the same direction between the different types of samples: in the Figure 9.12 there are shown the mean

curves of the compression tests in the Z direction and in the Figure 9.13 there are shown the mean curves of the compression tests in the X direction.

The curves of all the samples have a similar shape and all experiencing the three stages. However, talking about the compression in the Z axis (Figure 9.12), the samples H600\_45 (green curve) have a higher strength value before the decrease but both the typology of samples have similar first and third stages.

In the X direction (Figure 9.13) the curves of all samples have almost the same shape and they overlap in most of the points, so there is almost no difference between them.

In addition, at the beginning the shape of the curves shows a small positive concavity which can be reasonably ascribed to the fact that the two faces of the sample (in contact with the compressing machine) are not perfectly parallel and so there is a first phase (almost a pre-phase) in which the sample settles down.

## **10 Final Conclusion**

In summary, the direct slicing approach lead us to a number of advantages and it can be considered a smart way to achieve a good porous structure for different practical applications. The main reason for this approach is that the number of generated process files to be handled is reduced because STL files are not required and so there is no geometrical porosity design needed.

Without the design of a porous component, the surface of the component does not contain the porosity, because it is created through the process parameters, and so the file size is lightened. This reduction of the file weight simplifies the process, because there is no overload of the managing files.

In addition, part quality can be enhanced. Furthermore, the native CAD geometry must not be tessellated before slicing; and even adaptive slicing can be considered and implemented in this approach in future.

To sum up, to reach a good level of porosity, we introduced two different methods of printing (both based on the direct slicing approach) and we compared them: the first method is the beam overlap technique while the second method consists of the rotation of each layer of a constant angle.

The good adjustable pore sizes, the different tried techniques and the different compared geometries of the porous structure are a consequence of the geometrical freedom in laser beam melting

The beam overlap technique has been used to create homogeneous porous structures of controlled and interconnected porosity: structures have been developed with pore diameters in the range of 300 $\mu\text{m}$  and 500  $\mu\text{m}$  and all the porous have a similar shape and geometry. A potential negative effect of the beam overlap structures is that the pore distribution is largely directionally dependent. In the side view the walls are seen in profile, which decreases the line of sight porosity compared to the highly open top view. The second method shows a different level of porosity which is less homogeneous and with different values of porous dimensions ranging from less than 100 $\mu\text{m}$  to 400 $\mu\text{m}$  in the same sample.

It has been shown that it is possible to work at significantly higher porosities yet still meet the mechanical requirements. This may be an important consideration for devices that require higher porosities and strength.

To check the mechanical properties, we have submitted the samples to the compression test: compression strength has an inverse relationship to porosity.

Depending on the application, the porous structure could be different and so one main objective is to investigate and develop specific scan strategies for the laser that can be applied in manufacturing open porosities. Open porosities are characterized by cavities and holes that are interconnected with each other and with their environment. These porosities can then be used for the perfusion of liquid or gaseous fluids, which is why they are often used as filter elements. The main filtering functions can be seen in Figure 10.1:

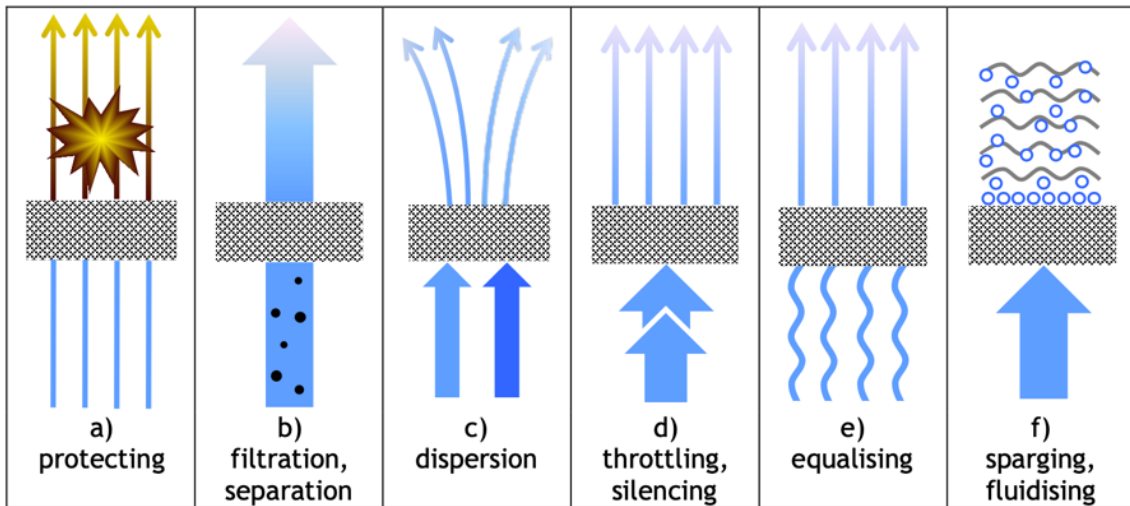


Figure 10.1: Different applications for porous materials [36]

## References

- [1] [O. Diegel, «Advances in Additive Manufacturing and Tooling,» 2014, 1-5.](#)
- [2] [T. Duda e L. V. Raghavan, «3D Metal Printing Technology,» February 2016, 9-18.](#)
- [3] [T. D. A, H. Wei, J. Zuback, T. Mukherjee, J. Elmer, J. Milewski, A. Beese, A. Wilson-Heid, A. De e W. Zhang, «Additive manufacturing of metallic components: Process, structure and properties,» October 2017, 116-120.](#)
- [4] [J. Liu, Y. Gao, Y. Fan e W. Zhou, «Fabrication of porous metal by selective laser melting as catalyst support for hydrogen production microreactor,» October 2019, 11-16.](#)
- [5] [A. Großmann, J. Felger, T. Frölich e J. G. C. Mittelstedt, «Melt pool controlled laser powder bed fusion for customised low-density lattice structures,» July 2019, 78-91.](#)
- [6] [B. Vayre, F. Vignat e F. Villeneuve, «Metallic additive manufacturing: State-of-the-art review and prospects,» January 2012, 42-54](#)
- [7] [V. Bhavar, P. Kattire, V. Patil, S. Khot, K. Gujar e R. Singh, «A review on powder bed fusion technology of metal additive manufacturing,» April 2016, 1-6](#)
- [8] [C. Xie, Q. Gao, P. Wang, L. Shao, H. Yuan, J. Fu, W. Chen e Y. He, «Structure-induced cell growth by 3D printing of heterogeneous scaffolds with ultrafine fibers,» August 2019, 12-14](#)
- [9] [Y. Zhu, X. Tian, J. Li e H. Wang, «The anisotropy of laser melting deposition additive manufacturing Ti-6.5Al-3.5Mo-1.5Zr-0.3Si titanium alloy,» November 2014, 104-122](#)
- [10] [R. J. Friel e R. Harris, «Ultrasonic additive manufacturing A hybrid production process for novel functional products,» April 2013.](#)
- [11] [L. Yuan, S. Ding e C. Wen, «Additive manufacturing technology for porous metal implant applications and triple minimal surface structures: A review,» December 2018, 55-67.](#)
- [12] [R. Singh e M. Chhabra, «Three-Dimensional Printing in Reference Module in Materials Science and Materials Engineering,» October 2017, 3-14](#)
- [13] [F. Echeta, X. Feng, B. Dutton, R. Leach e S. Piano, «Review of defects in lattice structures manufactured by powder bed fusion,» January 2020.](#)
- [14] [A. Kumar, S. Mandal, R. Vasireddi, S. Barui, U. Gbureck, M. Gelinsky e B. Basu, «Low temperature additive manufacturing of three dimensional scaffolds for bone-](#)



- [tissue engineering applications: Processing related challenges and property assessment,» May 20, 784-792](#)
- [15] [B. Zhang, X. Pei, C. Zhou, Y. Fan, Q. Jiang, A. Ronca, U. D'Amora, Y. Chen, H. Li, Y. Sun e X. Zhang, «The biomimetic design and 3D printing of customized mechanical properties porous Ti6Al4V scaffold for load-bearing bone reconstruction,» April 2018, 3-17.](#)
- [16] [L. Dall'Ava, H. Hothi, A. D. Laura, J. Henckel e A. Hart, «3D Printed Acetabular Cups for Total Hip Arthroplasty: A Review Article,» June 2019, 2-11.](#)
- [17] [F. A. Shah, O. Omar, F. Suska, A. Snis, A. Matic, L. Emanuelsson, B. Norlindh, J. Lausmaa, P. Thomsen e A. Palmquist, «Long-term osseointegration of 3D printed CoCr constructs with an interconnected open-pore architecture prepared by electron beam melting, 2-11](#)
- [18] [F. Yang, C. Chen, Q. Zhou, Y. Gong, R. Li, C. Li, F. Klämpfl, S. Freund, X. Wu, Y. Sun, X. Li, M. Schmidt, D. Ma e Y. Yu, «Laser beam melting 3D printing of Ti6Al4V based porous structured dental implants: fabrication, biocompatibility analysis and photoe, 1-9](#)
- [19] [A. B. Nover, S. L. Lee, M. S. Georgescu, D. R. Howard, R. A. Saunders, W. T. Yu, R. W. Klein, A. P. Napolitano, G. A. Ateshian e C. T. Hung, «Porous titanium bases for osteochondral tissue engineering,» August 2015, 286-290.](#)
- [20] [M. Fousová, J. Kubásek, D. Vojtěch, J. Fojt e J. Čapek, «3D printed porous stainless steel for potential use in medicine,» May 2017, 1-5.](#)
- [21] [S. S.E., A. A., M. N.S., M. A., N. M., S. S., E. M. e K. H.E., «Mechanical and shape memory properties of triply periodic minimal surface \(TPMS\) NiTi structures fabricated by selective laser melting,» October 2018, 1-6.](#)
- [22] [Q. Ran, W. Yang, Y. Hu, X. Shen, Y. Yu, Y. Xiang e K. Cai, «Osteogenesis of 3D printed porous Ti6Al4V implants with different pore sizes,» April 2018, 1-11.](#)
- [23] [W. v. Grunsven, R. Goodall e G. C. Reilly, «Porous metal implants for enhanced bone ingrowth and stability,» March 2011.](#)
- [24] [A. Vyatskikh, S. Delalande, A. Kudo, X. Zhang, C. M. Portela e J. R. Greer, «Additive manufacturing of 3D nano-architected metals,» September 2018, 1-4.](#)
- [25] [J. S. a, J. Yang, Z. Li, L. Zhu, L. Li e X. Wang, «Design and fabrication of graduated porous Ti-based alloy implants for biomedical applications,» August 2017, 1043-1047.](#)

- [26] [J. Sehart, A. Martha e G. Witt, «Direct slicing approach for the production of perfused components by laser beam melting,» May 2014, 96-105](#)
- [27] [X. Cheng, S. Liu, C. Chen, W. Chen, M. Liu, R. Li, X. Zhang e K. Zhou, «Microstructure and mechanical properties of additive manufactured porous Ti–33Nb–4Sn scaffolds for orthopaedic applications,» August 2019, 1-12](#)
- [28] [X. Tan, Y. Tan, C. Chow, S. Tor e W. Yeong, «Metallic powder-bed based 3D printing of cellular scaffolds for orthopaedic implants: A state-of-the-art review on manufacturing, topological design, mechanical properties and biocompatibility,» February 2017, 1331-1035.](#)
- [29] [«Renishaw RBV RenAM 500 series additive manufacturing systems,» 2019.](#)
- [30] [W. P. Syam, A. Al-Ahmari, M. A. Mannan e K. A. Al-Wazzan, «Metallurgical, accuracy and cost analysis of Ti6Al4V dental coping fabricated by electron beam melting process,» November 2011.](#)
- [31] [E. Akca e E. Trgo, «Metallographic Procedures and Analysis,» February 2016.](#)
- [32] [X. Lu, T. Zhao, X. Ji, J. Hu, T. Li, X. Lin e W. Huang, «3D printing well organized porous iron-nickel/polyaniline nanocages multiscale supercapacitor,» May 2018, 78-82.](#)
- [33] [B. Jackson, «South korean research demonstrates blu-ray powered micro 3d printing for cell scaffolds,» May 2017.](#)
- [34] [R. Stamp, P. Fox, W. O'Neill, E. Jones e C. Sutcliffe, «The development of a scanning strategy for the manufacture of porous biomaterials by selective laser melting,» June 2009, 1839-1847.](#)
- [35] [F. Calignano, G. Cattano e D. Manfredi, «Manufacturing of thin wall structures in AlSi10Mg alloy by laser powder bed fusion through process parameters,» February 2018 Italy, 773-782.](#)
- [36] [A. N. meetei, A. Bhattacharya e R. Chutia, «Study of Double-pass Strategies for Crack Reduction in SLM of a Tool Stee,» July 2019, 33-37](#)
- [37] [R. plc, «Ti6Al4V ELI-0406 powder for additive manufacturing,» June 2016, 2-6.](#)